TÉCNICO LISBOA

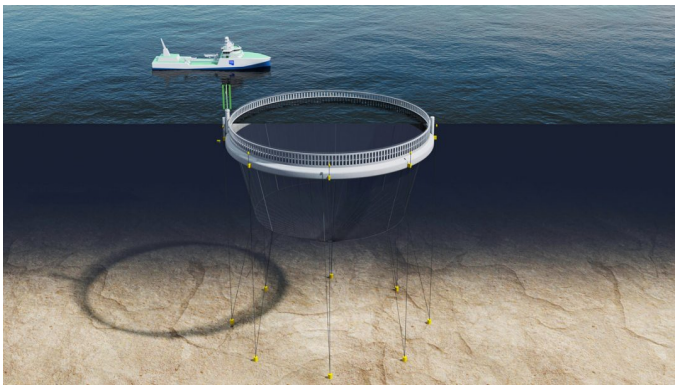

Simulations of Flow Around Bluff Bodies at High Reynolds Numbers

Guilherme Vaz de Almeida Fontes Neves

Thesis to obtain the Master of Science Degree in

Aerospace Engineering

Supervisor: Prof. Luís Rego da Cunha Eça

Examination Committee

Chairperson: Prof. Fernando José Parracho Lau
Supervisor: Prof. Luís Rego da Cunha Eça
Members of the Committee: Prof. João Manuel Ribeiro Costa Baltazar
Eng. Maarten Kerkvliet

January 2021

In memory of my grandmother Nazaré, who taught me the way here.

Em memória da minha avó Nazaré, que me ensinou o caminho até aqui.

Declaration

I declare that this document is an original work of my own authorship and that it fulfills all the requirements of the Code of Conduct and Good Practices of the Universidade de Lisboa.

Acknowledgments

I would first like to thank my supervisor, Professor Luís Eça for offering me the opportunity to work in this project within the collaboration IST/MARIN. And to express my gratitude for all of his advice, suggestions and encouragement throughout the duration of this work.

I want to express my gratitude towards NUMECA for allowing me to make use of their mesh generator, HEXPRESS, an essential tool for the development of this project.

Without the inspiration and knowledge of my previous educators, teachers and Professors this work would not have been possible. A special word of gratefulness for the countless hours spent in classrooms learning and growing with their help and motivation.

To my friends and colleagues, I thank you for your support and advice you have given me. In particular a heartfelt thank you to the two people who for more than a decade I have had the pleasure of calling my best friends, Guilherme Pinto and Diogo Paraíso.

Lastly I would like to thank my family. My brother, Gonçalo, who will never cease to inspire me with his hard work and dedication. My mother, Manuela, whose calming advice has always helped me to see things in perspective. And my father, David, who gave me the tools and skills to be able to succeed in life.

Resumo

O escoamento em volta de corpos não fuselados tem sido extensamente investigado em mecânica de fluidos computacional (CFD), sendo que o cilindro circular é o principal objeto dessa investigação. Motivado pelo projeto de uma estrutura de aquacultura off-shore, este trabalho foca-se em escoamento estatisticamente não-estacionário em volta de corpos não fuselados com diferentes formas transversais. Dois estudos preliminares foram conduzidos. As equações de Navier Stokes em média de Reynolds (RANS) foram usadas e modelos de turbulência ($KSKL$ e $k-\omega$ SST) foram usados para fechar o problema.

O primeiro estudo tenta verificar as propriedades de convergência de malhas não estruturadas. O escoamento em volta de cilindros bidimensionais a $Re = 1000$ com secções circulares, hexagonais e octagonais foi simulado de forma a comparar resultados com a literatura disponível. As malhas não estruturadas mostraram bons resultados.

O segundo estudo preliminar mostra a simulação de escoamento em volta de cilindros bidimensionais a $Re = 10^8$ com secções circulares, octagonais e hexadecagonais de forma a avaliar o impacto do uso de leis da parede no erro numérico e de modelação a Reynolds elevados. Os resultados mostraram um melhoramento significativo na robustez numérica com o uso de leis da parede, em paricular nas geometrias poligonais.

Os dois estudos preliminares levaram a um set-up do estudo 3D do escoamento em volta da estrutura completa a $Re = 10^8$ composto por malhas não estruturadas e com leis da parede. Estimativas das forças e momentos médios são apresentados, assim como o conteúdo em frequência, que permitirão a realização de uma análise estrutural.

Keywords: Corpos Não-Fuselados, Secção Octogonal, Malhas Não-Estruturadas, Leis da Parede, Reynolds Elevado, RANS.

Abstract

The flow around bluff bodies has been extensively studied in computational fluid dynamics (CFD), with the circular cylinder as the prime subject of investigation. Motivated by the project of a complex off-shore aquaculture structure, this work focuses on statistically unsteady flow around bluff bodies of different cross-sectional shape. Two preliminary studies were performed. The Reynolds-Averaged Navier Stokes (RANS) equations are used for modeling and closed with turbulence models ($KSKL$ and $k-\omega$ SST).

The first preliminary study aims to check the convergence properties of unstructured grids. The flow around two-dimensional infinite cylinders at $Re = 1000$ with circular, hexagonal and octagonal cross-sections was simulated in order to compare with the available literature. The unstructured grids showed to be able to accurately perform the simulations.

The second preliminary study presents the calculations of the flow around two-dimensional cylinders at $Re = 10^8$ with circular, octagonal and hexadecagonal cross-sections in order to assess the impact of the use of wall functions in the numerical and modeling error at very high Reynolds numbers. The results showed a significant improvement in numerical robustness with the use of wall functions, especially for the polygonal geometries.

The two preliminary studies led to a set up of the 3D study of flow around the aquaculture structure at $Re = 10^8$ made up of unstructured grids with wall functions. Estimations of the average forces and moments acting on the structure were presented, as well as the frequency content, which will allow for an accurate structural analysis in the future.

Keywords: Bluff Bodies, Octagonal Cross-Section, Unstructured Grids, Wall Functions, High Reynolds Number, RANS.

Contents

List of Tables

List of Figures

Nomenclature

2D Two dimensional.

3D Three dimensional.

CAD Computer-Aided Design.

CFD Computational Fluid Dynamics.

DNS Direct Numerical Simulation.

FFT Fast Fourier Transform.

k$-\omega$ SST (Menter's) Shear Stress Transport Turbulence Model.

KSKL k-$\sqrt{k}l$ Turbulence Model.

RANS Reynolds Averaged Navier-Stokes Equations.

RHS Right Hand Side (of an equation).

U-RANS Unsteady Reynolds Averaged Navier-Stokes Equations.

WF Wall Functions.

Greek symbols

α_{exp} Explicit under relaxation factor.

α_{imp} Implicit under relaxation factor.

ϵ Turbulence dissipation rate.

μ Dynamic Viscosity of the fluid.

μ_t Dynamic turbulent eddy viscosity.

ν Kinematic Viscosity of the fluid.

ν_t Kinematic turbulent eddy viscosity.

ρ Density.

τ Shear Stress.

τ_w Shear stress at the wall.

$\overline{\phi}$ Average value of a given quantity ϕ.

ω Specific Turbulence dissipation rate.

Roman symbols

A Area.

C Courant Number.

C_D Coefficient of drag.

C_L Coefficient of lift.

d Diameter.

d_1 Circumscribed diameter.

d_2 Inscribed diameter.

f Vortex shedding Frequency.

F_i Total Force in i-direction.

Fr Froude Number.

g Acceleration of gravity.

I Turbulent Intensity.

k Turbulent Kinetic Energy.

L Characteristic length.

M_i Total Moments about i-direction.

N Number of faces of a polygon.

N_f Number of face elements.

N_r Number of realizations.

N_v Number of volumes.

p Pressure.

r_i Grid Refinement Ratio.

Re Reynolds number.

Re_c Critical Reynolds Number.

Re_{eff} Effective Reynolds number.

St Strouhal number.

t Time.

U, U_∞, V, V_∞ Inflow Velocity.

Subscripts

∞ Free-stream condition.

avg Average value of a given quantity.

n Normal component.

u_i Cartesian velocity components (tensor notation).

x, y, z Cartesian components.

x_i Cartesian coordinates (tensor notation).

Superscripts

ϕ' Fluctuation of a given quantity ϕ, with respect to the average value $\overline{\phi}$.

y^+ Dimensionless Wall distance.

Chapter 1

Introduction

1.1 Motivation and Objectives

A significant growth in fisheries and aquaculture production has been registered starting in the middle of the 20th century. This has led to an increase in fish consumption from 9kg per capita in 1961 to 20.2kg per capita in 2015 and additional growth is expected in the coming years. Even though aquaculture production is no longer growing at the rates it used to in the 1980s and 1990s it still continues to grow faster than any other food prodution sector. This growth is related to a stabilization of capture fishery production that started in the late 80s due to overfishing and regulations to prevent overfishing [1].

This increase in aquaculture production has been leading to a tendency of placing marine fish farms in more exposed locations, which translates to higher current and wind velocities and more energetic waves. One of the issues with this trend is that fish escape is more likely due to damages or collapse of the farm, meaning economic losses and genetic contamination of wild fish.

Both rigid and flexible floating fish farms exist, being that the former is made of concrete or steel and the latter is made of fabric. The work here presented will deal with a mix of flexible and rigid fish farm, since the floating ring is made out of concrete and the netting is made of plastic. This solution allows for a high rigidity of the structure, necessary to endure the conditions found in more open sea areas as well as minor maintenance and construction cost when compared with rigid closed fish farms.

The main objective of this work is to study the forces and moments acting on the structure so that an accurate structural analysis can be done in subsequent studies. To achieve this there are two challenges that must be tackled:

- The **complexity of the geometry**: the floating ring is an octagon. On each of the faces there are holes that allow fluid to be exchanged with the outside of the structure near the water surface. Along the face there is also a rounded protrusion that is hollow and is what allows the structure to float;
- The **Reynolds number**: The diameter of the aquaculture structure is $d = 136.3m$, considering this to be the characteristic length, and a fluid velocity of $U = 1m/s$, which is a valid current velocity for off-shore applications, the Reynolds number is: $Re = \frac{dU}{\nu} = 1.363 \times 10^8$, where ν is the kinematic

viscosity of the fluid. This is a very high Reynolds number, which presents a challenge from a CFD (Computational Fluid Dynamics) standpoint. For the purpose of this investigation an approximation to a Reynolds number of $Re = 10^8$ will be made.

With this in mind it would be unwise to immediately start with the study of flow around the aquaculture structure, since most likely the numerical set up would not be ideal and computational time would be wasted. Consequently, two preliminary studies were made:

- The first study attempted to deal with minimizing the problem of the complex geometry: Using **unstructured grids** to discretize the domain around the aquaculture structure would help deal with this problem. So a study with the objective of verifying the quality and numerical robustness of the unstructured grids produced by the software HEXPRESS™, as well as check numerical convergence properties as a function of body shape was performed. The study was 2D in nature and dealt with the flow around infinite cylinders with circular, hexagonal and octagonal cross-section at a much lower Reynolds number of $Re = 1000$. The work done by Khaledi and Andersson [2] was used as reference, in which the flow around hexagonal cylinders with two different orientations was studied at three different Reynolds numbers, the highest of which being $Re = 1000$. It was expected that the behaviour of the octagonal cylinder would be somewhere between the hexagonal and the circular cylinders. This study also served to understand the influence of unstructured grid refinement in the convergence of the simulation.

- The second study attempted to deal with the problem of the high Reynolds number: A domain discretization without **wall functions** is more accurate but also more computationally expensive than a simulation where wall functions are used [3]. This effect is heightened at a Reynolds number as high as the one being considered. So this study sets out to evaluate the numerical convergence properties of the simulation of bluff bodies with the RANS equations supplemented with the $k - \omega$ SST model for a Reynolds number of 10^8, which includes two topics: the robustness (iterative convergence) of the flow solver for geometries including obtuse angles on the surface in simulations performed with and without wall functions and the estimate of the grid refinement level required to obtain acceptable numerical uncertainties for the average force coefficients. The study also aims to compare the solutions obtained with and without wall functions to evaluate the ability to use wall functions in the simulations with flow around cylinders with circular, octagonal and hexadecagonal (16 sides) cross section at very high Reynolds numbers [4]. For this study the grids without wall functions generated in HEXPRESS™ did not present the necessary quality, so the grids generated for this study were structured grids generated using the *Grid Generation Tools for Structured Grids* [5].

This also makes evident the relevance of the topic from an aerospace engineering perspective. While this work is initially motivated by a floating aquaculture reservoir, the underlying theoretical and computational concepts can be applied to any blunt body in fluid, which represent important structures in aerospace engineering, found for example in landing gears, flapped wings and any other non-streamlined body in incompressible flow. It is predictable that effects which are important for the design

of aerodynamic structures such as turbulence and vortex shedding will also be of major importance in the design of the fish farm. Additionally, the Reynolds number at which the fish farm will function, $Re = 10^8$, is so high that almost no study has been performed for bluff bodies, which also motivates this work in an investigative capacity, since there are several engineering applications, besides aquaculture structures, at which bluff bodies might be at Reynolds numbers close to $Re = 10^8$.

1.2 Thesis Outline

The remainder of this work is divided into chapters, each with focus on different relevant aspects of the investigation:

- Chapter 2 presents a brief review of the literature already available regarding the flow around bluff bodies with special focus on polygonal cylinders in order to contextualize this work and the decisions taken throughout it;
- Chapter 3 defines the problem mathematically and geometrically, describing the equations that govern the flow, the turbulence models used, the computational domains of the three studies and their respective boundary conditions;
- In Chapter 4 a description of the tools and methods used to solve the problem using CFD is presented. An overview of the software used in this investigation is given, as well as the numerical options used in the software *ReFRESCO* [6] to solve the mathematical formulation of the problem. Furthermore, the spatial and temporal descritization of the studies is presented, i.e. the grids and the time steps size used for the simulations. Finally, the quantities of interest to be monitored are enumerated;
- Chapter 5 provides a description of the results obtained from the several simulations and from the post processing of the data obtained from said simulations. When relevant, those results are compared with the available literature to assess the validity of the results;
- Chapter 6 synthesises the conclusions that can be taken from this investigation and lays down suggestions of work that can be done to further the study of flow around bluff bodies.

Chapter 2

Background

Bluff bodies in turbulent flow and their respective vortex shedding effect have been the topic of research for many years, with the circular cylinder as the prime subject of the investigation. Williamson [7] studied extensively several vortex shedding regimes with Reynolds numbers ranging from 10^1 to 10^7 noting the different characteristics of each regime such as the transition to three dimensional effects, the different modes of vortex shedding, associated with vortex loops (mode A) and finer-scale streamwise vortices (mode B).

Extensive research has also been done around triangular (Number of faces, $N = 3$) and rectangular ($N = 4$) cylinders. Sohankar et al. [8] studied the flow around rectangular cylinders of different aspect ratios at low Reynolds numbers ($Re = 100$ and 200) to study the influence of the angle of incidence of the flow. Differences were noted on the separation of the flow, being that at $Re = 100$ with a face oriented geometry (one of the faces of the polygon faces the oncoming flow) the flow would separate at the downstream corners while at $Re = 200$ the flow would separate at the upstream corners, creating separation bubbles attached to the body.

However, the study of flow behind infinitely long bluff bodies with sharp edges with a cross section with more than four sides ($N > 4$), such as cylinders of hexagonal or octagonal cross-section has not received the same level of attention. This does not mean that no material can be found in the literature about this topic: Khaledi and Andersson [2] studied the flow around an hexagonal cylinder with 3D geometry using Direct Numerical Simulation (DNS) at three different Reynolds numbers ($Re = 100$, $Re = 500$, $Re = 1000$) for two orientations of the cylinder: face oriented and corner oriented. Considerable differences were found comparing to the rectangular and circular test cases, the most important being that the behaviour of the face oriented hexagonal cylinder is more alike that of a corner oriented rectangular cylinder and a corner oriented hexagonal cylinder to that of a face oriented rectangular cylinder. This is due to the point where separation will occur in one case or the other. In the case of a face oriented hexagon the separation will occur at the 120° corners of the hexagon, while in a corner oriented geometry, separation will happen at the leading edge of the faces parallel with the direction of the flow. Another important conclusion concerns the vortex shedding frequencies, characterized by the Strouhal

number, St, defined here as

$$St = \frac{fL}{U}, \tag{2.1}$$

where f is the frequency of vortex shedding and L is the characteristic length. For corner orientation, L is equal to the inscribed diameter, d_2, and for corner orientation L is equal to the circumscribed diameter, d_1, as can be seen in Figure 2.1. Khaledi and Andersson noted that St increased from $Re = 100$ to $Re = 500$, however no increase in St was recorded when testing $Re = 1000$, for any of the two orientations of the cylinder. In addition, the St recorded for face oriented cylinder was higher than for corner oriented. Thus arriving at the conclusion that for wake dynamics it is irrelevant if the front stagnation point is at a face or a corner but rather "if the width of the projected cylinder is determined by sharp corners or flow-parallel faces". It was also speculated by Khaledi and Andersson that the wake behind a octagonal cylinder would then have a behaviour similar to the one after a square cylinder, which is supported by the experimental data of flow around octagonal cylinders at $Re \approx 10^4$ by Bosch and Guterres [9], which showed that St was higher for corner-oriented octagonal cylinders compared to face-oriented octagonal cylinders.

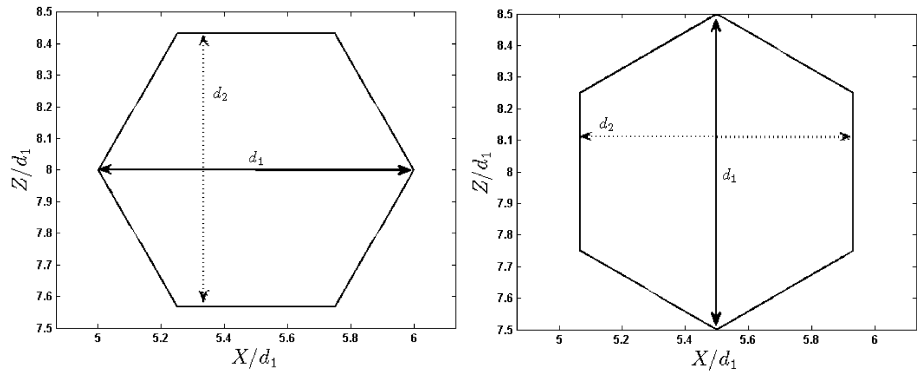

Figure 2.1: Orientations of the hexagonal cylinder by Khaledi and Andersson [2]: (a)-corner orientation; (b)-face orientation. Inscribed and circumscribed diameters are also shown.

Xu et al [10], motivated by the lack of experimental data concerning polygonal cylinders with $N \geq 5$, proceeded to test cylinders with $N = 2 - 8, N = 12, N = 16$ as well as a circular cylinder ($N = \infty$) based on fluid force, hot-wire, Particle Image Velocimetry (PIV) and flow visualisation measurements. The polygonal cylinders were studied from both corner and face orientations for a Reynolds number of $10^4 \sim 10^5$, depending on the longitudinally projected cylinder width. The dependence of time-averaged Drag Coefficient, C_D, and St on the number of faces was studied, as shown in Figure 2.2. Some of the conclusions of this work regarding cylinders with $N \leq 8$ were that, for Reynolds numbers ranging from 1×10^4 to 6×10^4 ($Re = 1 \times 10^4 < Re_c$ - Re_c is the critical Reynolds number - and $Re = 6 \times 10^4 > Re_c$), both C_D and St vary little over said Reynolds range, which suggest that there is no change to the boundary layer state. It was also noted that, for small N, the C_D and St values differ significantly for the two considered orientations. The dependence of the fluctuating lift coefficient, C'_L, on N was also studied. It was found that C'_L increases quickly with rising N, reaching a maximum at $N = 6$ for corner facing geometry and at $N = 4$ for face oriented geometry, and then drops rapidly before approaching

the value for $N = \infty$. It was also found that C'_L varies greatly between the two orientations for $N < 7$ but has the same value for both orientations for $N > 12$.

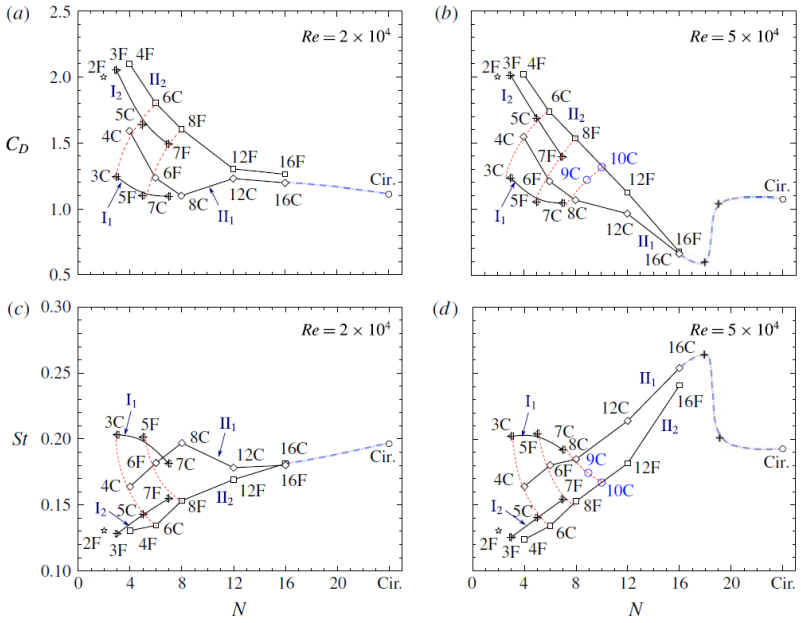

Figure 2.2: Dependence of C_D (a,b) and St (c,d) on the polygon side number N, for $Re < Re_c$ (a,c) and $Re > Re_c$ (b,d) [10].

Chapter 3

Problem Formulation

Any CFD problem needs to be described mathematically and geometrically. This set of constraints consists of:

- A set of equations that are able to describe the properties of the flow;
- A computational domain that defines the geometrical limits of the calculations;
- A set of boundary conditions that define how the equations are supposed to interact with the limits of the domain.

This chapter describes how these constraints were implemented in this work.

3.1 RANS Formulation

Solving the Navier-Stokes equations directly, in what is called Direct Numerical Simulation (DNS), is only feasible in specific situations (for example, low Reynolds numbers and small computational domains). At very high Reynolds numbers DNS is not feasible [11] and, given that the main concern of this work are the mean properties of the flow, a RANS (Reynolds Averaged Navier-Stokes) approach was taken.

As such, it is useful to perform a Reynolds decomposition, which will deal with the intrinsically unsteady features of turbulence, when dealing with turbulent flows, as is the case with this investigation. Both steady and unsteady flows can be subject to a Reynolds decomposition, the key difference being that in the former, the mean value of the decomposition represents a time average of the quantity of interest and in the latter, the mean value represents the ensemble average of the quantity of interest.

The research that this work focuses on is unsteady in nature, so what will be done is to apply the Reynolds decomposition for unsteady flows to the Navier-Stokes equation (mass and momentum balance), obtaining the, so-called **Unsteady Reynolds-Averaged Navier-Stokes Equations (U-RANS)**.

3.1.1 Reynolds Decomposition

The Reynolds decomposition is a tool that allows to separate a given quantity, ϕ, into a mean value, $\overline{\phi}$, and a fluctuation from said mean value, ϕ'. Considering unsteady flow, for a given quantity that varies in space, x_i, and time, t:

$$\phi(x_i, t) = \overline{\phi}(x_i, t) + \phi'(x_i, t). \tag{3.1}$$

In unsteady flow it does not make sense to eliminate the dependence on time for the mean value, which is why it is needed to adopt an ensemble averaging process. It follows that the mean value, i.e. ensemble average, for an unsteady flow is computed as:

$$\overline{\phi}(x_i, t) = \lim_{N_r \to \infty} \frac{1}{N_r} \sum_{n=1}^{N_r} \phi(x_i, t + nt). \tag{3.2}$$

In this averaging procedure N_r is the number of realizations (as described by Ferziger and Peric: "imagined set of flows in which all controlable factors are kept fixed" [11]). N_r must be as large as possible in order to obtain statistical convergence.

3.1.2 Averaged Continuity and Momentum Equations

A consequence of equation (3.2) is that the mean value of a fluctuation is zero, $\overline{\phi}' = 0$. Thus, averaging a linear term results in the averaged quantity of that term.

Additionally, the average of a product of two terms results in:

$$\overline{u_i \phi} = \overline{(\overline{u_i} + u_i')(\overline{\phi} + \phi')} = \overline{u_i}\overline{\phi} + \overline{u_i' \phi'}. \tag{3.3}$$

The terms $\overline{\overline{u_i}\phi'}$ and $\overline{\overline{\phi} u_i'}$ are both zero because the average of a fluctuating quantity is zero, otherwise they would appear in equation (3.3).

Some attention must be payed to the last term of equation (3.3), $\overline{u_i' \phi'}$. This term is usually non-zero due to correlation between the two quantities in turbulent flows; The **Reynolds Stresses**, $\rho\overline{u_i' u_j'}$, where ρ is the fluid density, are examples of such non-zero terms.

Applying the aforementioned averaging method to the continuity and momentum equations for incompressible flow results in:

$$\frac{\partial(\rho\overline{u_i})}{\partial x_i} = 0, \tag{3.4}$$

$$\frac{\partial(\rho\overline{u_i})}{\partial t} + \frac{\partial}{\partial x_j}\left(\rho\overline{u_i u_j} + \rho\overline{u_i' u_j'}\right) = -\frac{\partial \overline{p}}{\partial x_i} + \frac{\partial \overline{\tau_{ij}}}{\partial x_j}, \tag{3.5}$$

where Cartesian coordinates and Tensor notation were used.

The terms τ_{ij} from equation (3.5) are the components of the mean viscous stress tensor, which in incompressible flow of a Newtonian fluid can be expanded to:

$$\overline{\tau_{ij}} = \mu \left(\frac{\partial \overline{u_i}}{\partial x_j} + \frac{\partial \overline{u_j}}{\partial x_i} \right), \tag{3.6}$$

where μ is the dynamic viscosity.

The presence of the Reynolds stresses indicates that the equations are not closed, i.e. that there are more variables than there are equations, this is referred to as the **RANS closure problem**. Turbulence Models are used to close the equations by approximating values for these terms, either empirically or by use of transport equations. The $k-\omega SST(2003)$ model [12, 13] and the $KSKL$ model [14, 15] are two such models and will be used in this research.

3.2 Turbulence Models

The $KSKL$ model was only used in the first preliminary study, to compare the behaviour of each model with the literature. For the rest of this investigation the $k-\omega SST(2003)$ model was used. Both models are two-equation models, i.e. two independent transport equations, for two independent scales, are used to close the RANS equations. For the velocity scale, all two-equation models use the equation for the turbulent kinetic energy, k, since it mainly requires a model for turbulent diffusion. That means that the main distinguishing characteristic between models resides in the equation for the length scale.

3.2.1 $k-\omega$ SST (2003) Model

The $k-\omega$ Shear Stress Transport (SST) model was developed by Menter in 1994 [12] by modifying the definition of eddy viscosity in the baseline (BSL) model he developed in the same article and that itself is a combination of the $k-\epsilon$ [16] and Wilcox's $k-\omega$ model [17]. This is done by including in the equation a term relating to the transport of the turbulent shear stress $\tau =: -\rho\overline{u'v'}$, analogous to the Johnson-King model [18], this increased significantly the quality of the predictions particularly in adverse pressure gradient flows. The model equations are [12]:

$$\frac{\partial(\rho k)}{\partial t} + \frac{\partial(\rho U_j k)}{\partial x_j} = P_k - \beta^* \rho k\omega + \frac{\partial}{\partial x_j}\left[(\mu + \sigma_k \mu_t)\frac{\partial k}{\partial x_j}\right], \tag{3.7}$$

$$\frac{\partial(\rho \omega)}{\partial t} + \frac{\partial(\rho U_j \omega)}{\partial x_j} = P_\omega - \beta^* \rho k\omega^2 + \frac{\partial}{\partial x_j}\left[(\mu + \sigma_\omega \mu_t)\frac{\partial \omega}{\partial x_j}\right] + 2\rho(1-F_1)\frac{\sigma_{\omega 2}}{\omega}\frac{\partial k}{\partial x_j}\frac{\partial \omega}{\partial x_j}, \tag{3.8}$$

where the production terms for k and ω in its original form are [12]:

$$P_k = \tau_{ij}\frac{\partial U_i}{\partial x_j}, \qquad P_\omega = \frac{\alpha\rho}{\mu_t}\tau_{ij}\frac{\partial U_i}{\partial x_j} = \frac{\alpha}{\nu_t}P_k. \tag{3.9}$$

P_k can be rewritten by applying the Bousinesq hypothesis (The Bousinesq hypothesis postulated that the momentum transfer caused by turbulent eddies can be modelled by a viscosity - eddy viscosity - in an analogy to how momentum transfer caused by molecular motion can be described using the

molecular viscosity):

$$P_k = \mu_t S^2 - \mu_t \frac{1}{3}\left(\frac{\partial U_k}{\partial x_k}\right)^2 - \frac{2}{3}\rho k\left(\frac{\partial U_k}{\partial x_k}\right)^2, \tag{3.10}$$

with $S_{ij} = \frac{1}{2}\left(\frac{\partial U_i}{\partial x_j} + \frac{\partial U_j}{\partial x_i}\right)$ and $S^2 = 2S_{ij}\frac{\partial U_i}{\partial x_j} = 2S_{ij}S_{ij}$.

The additional closure coefficients are:

$$F_1 = \tanh\left(arg^4\right), \tag{3.11}$$

$$arg = min\left[max\left(\frac{\sqrt{k}}{\beta^*\omega d}, \frac{500\nu}{d^2\omega}\right), \frac{4\rho\sigma_{\omega 2}k}{CD_{k\omega}d^2}\right], \quad CD_{k\omega} = max\left(2\rho\sigma_{\omega 2}\frac{1}{\omega}\frac{\partial k}{\partial x_i}\frac{\partial \omega}{\partial x_i}, 1\times 10^{-20}\right), \tag{3.12}$$

where d is the distance to nearest wall and

$$\alpha = F_1\alpha_1 + (1-F_1)\alpha_2, \qquad \beta = F_1\beta_1 + (1-F1)\beta_2, \tag{3.13}$$

$$\sigma_k = F_1\sigma_{k1} + (1-F_1)\sigma_{k2}, \qquad \sigma_\omega = F_1\sigma_{\omega 2} + (1-F_1)\sigma_{\omega 2}, \tag{3.14}$$

with constants

$$\beta^* = 0.09, \quad \alpha_1 = 0.5532, \quad \beta_1 = 0.075, \quad \sigma_{k1} = 0.85,$$
$$\sigma_{\omega 1} = 0.5, \quad \alpha_2 = 0.4404, \quad \beta_2 = 0.0828, \quad \sigma_{k2} = 1.0, \quad \sigma_{\omega 2} = 0.856,$$

and the eddy viscosity, ν_t:

$$\nu_t = \frac{a_1 K}{max(a_1\omega, F_2\Omega)}, \qquad a_1 = 0.31, \tag{3.15}$$

$$F_2 = \tanh\left(arg_2^2\right), \qquad arg_2 = max\left(\frac{2\sqrt{k}}{0.09\omega d}, \frac{500\nu}{\omega d^2}\right), \tag{3.16}$$

where Ω is the absolute value of vorticity. With this the value of F_1 is equal to one close to a wall, retaining the $k-\omega$ behaviour and it is equal to zero far from a wall, retaining the $k-\epsilon$ behaviour.

The P_k term is limited to prevent the build up of turbulence in stagnation regions. Refering to this term as $\tilde{P_k}$ comes:

$$\tilde{P_k} = min(P_k, 20\beta^*\rho k\omega). \tag{3.17}$$

This description refers to the original $k-\omega$ SST model published in 1994, however, in 2003 Menter published slight variations to his own model [13], these variations are then the $k-\omega$ SST (2003) model. The alterations are:

$$\nu_t = \frac{a_1 k}{max\left(a_1\omega, F_2 S\right)}, \qquad a1 = 0.31, \tag{3.18}$$

$$\alpha_1 = \frac{5}{9}, \qquad \alpha_2 = 0.44, \tag{3.19}$$

$$CD_{k\omega} = max\left(2\rho\sigma_{\omega 2}\frac{1}{\omega}\frac{\partial k}{\partial x_i}\frac{\partial \omega}{\partial x_i}, 1\times 10^{-10}\right), \tag{3.20}$$

and

$$\tilde{P_k} = min(P_k, C\beta^*\rho k\omega), \tag{3.21}$$

where C is a constant. In the 2003 model $C = 10$, however the computational software used in this work applies $C = 15$.

It is the model with these alterations that will be used throughout this work.

3.2.2 KSKL Model

The KSKL model was derived by Menter et al. [14] based on the k-kL model by Rotta [19, 20]. This model as been formulated as a one- and two- equation model that uses $\Phi = \sqrt{k}L$ as the scaling variable. This results in the equations [14, 15]:

$$\frac{\partial(\rho k)}{\partial t} + \frac{\partial(\rho U_j k)}{\partial x_j} = P_k - c_\mu^{\frac{3}{4}}\cdot\rho\frac{k^2}{\Phi} + \frac{\partial}{\partial x_j}\left(\frac{\mu_t}{\sigma_k}\frac{\partial k}{\partial x_j}\right), \tag{3.22}$$

$$\frac{\partial(\rho\Phi)}{\partial t} + \frac{\partial(\rho U_j\Phi)}{\partial x_j} = \frac{\Phi}{k}P_k\left(\zeta_1 - \zeta_2\left(\frac{L}{L_{\nu K}}\right)^2\right) - \zeta_3\cdot\rho k + \frac{\partial}{\partial x_j}\left(\frac{\mu_t}{\sigma_\Phi}\frac{\partial\Phi}{\partial x_j}\right), \tag{3.23}$$

$$\mu_t = c_\mu^{\frac{3}{4}}\rho\Phi, \qquad L_{\nu K} = \kappa\left|\frac{U'}{U''}\right|, \qquad U'' = \sqrt{\frac{\partial^2 U_i}{\partial x_k^2}\frac{\partial^2 U_i}{\partial x_j^2}}, \tag{3.24}$$

$$U' = S = \sqrt{2\cdot S_{ij}S_{ij}}, \qquad S_{ij} = \frac{1}{2}\left(\frac{\partial U_i}{\partial x_j} + \frac{\partial U_j}{\partial x_i}\right), \qquad P_k = \mu_t S^2, \tag{3.25}$$

where $\zeta_1, \zeta_2, \zeta_3\sigma_k, \sigma_\Phi, c_\mu$ and κ are constants of the model, whose values are shown in Table 3.1. The definition of $L_{\nu K}$ given in equation (3.25) is a generalization of the boundary layer formulation to three-dimensional flows and is representative of a natural length scale for the flow [15].

Table 3.1: Constants of the KSKL model

ζ_1	ζ_2	ζ_3	σ_k	σ_Φ	c_μ	κ
0.8	1.47	0.0288	2/3	2/3	0.09	0.41

3.3 Computational Domain

As previously stated, two preliminary CFD studies were performed in order to choose the best possible settings for the main computations. The studies had different objectives and were performed at different Reynolds numbers, so naturally the computational domain of each study is different.

3.3.1 Preliminary Study 1 - Flow around 2D Cylinders at $Re = 10^3$

This study aims to check the quality and robustness of unstructured grids against a case where results are available, as well as understand the impact of non-structured grid refinement on the convergence of the solution. Khaledi and Andersson's investigation of flow around hexagonal cylinders [2] was chosen as the benchmark. As such, the domain used for this study tried to recreate the domain they used.

Their domain was $20d$ long, $16d$ wide and $6d$ high (x, y, z), with the axis of the cylinder centered at ($x = 5.5d$, $y = 8.0d$), where d is the circumscribed diameter of the hexagon, i.e. diameter between two opposing corners of the polygon, which is considered to be the reference length. A similar domain was created, with the caveat that the simulations here performed were 2D in nature and as such the length of the cylinder in the z-direction is considered to be infinite. Additionally, rather than only simulating the flow around hexagonal cylinders with corner and face orientation, simulations were also performed on the flow around a circular cylinder and an octagonal cylinder with both orientations, as can be seen in Figure 3.1. The dimensions of the domain were the same regardless of the cross-sectional shape of the cylinder.

3.3.2 Preliminary Study 2 - Flow around 2D Cylinders at $Re = 10^8$

This study aimed to check the impact of using wall functions on the computation of a flow at a Reynolds number of 10^8. At this Reynolds number the domain used in the first preliminary study would be too small and interactions between the boundary conditions and the wake of the cylinder would deteriorate the quality of the solution. As such, a bigger domain, based on previous investigations [21], was designed. It was then decided that a domain $118d$ long and $102d$ wide was adequate, with the center of the cylinder placed in the width-wise centerline of the domain, $51d$, and lengthwise $40d$ away from the inlet. The cylinders studied had circular, octagonal and hexadecagonal cross-sectional shapes. An illustrative example of the domains used for this preliminary study is presented in Figure 3.2 using the circular geometry.

3.3.3 3D Study - Flow around aquaculture structure at $Re = 10^8$

The final part of this work concerns itself with the flow around the complete aquaculture structure at a Reynolds number of $Re = 10^8$. Some simplifications were made in order to guarantee the feasibility of the simulations:

- The net was considered to be non-permeable and non-deformable, in effect acting as a wall, which means no flow travels on the inside of the structure. This was done for simplicity and due to the fact that, at the time the simulations were performed, the ability to accurately simulate permeable structures was not available in ReFRESCO.
- Waves were not considered for the simulations as the Froude Number, $Fr = \frac{U}{\sqrt{gL}}$, where g is the acceleration of gravity and L is the characteristic length, commonly used to describe the resistance

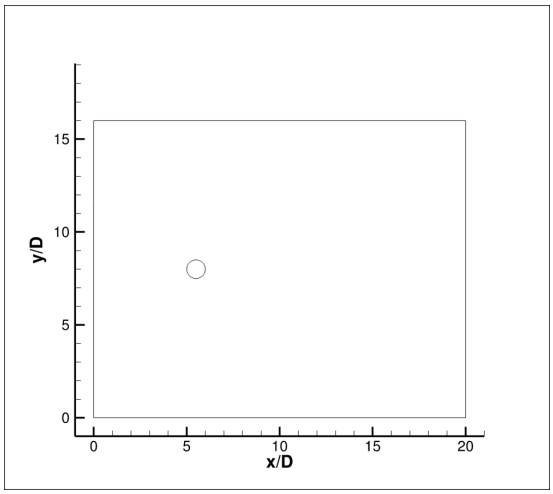

(a) Complete domain

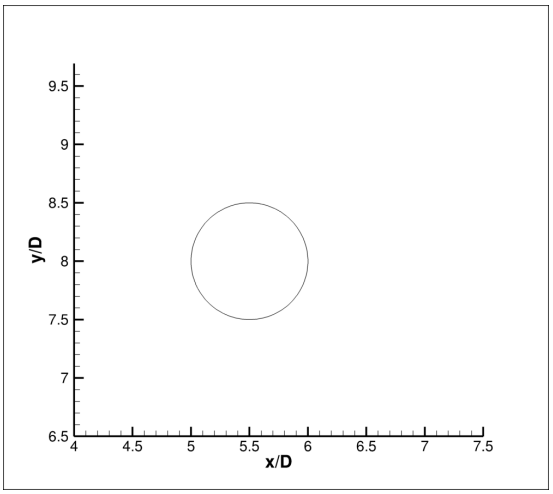

(b) Circular cylinder

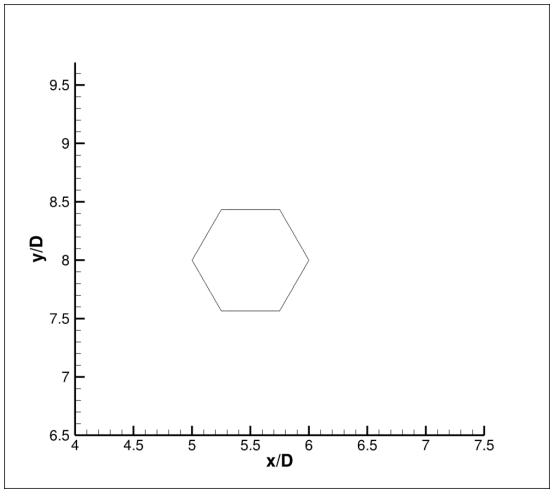

(c) Hexagonal cylinder with corner orientation

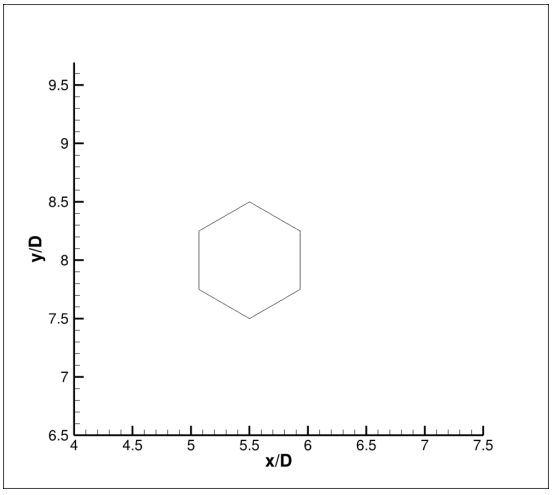

(d) Hexagonal cylinder with face orientation

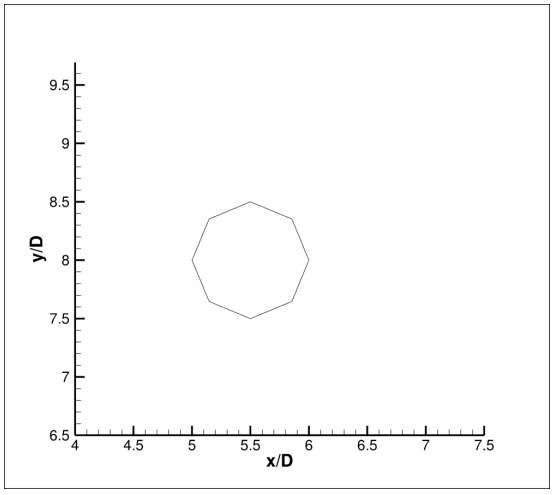

(e) Octagonal cylinder with corner orientation

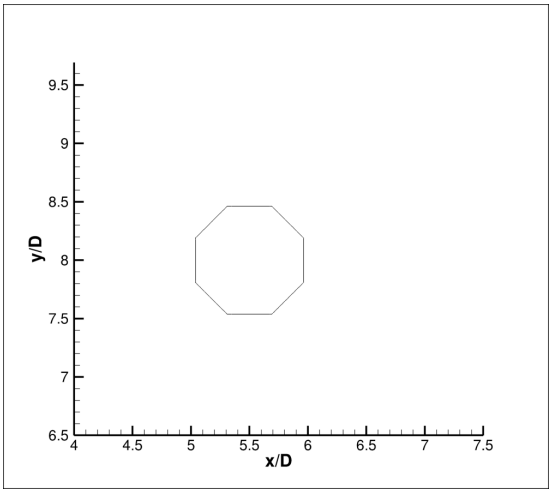

(f) Octagonal cylinder with face orientation

Figure 3.1: Computational Domains used for the first preliminary study. Figure (a) shows the complete domain. Figures (b)-(f) show close ups of the several geometries studied.

of a partially submersed object moving through water, is very low $Fr \approx 0.03$, which means that the wave length is much smaller than the length of the structure, meaning very low wavemaking

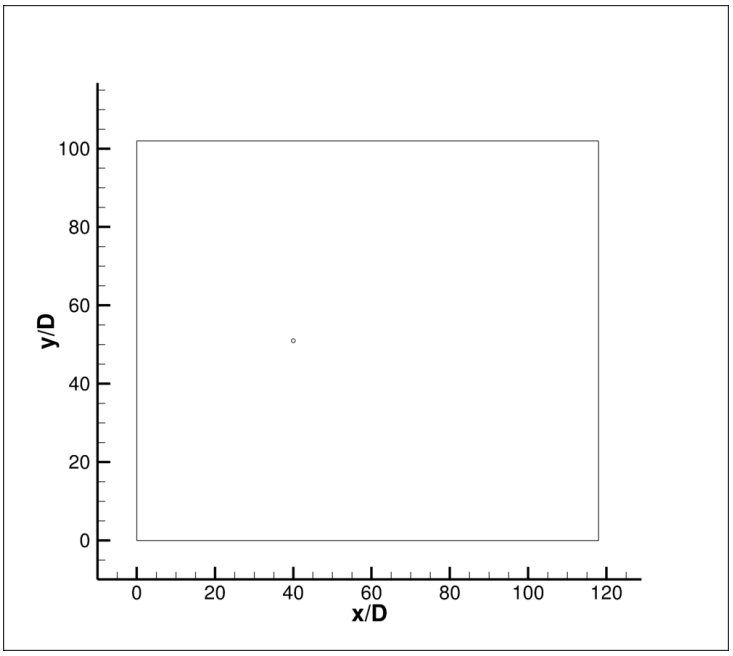

Figure 3.2: Example of a domain used in the second preliminary study: circular geometry.

resistance;

As the size of the domain used for the second preliminary study proved to minimize the interaction of the boundary conditions with the flow, the domain used in the main study kept the size ratio used in that study, however a scale of 1:1 was used, which means that, since the structure has a circumscribed diameter of $136.3m$, the outer limits of the domain are $16083.4m$ in the longitudinal (x) direction, $13902.6m$ in the transverse (y) direction and $6815m$ in the z-direction. The center of the structure is located $5452m$ away from the inlet and $6951.3m$ away from the lower part of the domain, as shown in Figure 3.3.

Figure 3.4 shows a close up of the aquaculture structure that is going to be simulated. Only the part of the floating collar that is under water was modelled. The collar has circumscribed diameter of $136.3m$, a height (z-direction) of $11m$ and a thickness of $3.10m$ at its thickest point. The net was modelled to be $60m$ high with a $15°$ tapper.

3.4 Boundary Conditions

For the preliminary studies, similar boundary conditions to those used by Khaledi and Andersson [2] were used:

- Imposed velocity at the inlet: uniform flow with streamwise velocity vector, $\tilde{\mathbf{V}} = (\mathbf{1}, \mathbf{0}, \mathbf{0})[m/s]$. k and ω are specified and pressure, p, is extrapolated from the interior assuming zero streamwise derivative.

  An inlet turbulent intensity of $I = 1 \times 10^{-2}$ gives $k = 1.5 \times 10^{-4} U_\infty^2 [m^2/s^2]$. Using $\frac{\nu_t}{\nu} = 0.01$, where ν_t is the kinematic eddy viscosity, ω follows from: $\omega = \frac{k}{\nu_t}[1/s]$;

- Mirror conditions at the side walls of the domain to simulate an infinitely long cylinder, $U_z = 0$;

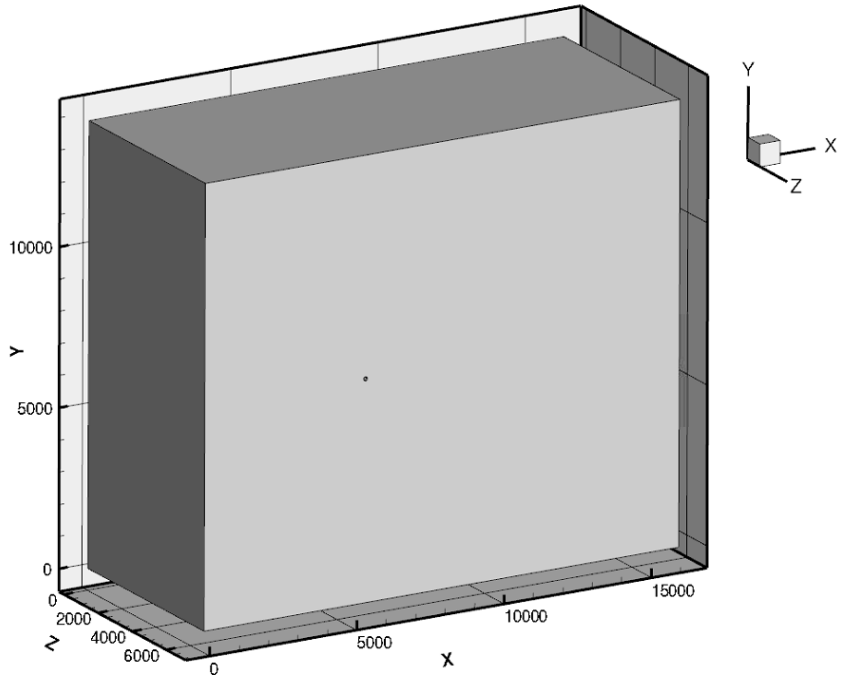

Figure 3.3: Domain used for the Study of Flow around the aquaculture structure.

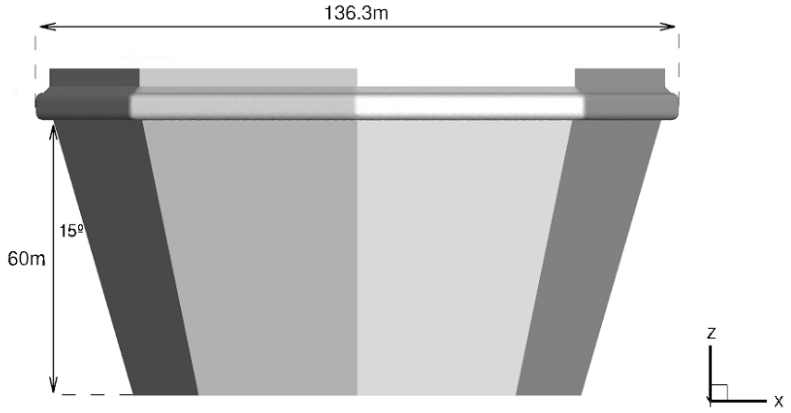

Figure 3.4: Close up of the aquaculture structure.

- Zero-pressure condition at the outlet of the domain and zero streamwise derivatives for the remaining quantities, $\frac{\partial \phi}{\partial x} = 0$;
- Free-slip conditions at the top and bottom boundaries: null normal velocity component ($U_y = 0$) and zero normal derivatives for the remaining quantities, $\frac{\partial \phi}{\partial y} = 0$.
- No-slip and impermeability condition at the wall of the cylinder. All velocity components equal to the wall velocity, $U_x = 0$ and $U_y = 0$, turbulent kinetic energy is zero, $k = 0$. Pressure derivative in the direction normal to the wall is assumed zero $\frac{\partial p}{\partial n} = \nabla p \cdot \overrightarrow{n} = 0$;

  For the second preliminary study the use of wall functions was tested. The determination of the

shear-stress at the wall τ_w and the specification of the ω boundary condition ($\omega \to \infty$ at the wall) represent the most challenging part of the wall boundary conditions in a turbulent flow. In the second preliminary study, two alternatives were tested [4]:

– **No wall functions (NO)**

In this approach τ_w is determined from its definition directly:

$$\tau_w = \mu \frac{U_{t2}}{(y_n)_2}, \tag{3.26}$$

where U_{t2} is the velocity component tangential to the wall at the near wall cell centre and $(y_n)_2$ is the distance from the near-wall centre to the wall. Close to the wall mean velocity profiles only remain linear for approximatly $y_n^+ < 5$ with

$$y_n^+ = \frac{u_\tau y_n}{\nu} \text{ and } u_\tau = \sqrt{\frac{\tau_w}{\rho}} . \tag{3.27}$$

So the value of y_{n2} should be smaller than one in order to guarantee an accurate solution of τ_w [22].

In order to avoid the singular behaviour of ω at the wall, the near-wall analytic solution of the ω transport equation [17] is used to specify ω at the near-wall centre

$$\omega_2 = \frac{6\nu}{\beta (y_n)_2^2} . \tag{3.28}$$

The value of ω at the boundary can be set equal to 10 times the value obtained from equation (3.28) [12], however that approach increases the numerical uncertainty of the shear-stress determination when compared to the use of equation (3.28) at the near-wall centre.

– **"Automatic" Wall Functions (WF)**

The so-called "automatic" wall functions blend the analytical equations of the linear and logarithmic layers to obtain expressions valid from the top of upper edge of the log layer down to the wall. Menter [23] proposes the following blend:

$$u^+ = \frac{U}{\tau_w} = \left(\left(\frac{1}{y^+} \right)^4 + \left(\frac{\kappa}{\ln(\mathrm{y^+E})} \right)^4 \right)^{-0.25} , \tag{3.29}$$

with $\kappa = 0.41$ and $E = 8.43$. Equation (3.29) is solved at the centre of the near-wall cells to determine τ_w.

With this approach $(y_n)_2$ may be located up to the outer edge of the log-layer (wherever it is located). However the main advantage of equation (3.29) is that it becomes equivalent to equation (3.26) when $(y_n^+)_2 < 1$. A robust implementation for the solution of the non-linear equation 3.29 can be found in[3].

With WF, ω is also specified at the centre of the near-wall cells using the blend proposed in [23]

$$\omega^{+} = \left(\left(\frac{6}{\beta \left(y^{+} \right)^{2}} \right)^{2} + \left(\frac{1}{\kappa \sqrt{C_{\mu}} y^{+}} \right)^{2} \right)^{0.5} , \tag{3.30}$$

where $C_{\mu} = 0.09$.

There are several alternatives for the turbulence kinetic energy boundary condition [3]. In the second preliminary study $k = 0$ is imposed at the wall and the k transport equation is solved with the production term in the near-wall cell determined from the shear-stress at the wall and the derivative of u^{+} with respect to y^{+} using equation 3.29. Although this is the best alternative proposed in [3], it must be mentioned that correcting the production term in the near-wall cell makes WF slightly different from NO even when the near-wall cell is inside the linear sub-layer.

An illustration of the application of these boundary conditions to the domains used for each of the studies is shown in Figure 3.5

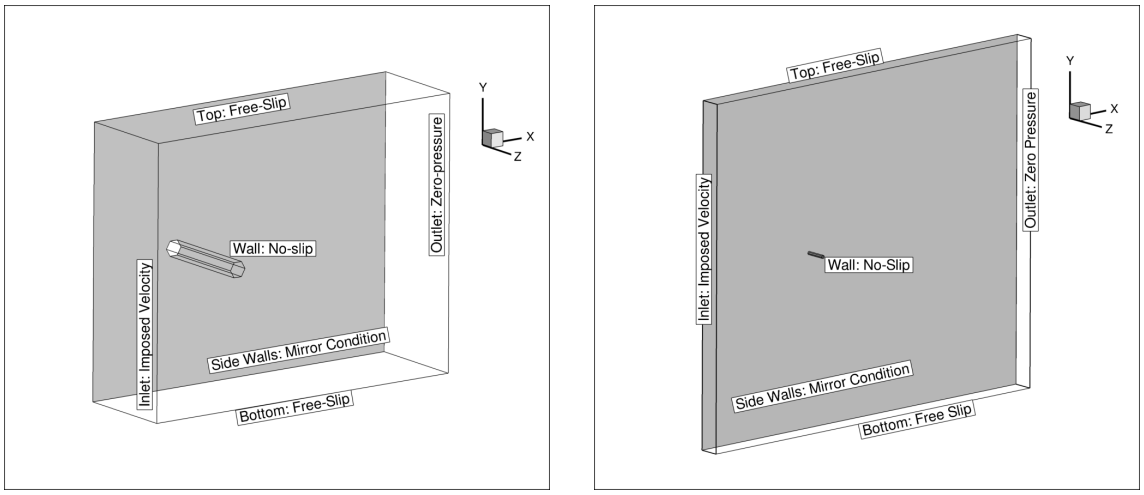

(a) First preliminary study

(b) Second preliminary study

Figure 3.5: Boundary conditions used for the preliminary studies

Due to the 3D nature of the main set of simulations, it was necessary to change the boundary conditions for the lateral boundaries of the domain as well as the free surface and domain floor:

- Imposed velocity at the inlet - same as previous;
- Mirror conditions at the water surface (no waves), $U_y = 0$;
- Zero-pressure condition at the outlet of the domain and zero streamwise derivatives for the remaining quantities - same as previous;
- Free-slip conditions at the longitudinal top and bottom of the domain and at the 'ocean floor': null normal velocity component and zero normal derivatives for the remaining quantities;
- No-slip and impermeability condition at the wall of the structure. "Automatic" wall functions were used as a consequence of the results obtained in the second preliminary study.

Figure 3.6 shows the application of such boundary conditions on the domain presented earlier.

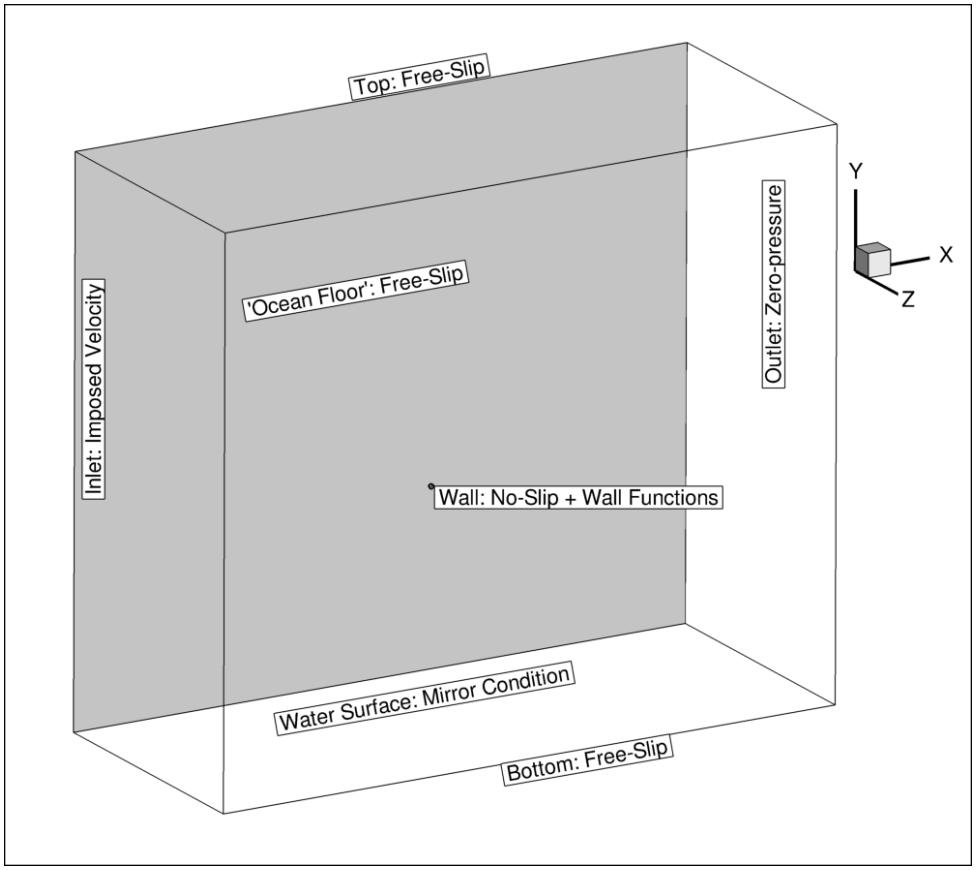

Figure 3.6: Boundary conditions used for the 3D Study.

Chapter 4

Solution Procedure

This chapter details the processes and tools used to obtain the results needed to achieve the objectives of this investigation.

To perform the simulations, the domains described above had to be generated using Computer-Aided Design (CAD) tools. Those domains had to be discretized using grid generation software and finally the parameters of the calculations had to be set up in a Computational Fluid Dynamics (CFD) Software that was used to obtain the solutions.

A description of the grids (spatial discretization) and time steps (temporal discretization) used for the preliminary studies as well as the main calculations is also presented in this chapter.

Finally the quantities of interest, are defined for each one of the studies, bearing in mind the objectives of each study.

4.1 CAD software - SOLIDWORKS

The design of the domains used in this work was made using the CAD software SOLIDWORKS®, and later transferred to a grid generation software that discretized each domain.

”SOLIDWORKS leads the global 3D CAD industry with easy-to-use 3D software that trains and supports the world’s engineering and design teams as they drive tomorrow’s product innovation.” - taken from the official website [24].

4.2 Grid Generation Software

4.2.1 Unstructured Grids - HEXPRESS

The complexity of the geometry of the aquaculture structure makes it difficult to generate structured grids with the adequate robustness. So an alternative was used: a grid generation software that creates unstructured grids. The software selected was NUMECA’s HEXPRESS™ software. ”HEXPRESS™ generates non-conformal body-fitted full hexahedral unstructured grids on complex arbitrary geometries.

In addition, the advanced smoothing capability provides high-quality boundary layers insertion." - taken from the official website [25].

Grid Refinement

Unstructured grids present advantages over structured grids, particularly in regards to grid generation, since they are capable of adequately handle complex geometry, are faster and require less grid generation experience. However, grid refinement is more challenging in unstructured grids than in structured ones. One of the challenges tackled in the first preliminary study was the influence of grid refinement of an unstructured grid in the solution and convergence. The grid refinement method tested in the first preliminary study was formulated by Crepier to obtain grids as geometrically similar as possible when dealing with unstructured grids [26]:

1. The initial cell size is decreased by a factor 2, 3, 4 and 5 in each direction by using 2,3,4 or 5 times more cells in each direction.
2. The surface refinement degree is kept constant throughout the sets: if, for instance, 6 refinements levels are set in the initial coarse grid, the same 6 successive refinements are performed for the other grids.
3. The size of the transition region, so-called diffusion depth d, is adapted such that it matches the expected final size of the grid.
4. The anisotropic sub-layer settings are adapted to account for the refinement performed.

This process can only be explained by understanding how the HEXPRESS™ software deals with refinement. In this software an initial grid is created by choosing the amount of cells in the x, y and z directions, then criteria for refinement are selected (for example, in surface refinement, one or more surfaces are chosen and cells intercepting those surfaces are selected for refinement). Refinement in HEXPRESS™ happens in levels. In each level, the base cell is divided in 2^n cells isotropically, in the three directions. The diffusion depth, d, is an input of the software that determines that cells neighbouring those that are selected for refinement will also be refined, i.e, if the diffusion depth is 2 that means that the immediate neighbours of the cells intercepting the surface (assuming that surface refinement is being used) will also be refined; if d is set to 3 that means that not only the neighbours of those cells but also the neighbours of the neighbours will be flagged for refinement. A 2D example of this can be seen in figure 4.1.

As detailed by Crepier [26], the size of the cells in the anisotropic sub-layer in HEXPRESS™ follows a geometric series of first term S_0 (first cell size) and ratio r:

$$S_n = S_0 r^n. \tag{4.1}$$

Crepier further explains that this definition means that dividing the initial cell size, and keeping the ratio constant in all grids will not result in geometrically similar grids. To that effect the first cell size and stretching ratio should be adapted following equations (4.2) and (4.3):

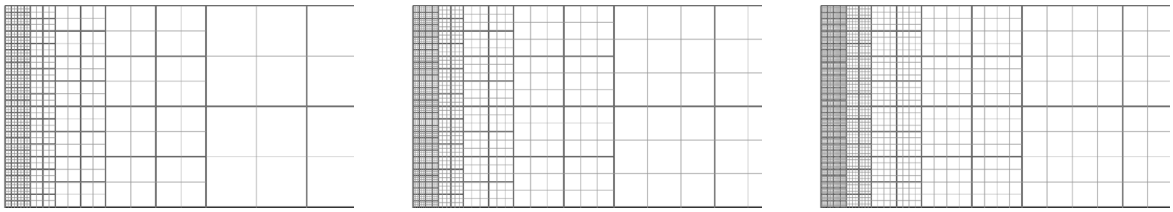

(a) 2 refinement levels (b) 3 refinement levels (c) 4 refinement levels

Figure 4.1: Example of volume grid refinement. Black lines: initial coarse grid; Grey lines: refined grid [26].

$$S_n = S_0 \frac{1 - r_1^{\frac{1}{n}}}{1 - r_1}, \tag{4.2}$$

$$r_n = r_1^{\frac{1}{n}}, \tag{4.3}$$

where S_0 and r_1 are the first cell size and the growth ratio in the initial coarse grid, respectively and S_n and r_n the first cell size and growth ratio for the grid refinement n, n=1 corresponding to the coarsest grid [26].

4.2.2 Structured Grids

As previously stated, the second preliminary study did not use unstructured grids, since the objective of the study was to test the effects of using wall functions in simulations of flow around bluff bodies at a Reynolds number of $Re = 10^8$. Instead the *Grid Generation Tools for Structured Grids* [5] were used to obtain the grids necessary for the study.

4.3 CFD Software - ReFRESCO

The software used to perform the necessary simulations throughout this work is ReFRESCO (v2.5). ”ReFRESCO is a viscous-flow CFD code that solves multiphase (unsteady) incompressible flows using the Navier-Stokes equations, complemented with turbulence models, cavitation models and volume-fraction transport equations for different phases. The equations are discretised using a finite-volume approach with cell-centered collocated variables, in strong-conservation form, and a pressure-correction equation based on the SIMPLE algorithm is used to ensure mass conservation. Time integration is performed implicitly with first or second-order backward schemes. At each implicit time step, the non-linear system for velocity and pressure is linearised with Picard’s method and either a segregated or coupled approach is used. In the latter, the coupled linear system is solved with a matrix-free Krylov subspace method using a SIMPLE-type preconditioner. A segregated approach is always adopted for the solution of all other transport equations. The implementation is face-based, which permits grids with elements consisting of an arbitrary number of faces (hexahedrals, tetrahedrals, prisms, pyramids, etc.), and if needed h-refinement (hanging nodes).” - taken from the official website [27].

4.3.1 Computational Model

The numerical setup of the transport equations must be established in the early stages of any CFD calculation. In the present case the transport equations are for momentum, mass (pressure) and turbulence as no model for transition was considered. Implementation of the numerical model include the following parameters [6]:

- **Linear equation solver and mass-momentum solver.** - The three transport equations mentioned earlier are solved in the form $A\phi = RHS$, where A is the left-hand side matrix, ϕ is the variable or vector that the equation is being solved for and RHS is the right hand side vector of the equation. This means a systematic procedure has to be selected to calculate the solution of each linear equation: ReFRESCO uses a PETSc (Portable, Extensible Toolkit for Scientific Computation) solver, which is a set of routines and data structures used for the numerical solution of partial differential equations for scientific applications. It provides computational routines for parallel matrix and vector assembly which are valuable mechanisms in parallel application codes.

  An additional procedure is needed to couple the linear systems of the momentum and mass (pressure) equations;

- **Convergence tolerance** - This parameter specifies, in each time step, the precision to which the solution of each linear equation needs to be computed to;

- **Relaxation Procedure** - Each equation being solved has an initial guess for the solution. This guess is updated as the simulation runs. An **explicit under relaxation procedure** allows to alter the amount by which that initial guess is updated. While an **implicit under relaxation procedure** allows to control the ”stiffness” associated with the matrix A of each linear equation by increasing the matrix diagonal and the right-hand side (RHS) of the equation. This allows to ensure that the numerical scheme being implemented is capable of producing a solution.

  Regarding **explicit relaxation**, the explicit under relaxation factor, α_{exp}, weighs the contribution of the solution in the previous iteration by applying the following rule:

$$\phi^{n+1} = \phi^n + \alpha_{exp}\left(\phi^{n+1*} - \phi^n\right), \tag{4.4}$$

  in which ϕ^{n+1*} is the predicted solution at the new non-linear iteration, ϕ^{n+1} is the used solution at the new non-linear iteration, and ϕ^n is the solution at the previous iteration. This factor should, ideally, be as high as possible to ensure the fastest convergence possible (provided that the stability of the scheme is maintained).

  The following values were chosen, through a trial and error process, to be used as the initial values of explicit relaxation. They were, however, tuned to better fit each specific simulation:

  - Momentum equation: **0.8**
  - Turbulence equation: **0.75**

– Pressure (Poisson) Equation: **0.4**

In what concerns **implicit under relaxation**, the factor α_{imp} is introduced to modify (increase) the left hand side matrix's (A) diagonal and the RHS of the linear equation being solved:

$$\left(A_{ij} + \left(\frac{A_{ii}}{\alpha_{imp}} - A_{ii}\right)\right)\phi_j^n = RHS_i + \left(\frac{A_{ii}}{\alpha_{imp}} - A_{ii}\right)\phi_j^{n-1}, \tag{4.5}$$

Equation (4.5) applies to the non-linear problem at each time step. ReFRESCO allows to chose a minimum and maximum value for the implicit relaxation factor, as well as the number of iterations over which the minimum value must be increased until it reaches the maximum value. Convergence is usually quicker for high implicit relaxation factors, however lower values increase stability. It was empirically determined that **0.9** was an appropriate starting point value for both minimum and maximum relaxation factors, for both momentum and turbulence equation, but similarly to the values chosen for explicit relaxation, this value was also altered to adapt to each simulation.

- **Convective flux discretisation** - The momentum and turbulence equations both contain convective terms and as such, a discretisation scheme must be selected for those terms. Of the several schemes provided by *ReFRESCO*, the **LIMITED QUICK** scheme, which is a QUICK scheme with a flux limiter was used for the discretisation of the convective term in the momentum equation and a **first order upwind** scheme was used for the convective flux discretisation of the turbulence equation. The choice of these schemes guarantees that the flux values are always positive;

- **Time integration scheme** - An implicit three-time level (2nd order) scheme was used to perform time integration for all equations, with the exception of turbulence, on which a first order scheme was used to ensure robustness.

4.4 Spatial Discretisation

This section describes the grids used for spatial discretisation of the domains used for both the preliminary studies and the main simulations.

4.4.1 Preliminary Study 1

15 grids were generated in HEXPRESS™ for the first preliminary study. Three sets of grids for the domain with the circular cylinder, six sets of grids for the domain with an hexagonal cylinder and other six sets for the domain with an octagonal cylinder (three sets for corner orientation and three for face orientation). Examples of some of the grids used are shown in Figure 4.2, and two important parameters to characterize the grids, total number of cells, N_v, and number of faces in the surface of the cylinder, N_f are included in Table 4.1. Additionally, the grid refinement ratio, $r_i = h_1/h_i$, for the grids used in this

first preliminary study is presented in Table 4.2. The grid refinement ratio is obtained from

$$r_i = h_i/h_1 = \left(\frac{N_{v1}}{N_{vi}}\right)^{1/2} = \frac{N_{f1}}{N_{fi}} \ . \tag{4.6}$$

Table 4.1: Number of volumes N_v and number of cell faces on the surface of the cylinder N_f of the grids of the first preliminary study.

Grid		Circle	Hexagon		Octagon	
			Corner	Face	Corner	Face
1	N_v	122090	115228	121274	125789	118924
	N_f	1346	1230	1308	1362	1260
2	N_v	67354	64888	66924	68344	66396
	N_f	808	744	790	824	766
3	N_v	61372	31856	33342	33664	29590
	N_f	538	502	530	554	516

Table 4.2: Grid refinement ratio, r_i, of the grids of the first preliminary study.

Grid	Circle	Hexagon		Octagon	
		Corner	Face	Corner	Face
1	1.	1.	1.	1.	1.
2	1.666	1.653	1.656	1.653	1.645
3	2.502	2.450	2.468	2.458	2.442

4.4.2 Preliminary Study 2

As stated above, for the second preliminary study structured grids were used instead of unstructured ones, since the objective was to study the influence of wall function in the solution and the 2D grids without wall functions generated in HEXPRESS™ did not present the necessary quality.

Four sets of geometrically similar grids were generated to discretize the computational domain described in section 3.3.2. The multi-block structured grids were generated with algebraic and elliptic grid generators described in [28]. The grid is orthogonal to the surface in the near-wall region and the selected topology intends to cluster cells in the near-wake region and expand the cell size at the top, bottom and outlet to avoid pressure reflections. The first set of grids (GNO) is tunned to calculate τ_w from its definition which means using the NO wall boundary conditions described in section 3.4. Figure 4.3 illustrates the grid topology as well as views from the coarsest grid of the GNO set for the circular cylinder [4].

The remaining 3 sets are obtained by merging cells in the near-wall region keeping the cell height of all the grids of the same set constant. In [29] it is reported that for a flat plate flow the value of τ_w obtained with WF depends on $(y_n)_2$. Although the aerodynamic forces of the present flows are dominated by the

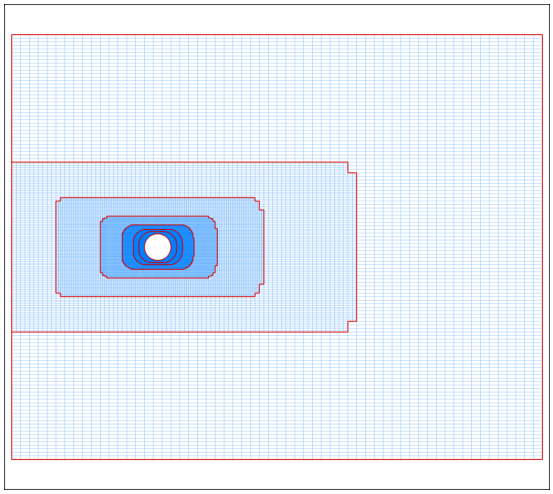

(a) Complete domain discretization

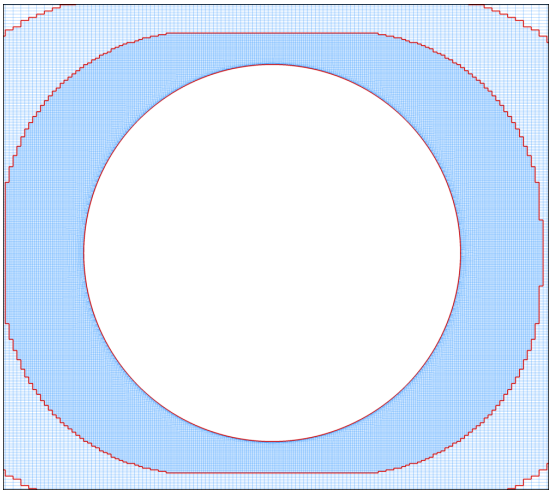

(b) Circular cylinder

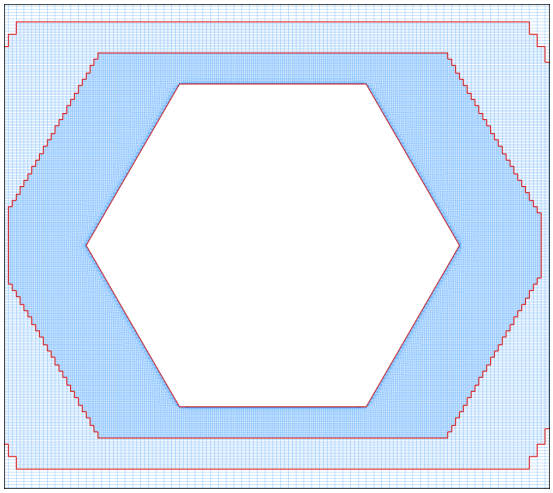

(c) Hexagonal cylinder with corner orientation

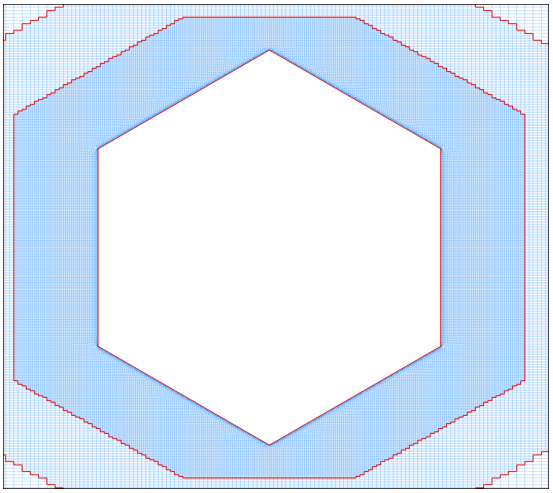

(d) Hexagonal cylinder with face orientation

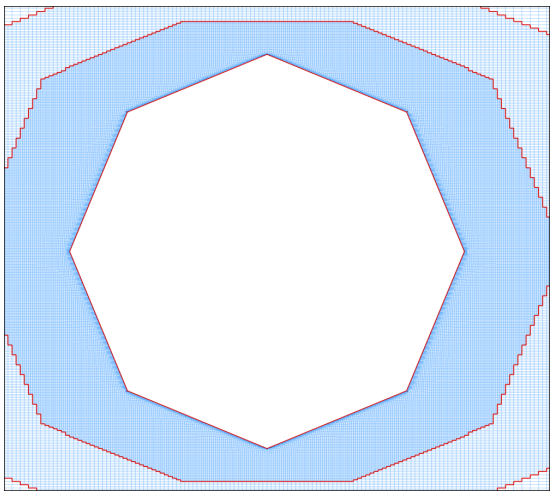

(e) Octagonal cylinder with corner orientation

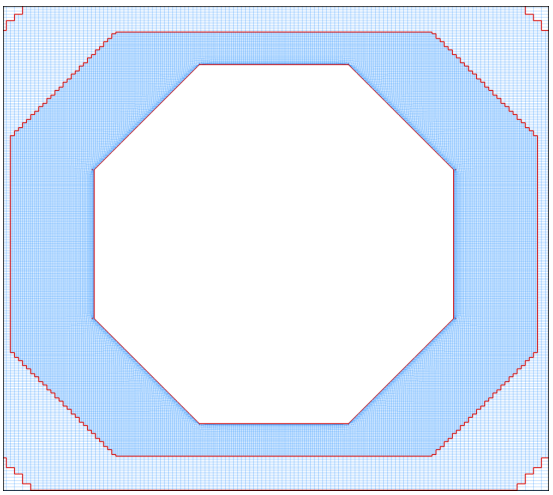

(f) Octagonal cylinder with face orientation

Figure 4.2: Finest grids (Grid 1) used for the first preliminary study. Figure (a) shows the complete discretization of the domain for the circular cylinder case. Figures (b)-(f) show close ups of the several geometries used.

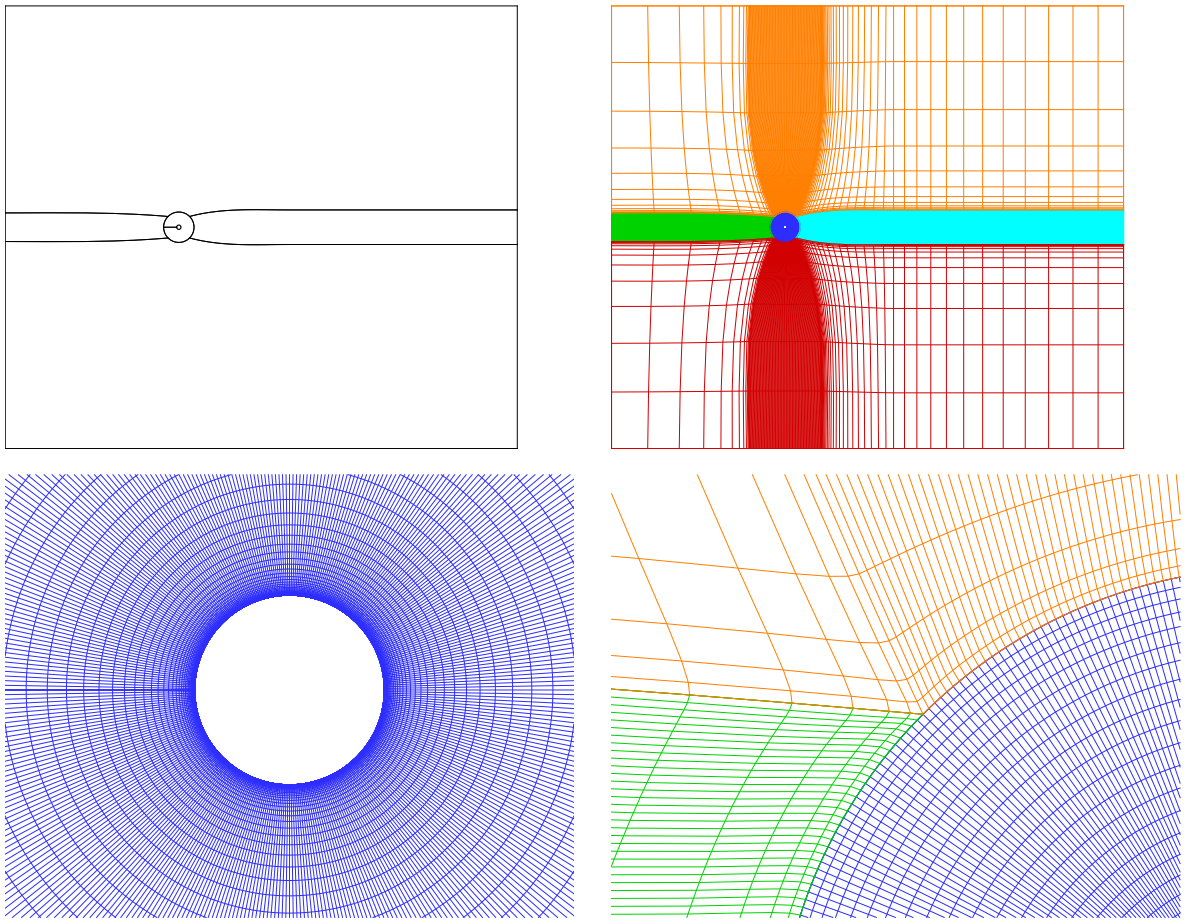

Figure 4.3: Illustration of the grid topology and different views of the coarsest grid of set GNO of the multi-block structured grids for the calculation of the flow around a circular cylinder at a Reynolds number of 10^8 without wall functions.

pressure component, their magnitude is essentially dependent on the location of the separation points. Consequently, in this work three different values of the near-wall cell size were tested for the application of WF in sets GWF1, GWF2 and GWF3. The number of cells merged in the near-wall region of the inner block are 1/4 (GWF1), 3/8 (GWF2) and 1/2 (GWF3) of the cells in the direction perpendicular to the surface of the cylinder. Figure 4.4 illustrates, for the coarsest grids of the four sets generated for the circular cylinder, the region close to wall [4].

The total number of cells of each grid, N_v, the number of faces on the surface of the cylinder, N_f and the grid refinement ratio $r_i = h_i/h_1$ are presented in Table 4.3.

The grid generation strategy used for the octagonal and hexadecagonal cylinders was the same, with the number of faces on the body surface and the number of cells merges in the near-wall region for the GWF sets identical to those used for the circular cylinder. Figure 4.5 shows the coarsest grids of the GNO set for the polygonal cylinders [4].

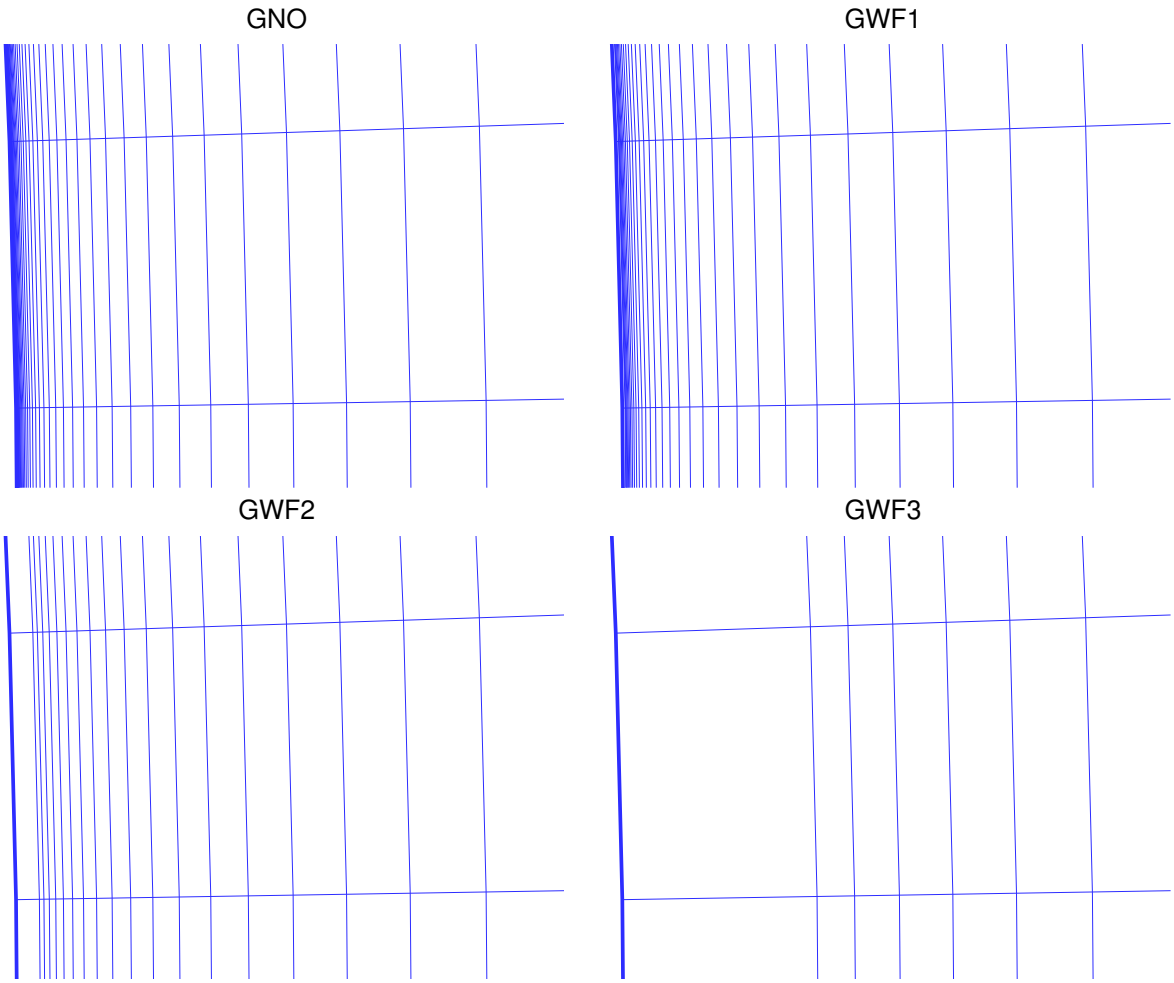

Figure 4.4: Near-wall grids of the coarsest grid of the sets GNO, GWF1, GWF2 and GWF3 of the multi-block structured grids for the calculation of the flow around a circular cylinder at a Reynolds number of 10^8 with and without wall functions.

Table 4.3: Number of volumes N_v, number of cell faces on the surface of the cylinder N_f and grid refinement ratio h_i/h_1 of the grid sets GNO, GWF1, GWF2 and GWF3 of the multi-block structured grids for the calculation of the flow around a circular cylinder at a Reynolds number of 10^8 with and without wall functions.

Grid	h_i/h_1	N_f	N_v			
			GNO	GWF1	GWF2	GWF3
1	1.	896	244608	194432	169344	144256
2	1.16(6)	768	179712	142848	169344	105984
3	1.4	640	124800	194432	169344	73600
4	1.75	512	79872	194432	169344	47104
5	2.	448	61152	194432	169344	36064
6	2.3(3)	384	44928	194432	169344	26496

4.4.3 3D Study

For the simulation of flow around the 3D aquaculture structure, three grids were generated using HEXPRESS™.

As a consequence of the results of the second preliminary study, wall functions were used and no

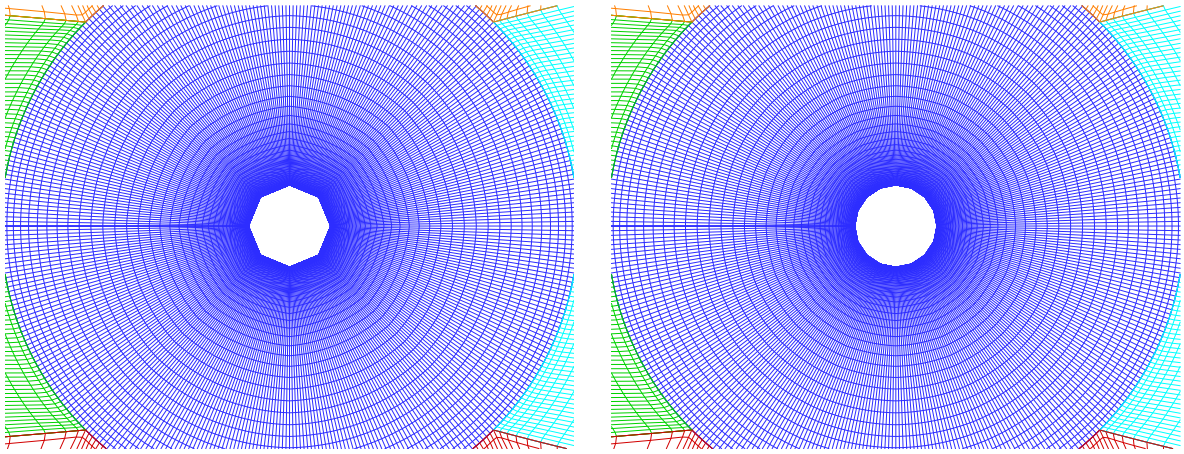

Figure 4.5: Illustration of the coarsest grid of set GNO of the multi-block structured grids for the calculation of the flow around a octagonal and hexadecagonal cylinder at a Reynolds number of 10^8 without wall functions.

viscous layer near the wall was introduced. Figure 4.6 shows details of the grids used in this study.

Table 4.4 shows the total number of cells, the number of faces on the surface of the structure and the grid refinement ratio of each one of the three grids.

Table 4.4: Number of cells N_v, number of face elements N_f and grid refinement ratio h_i/h_1 of the grids for the simulations performed with $Re = 10^8$ with 3D geometry

Grid	N_v	N_f	h_i/h_1
1	11 379 583	388 164	1.
2	3 504 780	185 390	2.094
3	988 237	86 364	4.495

4.5 Temporal Discretization

In all cases tested, the time scale was adapted inversely to the increase of number of face elements in each refinement, in order to guarantee an average Courant number, C_{avg} (ratio of the time scale to spatial scale multiplied by the local velocity), close to $C_{avg} = 1.2 \sim 1.5$. The Courant number gives an indication of the numerical stability of an unsteady simulation, as high values of C mean that the time step is too large for the size of the smallest spatial scales, which leads to significant time errors.

4.5.1 Preliminary Study 1

The values of the time steps, in seconds, used for each simulation of the first preliminary study are presented in Table 4.5.

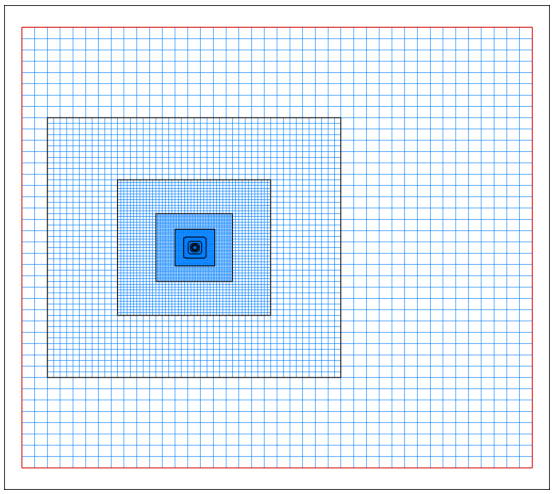

(a) Top-down view of the complete grid

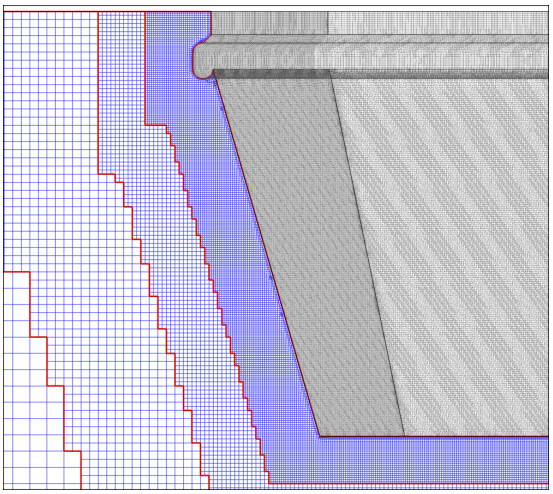

(b) Detail: side of the structure

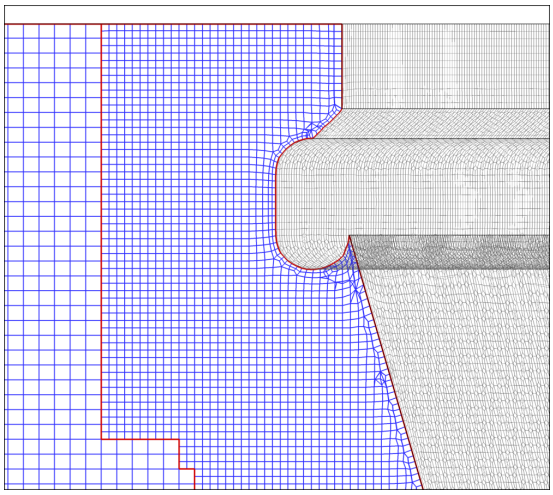

(c) Detail: bordure of the floating collar

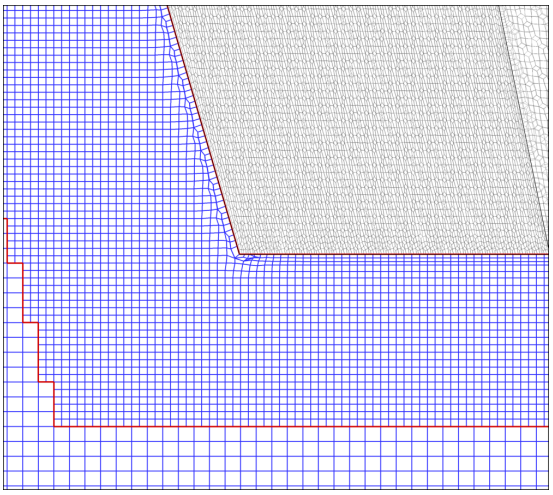

(d) Detail: bottom corner of the structure

Figure 4.6: Finest grid (Grid 1) used for the 3D study. Figure (a) shows the complete discretization of the domain in a top-down view. Figures (b)-(f) show close up details of relevant parts of the grid.

Table 4.5: Time scales of the simulations of the first preliminary study, in seconds

Grid	Circle	Hexagon		Octagon	
		Corner	Face	Corner	Face
1	0.007494	0.007652	0.007597	0.007627	0.007679
2	0.012485	0.012651	0.01258	0.012606	0.012631
3	0.01875	0.01875	0.01875	0.01875	0.01875

4.5.2 Preliminary Study 2

The time step for this study was selected to obtain a maximum Courant number around $C_{max} \approx 5$, which for the circular cylinder leads to an average C_{avg} close to $C_{avg} \approx 1.5$. The refinement studies performed for each set have a grid refinement equal to the time refinement ratio. The values of maximum Courant number C_{max} of the circular cylinder simulations as well as the maximum non-dimensional near-wall cell height in wall coordinates $((y_n^+)_2)_{max}$, are presented in Table 4.6

Table 4.6: Maximum C_{max} Courant number and Number of volumes N_v, number of cell faces on the surface of the maximum non-dimensional near-wall cell height in wall coordinates $((y_n^+)_2)_{max}$ of the grid sets GNO, GWF1, GWF2 and GWF3 of the multi-block structured grids for the calculation of the flow around a circular cylinder at a Reynolds number of 10^8 with and without wall functions.

h_i/h_1	C_{max}				$((y_n^+)_2)_{max}$			
	GNO	GWF1	GWF2	GWF3	GNO	GWF1	GWF2	GWF3
1.	5.0	5.0	6.5	4.9	0.24	230	1940	16147
1.16(6)	4.9	4.9	6.2	4.9	0.28	231	1957	16304
1.4	5.0	4.9	5.6	4.8	0.34	236	2018	16457
1.75	5.0	5.0	5.3	4.9	0.43	243	2084	16996
2.	5.0	5.0	5.3	5.1	0.50	248	2136	17927
2.3(3)	5.0	4.9	5.3	4.8	0.59	253	2214	18280

As mentioned above, the values of $((y_n^+)_2)_{max}$ for the GNO set decrease with grid refinement, whereas for the GWF1, GWF2 and GWF3 sets the values of $((y_n^+)_2)_{max}$ remain approximately constant. However. the dependence of $((y_n^+)_2)_{max}$ on the shear-stress at the wall τ_w generates a small change of $((y_n^+)_2)_{max}$ with grid refinement for the wall functions sets.

Initial conditions, whenever possible, were interpolated from a converged solution obtained in a different grid for the same geometry. For the coarsest grid of each grids set, the initial approximation is obtained from the inlet conditions except for the pressure field that is set equal to the value at the outlet. This means that the simulation must be sufficiently long to eliminate the influence of the initial condition.

4.5.3 3D Study

Table 4.7 shows the time scale, in seconds, used for each simulation performed with the 3D geometry, as well as the average and maximum Courant numbers of the simulations.

Table 4.7: Time scales of the simulations performed with $Re = 10^8$ with 3D geometry, in seconds

Grid	Time Scale	C_{avg}	C_{max}
1	0.66375	1.42	16.2
2	0.9825	1.42	15.5
3	1.5	1.42	14.6

To illustrate the computational power used for these simulations, Table 4.8 presents the number of processors used for each simulation, as well as the computation time of the whole simulation, in seconds.

4.6 Quantities of Interest

Since each study had its own objectives different from each other it is important to outline the relevant parameters that need to be analysed in each case.

Table 4.8: Number of processors N_{proc} and computation time t_{comput}, in seconds for the simulations with $Re = 10^8$ with 3D geometry.

Grid	N_{proc}	t_{comput} $[s]$
1	400	1.009876E+06
2	260	3.841356E+05
3	140	4.030541E+05

4.6.1 Preliminary Study 1

The first study aims to compare results with the ones obtained by Khaledi and Andersson [2], understand the impact of unstructured grids and their refinement on the solution and on the numerical robustness of the simulation itself and study the influence of the body shape in the numerical convergence properties. As such the quantities to be analysed are:

1. Average force coefficients ($C_{D_{avg}}$ and $C_{L_{avg}}$) and their evolution through time (time history), obtained from the total forces in the x and y directions:

$$C_D = \frac{D}{\frac{1}{2}\rho U_\infty^2 d}, \tag{4.7}$$

$$C_L = \frac{L}{\frac{1}{2}\rho U_\infty^2 d}, \tag{4.8}$$

   For flows around bluff bodies C_L and C_D change with time. Thus their behaviour will be described using the average and root mean squared (rms) values obtained from the last n cycles of the simulations, where n is selected through statistical convergence criteria;

   The average value of the time history of a variable ϕ is obtained from

$$\phi_{(avg)} = \frac{\int_{t_b}^{t_e} \phi(t) dt}{t_e - t_b}\ , \tag{4.9}$$

   where ϕ stands for any flow quantity and t_b and t_e are the beginning and the end time of the last n cycles simulated, respectively. The rms value is obtained from

$$\phi_{rms} = \sqrt{\frac{\int_{t_b}^{t_e} \left(\phi(t) - \phi_{avg}\right)^2 dt}{t_e - t_b}}\ . \tag{4.10}$$

   The integrals included in equations (4.9) and (4.10) are determined with second-order trapezoidal rules.

2. Strouhal number, obtained through an FFT (*Fast Fourrier Transform*) tool available in TecPlot [30], as a means of comparison with the literature;

3. Instantaneous streamline patterns to study vortex dynamics and the formation of turbulent structures in the wake of the cylinder;

4. Average Courant number to evaluate the presence of errors caused by an imbalance between the temporal and spatial scales;

5. Convergence properties of each simulation

   Statistical error - In statistically unsteady RANS simulations, statistical errors are a consequence of an incorrect initial condition. Assessing statistical errors is only straightforward if the mean flow solution is periodic, which is expected for all the test cases used in this study. However, as discussed in [31], there is no guarantee that the turbulence model provides the correct amount of diffusion (the role of the Reynolds stresses) to damp all the turbulent fluctuations. In this work a "cycle" is defined by the interval between the two time steps where the lift coefficient C_L is equal to zero and $dC_L/dt > 0$. Statistical convergence is quantified from the changes in average, maximum and root mean squared values of C_L in the last n cycles performed. Statistical convergence is assumed to occur when these changes are at the level of iterative convergence criteria used at each time step. [4]

   Iterative Convergence Criteria- The iterative convergence is monitored from the normalized residuals of all transport equations included in the determination of the flow field at each time step, i.e. x and y momentum equations, pressure correction (continuity) and turbulence transport equations. The normalization of the residuals is performed with the main diagonal of the system of equations and reference quantities based on ρ, L and V_∞. With this approach, the residuals correspond to dimensionless variables change in a simple Jacobi iteration.

   The statistical convergence is assessed for $C_{D_{avg}}$ and the period T of the last n cycles of the simulations using the simplest technique proposed in [32], which calculates the uncertainty of the mean value of a time signal from the standard deviation of the mean values obtained from equally-sized segments of the time interval defined by the number of cycles n.

   The discretization uncertainty is estimated using power series expansions [33] fitted to the data obtained from the grid/time refinement studies performed for each test case. As discussed in [34], the use of equal grid and time refinement ratios enables the use of the procedure described in [33].

4.6.2 Preliminary Study 2

The second preliminary study has as objective to understand the impact of wall functions in the simulation, so one of the main interests lies in the convergence properties of the simulation.

The relevant quantities are:

1. Average Force coefficients C_D, C_L and their time history;

2. Frequency content of the time histories, by means of an FFT and Strouhal number, St;

3. The time history of the main Cartesian velocity components U_x and U_y at two points in the near wake for the three geometries considered: P_1 has coordinates $x = 1.75d, y = 0$ and P_2 is located at $x = d, y = 0.75d$. The interpolation is performed using the value and the gradient at the nearest cell-centre.

$$\phi_P(t) = \phi_{nc}(t) + \nabla\phi_{nc}(t) \cdot (\vec{x}_P - \vec{x}_{nc}) \ , \tag{4.11}$$

where ϕ designates any of the Cartesian velocity components and $\vec{x}$ the positions of the selected location $_P$ and nearest cell centre $_{nc}$. Figure 4.7 shows the location of P_1 and P_2 in the near wake of the circular cylinder. The objective of monitoring these quantities is to check if the numerical solution exhibits a "RANS-like" behaviour, i.e. the FFTs of the velocity plots exhibit only significant amplitudes for discrete frequencies and to assess if statistical convergence of the force coefficients also implies statistical convergence of local flow quantities.

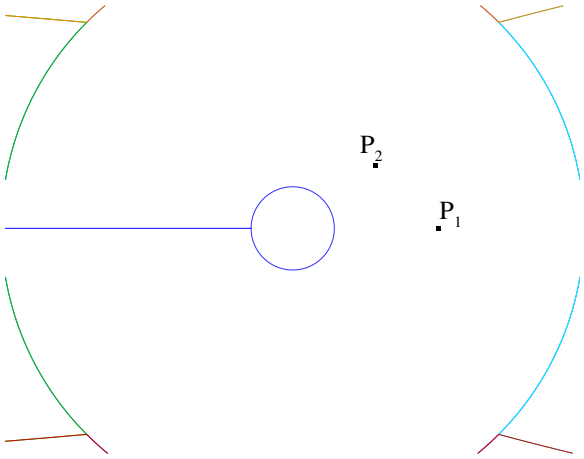

Figure 4.7: Selected locations for the assessment of the time histories of the mean Cartesian velocity components V_x and V_y. Flow around a circular cylinder at a Reynolds number of 10^8.

4. Iterative convergence properties of the simulations

   For all the simulations performed for the circular cylinder, the largest residual of all transport equations (L_∞ norm) was dropped to values below 10^{-6} at each time step. This value was selected after comparing results obtained with iterative convergence criteria of 10^{-3}, 10^{-5} and 10^{-6}. As discussed later, the iterative convergence of the octagonal and hexadecagonal cylinders is a lot more difficult than for the circular cylinder, especially for the GNO and GWF1 grids. Therefore, simulations performed in the GWF2 and GWF3 used 10^{-5} for the L_∞ norm of the normalized residuals, whereas some of the results presented for the GNO and GWF1 sets were obtained with a less strict iterative convergence criteria that required thousands of iterations at each time step.

4.6.3 3D Study

The final and main study wants to study the forces and moments with respect to the center of the structure acting on the structure in order to permit an accurate structural analysis in future studies. So,

naturally, the interest lies with:

1. Time history of the forces in the three directions and respective average values;
2. Time history and average moments acting in the three directions;
3. Frequency content analysis of the signals of the time histories.

The 3D force and moment coefficients were obtained from the total forces and moments in the respective directions making use of:

$$C_{F_i} = \frac{F_i}{\frac{1}{2}\rho U_\infty^2 A}, \tag{4.12}$$

and

$$C_{M_i} = \frac{M_i}{\frac{1}{2}\rho U_\infty^2 A d}, \tag{4.13}$$

where A is the impinging area of the structure, which is approximately $A = 8712.5m^2$.

Chapter 5

Results

In this chapter, the results from the two preliminary studies will be presented and analysed keeping in mind that the main objective of those studies is to chose the best possible settings for the main 3D study of flow around the aquaculture structure. The results of the main study will also be presented and analysed. Since the goal of this work is to provide information (forces and moments) for future studies such as a structural analysis of the aquaculture floating ring, the results of the main study will be presented taking that into account (for example, in addition to analysing the forces and moments coefficients, the total forces and moments will also be presented).

5.1 Preliminary Study 1

It bears repeating that the objective of this particular study was to test the numerical robustness of the unstructured grids generated with HEXPRESS^{TM} and their refinement by comparing the results obtained with these grids to the ones obtained by Khaledi and Andersson [2]. It also aimed to check the numerical convergence properties of the simulation as a function of body shape.

5.1.1 Time History of the Forces and Average Force Coefficients

Obtaining the average force coefficients, $\overline{C_d}$ and $\overline{C_l}$, and studying the time history of the forces is useful to understand the behaviour of the flow as a consequence of the different cross-section shapes and orientations, as well as giving a basis to later obtain the Strouhal number.

To obtain the average values of the forces for each case a FORTRAN routine was created that is able to select the relevant part of the data set since it eliminates the effect of the initial condition by considering only the last cycles of the simulation. To do this, the routine determines each time that the value of the Lift coefficient changes sign from a negative to a positive number($C_L = 0$ and $dC_L/dt > 0$). The time interval between each negative-to-positive sign change is considered a cycle. The user sets the number of cycles to consider and only full cycles are considered for the calculation of the average, i.e. if the last cycle does not finish in a negative-to-positive sign change, that partial cycle is not considered

for the calculations. For this study the number of cycles considered for each simulation was adapted in order to obtain around 120 seconds of relevant data.

This study involved a great number of simulations. There are five geometries being evaluated, two turbulence models and there are three refinement levels generated, which gives a total of 30 simulations. From these simulations the evolution of the force coefficients through time was plotted for each case. Figure 5.1 shows the plots generated for all 5 geometries for the grid with the highest level of refinement using the $k-\omega SST(2003)$ model. The other plots were placed in Appendix A for the sake of brevity.

From these plots a difference in behaviour between the octagonal cylinders and the hexagonal cylinders is noticeable. The hexagonal cylinder, as a consequence of the smaller internal angles, shows a frequency behaviour much different from the circular cylinder, with several energetic frequencies interacting with the structure, particularly in the face orientation. The octagonal cylinder still has more than one frequency, but they are less energetic. This will be further analysed in the analysis of the Strouhal number.

These plots also give an idea of the average values of the coefficients for the various simulations. The exact values are present in Tables 5.1 and 5.2 for all the simulations performed for this study, as a function of cross-section shape of the cylinder and the turbulence model used.

Table 5.1: Average Drag coefficient for the simulations performed with $Re = 10^3$

Grid	Turbulence Model	Circle	Hexagon		Octagon	
			Corner	Face	Corner	Face
1	$k-\omega SST$	1.4957	1.6884	1.9913	1.8727	1.5489
	$KSKL$	1.4734	1.7109	2.0354	1.8563	1.5353
2	$k-\omega SST$	1.4918	1.7224	1.9978	1.7569	1.5383
	$KSKL$	1.4648	1.7462	2.0442	1.7368	1.5229
3	$k-\omega SST$	1.5102	1.7591	2.0232	1.7049	1.6012
	$KSKL$	1.4795	1.7778	2.1945	1.8640	1.5771

Table 5.2: Average Lift coefficient for the simulations performed with $Re = 10^3$

Grid	Turbulence Model	Circle	Hexagon		Octagon	
			Corner	Face	Corner	Face
1	$k-\omega SST$	4.1750×10^{-5}	-0.15637	0.31461	0.063454	2.6420×10^{-5}
	$KSKL$	1.8780×10^{-5}	0.11519	0.021897	1.9880×10^{-4}	2.7510×10^{-5}
2	$k-\omega SST$	1.5350×10^{-5}	0.15377	-0.30218	-0.16871	9.8530×10^{-5}
	$KSKL$	1.499×10^{-5}	0.11281	0.082789	0.0014072	1.0040×10^{-4}
3	$k-\omega SST$	1.612×10^{-5}	0.11378	-0.26432	-1.9404×10^{-4}	4.317×10^{-5}
	$KSKL$	1.664×10^{-5}	0.062869	-0.093386	2.1532×10^{-4}	3.946×10^{-5}

From the average values of the force coefficients it is evident that there is little difference between the several refinement levels for a given case, particularly in the average Drag coefficient. Larger differences between the refinement levels on the average Lift coefficient can be due to the fact that forces in the y-

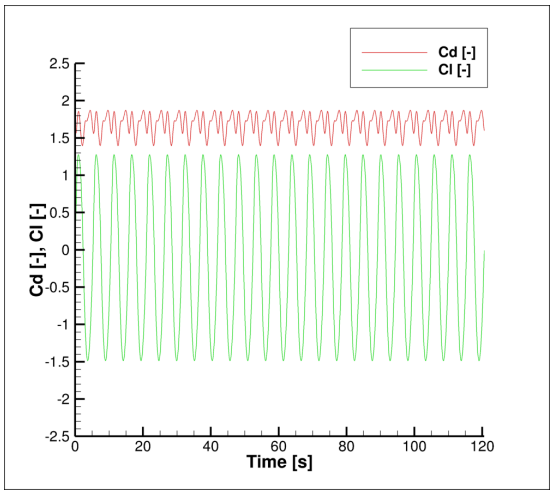

(a) Hexagonal cylinder with corner orientation

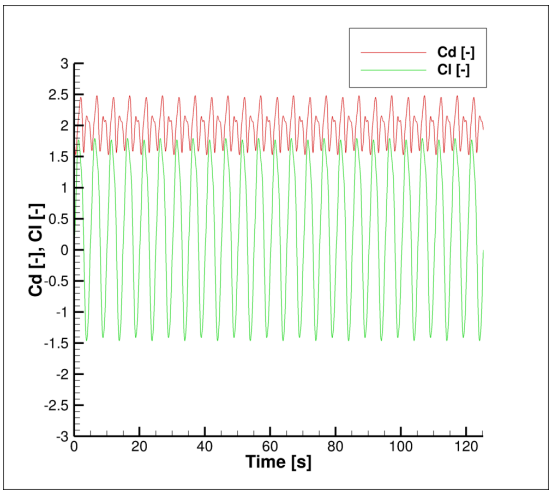

(b) Hexagonal cylinder with face orientation

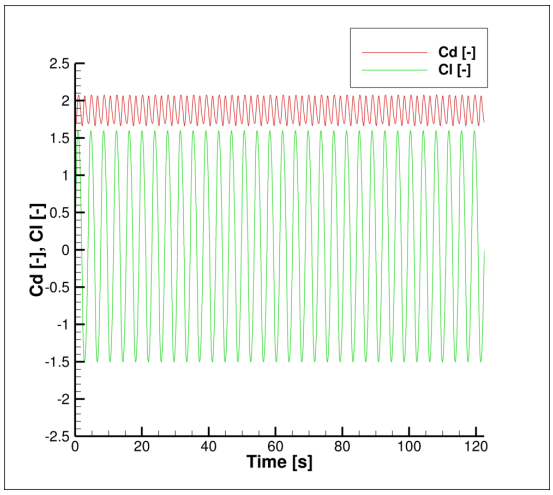

(c) Octagonal cylinder with corner orientation

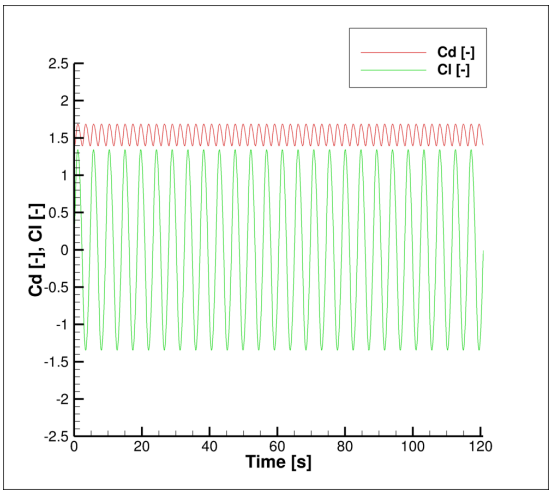

(d) Octagonal cylinder with face orientation

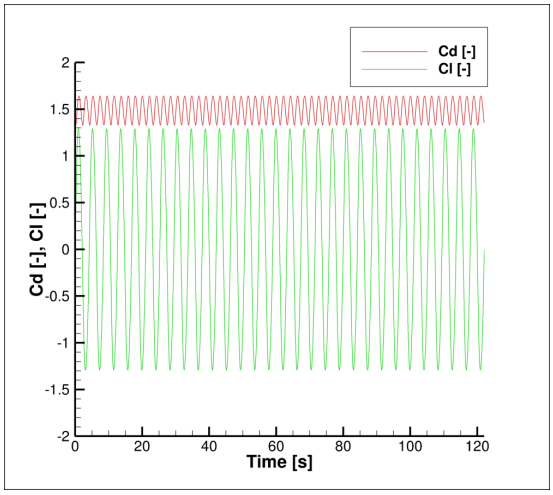

(e) Circular cylinder

Figure 5.1: Evolution of C_d and C_L for the simulations with the most refined grid (Grid 1) using the $k-\omega SST$ model

direction vary more heavily through time, when compared with the x-direction, due to vortex shedding and the recirculation bubbles formed close to the surface of the cylinder, which have special importance

in the polygonal cases.

5.1.2 Strouhal Number

The time history of the forces presented in the previous subsection allows to make some predictions about the important frequencies of the flow, such as the vortex shedding frequency. To prove those assumptions one may turn to a Fast Fourier Transform (FFT), which is a mathematical tool that allows to analyse the frequency content of a solution. The most energetic frequency - highest amplitude - in an FFT of the total forces in the y-direction, will be the vortex shedding frequency, i.e. the frequency at which each vortex leaves the wall of the cylinder as a recirculation bubble and travels along the wake. From that frequency, with the help of equation (2.1), one can extract the Strouhal number, commonly used to study this effect, since it represents an adimentional frequency. The FFT plots for the simulations performed with Grid 1 using the $k-\omega SST$ model are shown in Figure 5.2.

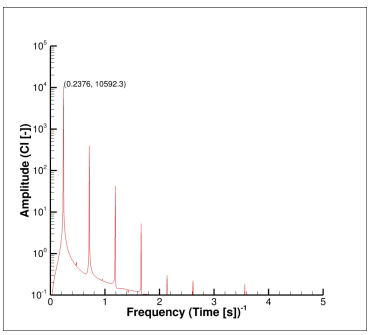

(a) Circular cylinder

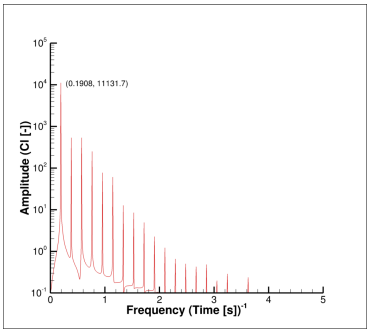

(b) Hexagonal cylinder with corner orientation

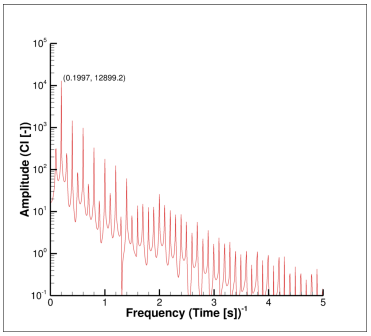

(c) Hexagonal cylinder with face orientation

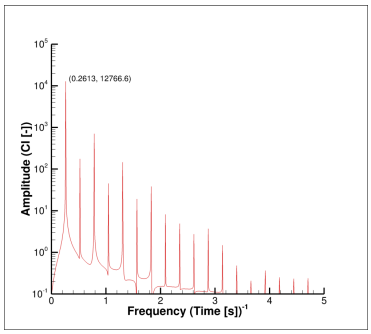

(d) Octagonal cylinder with corner orientation

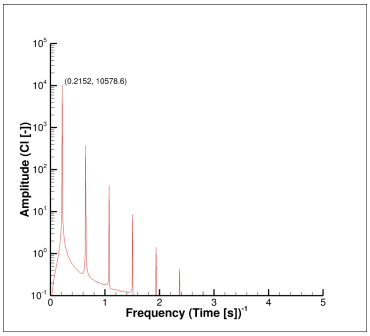

(e) Octagonal cylinder with face orientation

Figure 5.2: Fast Fourier Transfom plots obtained from the simulations with Grid 1 using the $k-\omega SST$ model.

In Figure 5.2, the frequency with the highest amplitude is the vortex shedding frequency, while the other peaks are harmonic frequencies of that first energetic frequency. The figure makes evident the difference between the different cross-sections of the cylinders: the circular cylinder, as the smoothest surface has little in terms of frequency content, as would be expected, both the hexagonal and octagonal cylinder have richer frequency spectra, particularly the hexagonal cylinder with face orientation. The octagonal cylinder is more similar in terms of frequency content to the circular cylinder than to the hexagonal cylinder, which can be corroborated by the Strouhal number extracted from the FFTs.

Khaledi and Andersson [2] obtained a value of $St = 0.1718$ for an hexagonal cylinder with corner orientation and a Strouhal of $St = 0.2136$ for an hexagonal cylinder with face orientation, which means that the vortex shedding frequency is higher in the face-oriented case. It is also inferred by them that the Strouhal number should decrease with increasing number of faces, approaching the Strouhal number of a circular cylinder in the limit. Regarding the circular cylinder, reference values can be found in experiments performed by Norberg [35] and Kiya et al. [36], where values close to $St = 0.21$ are obtained for uniform flow around a circular cylinder at $Re = 1000$.

The values of Strouhal number obtained in this study are presented in Table 5.3.

Table 5.3: Strouhal number obtained for the simulations performed with $Re = 10^3$

Grid	Turbulence Model	Circle	Hexagon		Octagon	
			Corner	Face	Corner	Face
1	$k-\omega SST$	0.2376	0.1908	0.1997	0.2613	0.2152
	$KSKL$	0.2365	0.1977	0.2087	0.2614	0.2153
2	$k-\omega SST$	0.2361	0.1931	0.2001	0.2369	0.2158
	$KSKL$	0.2345	0.2003	0.2092	0.2409	0.2155
3	$k-\omega SST$	0.2365	0.2010	0.1996	0.2342	0.2152
	$KSKL$	0.2345	0.2080	0.2236	0.2532	0.2145

A relative difference of around 12.7% from the reference values is found for the circular cylinder simulations, while for the hexagonal cylinder it is close to 10% for the corner orientation and about 5% for the face orientation.

It is possible to note that the tendency encountered by Xu et al. for flow at $Re = 2 \times 10^4$ shown in Figure 2.2 (c), also seems to apply to this case, since the values of Strouhal for the hexagonal cylinder with face orientation and for the octagonal cylinder with corner orientation are higher than their respective counterparts. Xu et al. also noted that for the Reynolds number they were experimenting with, the Strouhal of the octagonal cylinder with corner orientation would be slightly larger than the Strouhal of the circular cylinder, which also is true at the Reynolds number considered for this section of this work.

The similarity of the results here obtained with the literature available helps to confirm that the use of unstructured grids is not a disadvantage when dealing with complex geometries. The results also show that the grid refinement performed using Crepier's method [26] leads to grids as geometrically similar as possible. This shows that the use of this type of grids and this type of refinement can lead to accurate results when dealing with the more complex 3D geometry.

5.1.3 Instantaneous streamline patterns

Khaledi and Andersson studied the unsteady sheading behaviour of the flow by taking snapshots of the streamlines at particular points in time [2]. Similar snapshots taken at the end of the simulation (7 minutes = 420 seconds) in the current work are shown in Figure 5.3.

At this Reynolds, as is shown in Figure 5.3 (b), the flow separates near the leading edge of the flow parallel faces in the corner oriented hexagonal cylinder. In the case of the face oriented cylinder, the

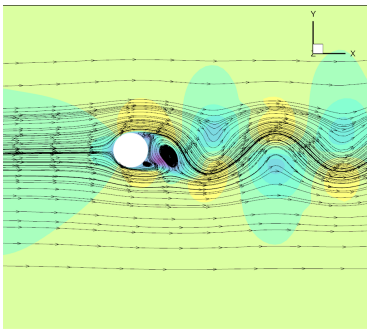

(a) Circular cylinder

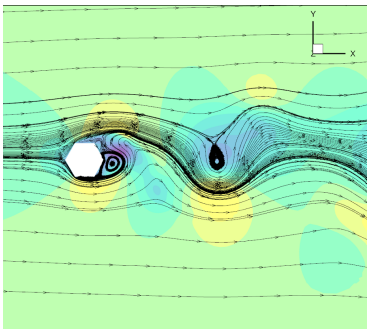

(b) Hexagonal cylinder with corner orientation

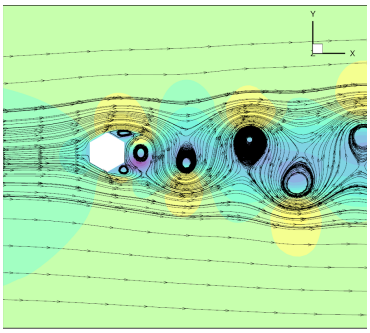

(c) Hexagonal cylinder with face orientation

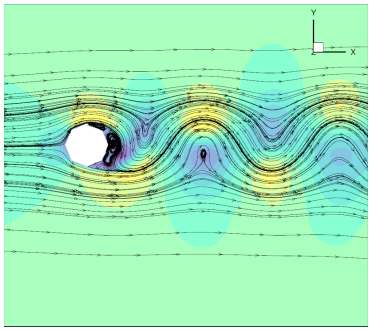

(d) Octagonal cylinder with corner orientation

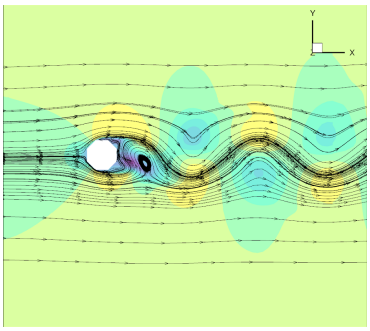

(e) Octagonal cylinder with face orientation

Figure 5.3: Streamline patterns obtained from the simulations with Grid 1 using the $k-\omega SST$ model at the time time instant of 420s.

flow separates at the upper and lower corners, where it forms a recirculation bubble, which evolves into a vortex that is shed alternatively from the upper and lower side of the cylinder. These results are similar to the ones obtained by Khaledi and Andersson [2].

As for the octagonal cylinder, since it is out of the scope of Khaledi and Andersson's research, no direct comparison can be made, however they state the following prediction: "While an octagonal cylinder resembles a square cylinder in the sense that face orientation implies that two of the faces become aligned with the flow direction, this is not the case for a hexagonal cylinder. In order for two of the faces of the hexagon to be parallel with the main stream, corner orientation is required" [2]. This means that the corner oriented hexagonal cylinder should share similarities in terms of flow characteristics with the face oriented octagonal cylinder while the face oriented hexagonal cylinder should be similar to the corner oriented cylinder. This does seem to be the case, since the corner oriented octagonal cylinder in Figure 5.3 shows that the flow is separating near the upper and lower corner of the cylinder and the face oriented octagonal cylinder in the same figure shows the flow separating at the leading edge of the faces parallel to the flow. Which, in turn corroborates the statement that "What matters for the wake dynamics is not if the front stagnation point is at a face or a corner, but if the width of the projected cylinder is determined by sharp corners or flow-parallel faces." [2].

5.1.4 Average Courant Number

As mentioned before, the average Courant number, C_{avg}, relates the smallest spatial scales to the time scales. High values of this parameter indicate the presence of significant time errors in the simulation, which could translate into unrealistic results. Acceptable values of C_{avg} are as close to one as possible, since it shows that the time scale and the spatial scale are well adapted to each other. Table 5.4 shows C_{avg} obtained for each simulation.

Table 5.4: Average Courant number C_{avg} obtained for the simulations performed with $Re = 10^3$

Grid	Turbulence Model	Circle	Hexagon		Octagon	
			Corner	Face	Corner	Face
1	$k-\omega SST$	1.28247	1.07209	1.55460	1.32202	1.16588
	$KSKL$	1.18062	1.06582	1.35405	1.41031	1.22798
2	$k-\omega SST$	1.25368	1.26615	1.50999	1.51988	1.18434
	$KSKL$	1.28533	1.21465	1.38345	1.47383	1.13029
3	$k-\omega SST$	1.36489	1.14386	1.44204	1.45579	1.28321
	$KSKL$	1.32384	1.13492	1.44945	1.46792	1.16369

As Table 5.4 shows, the average Courant of all the simulations performed at this stage is below 1.6. It also shows that the stability of the simulations is not affected by the grid refinement, since there is no discernible correlation between the average Courant number and the refinement level.

5.1.5 Convergence Properties

In order to further understand which kind of impact do the HEXPRESS™ grids and their refinement have on the results it is necessary to analyse the convergence of the simulations.

In an unsteady simulation, as is the case with this work, the software calculates the values of the properties of the flow, such as velocity, pressure and the turbulent viscosity in each time step. Before continuing to the next time step the residuals of those quantities must reach a maximum specified value, the so-called *Convergence Tolerance*, which for this study was set as 1×10^{-6}, i.e. the residuals of each quantity calculated with the specified equations must be lower than the value of Convergence Tolerance. Alternatively, if, by a set *Maximum Number of Iterations* in a given time step (200 for this study), these residuals have not all reached the Convergence Tolerance value, the simulation automatically moves on to the next time step. This is not ideal, since this means that at that time step the simulation did not converge to a good enough tolerance. High values of the number of iterations per time step also represent higher computational time, even if the maximum number of iterations has not been reached, so it is beneficial to keep the number of iterations per time step at an appropriate level.

The average number of iterations per time step for the simulations with the circular cylinder was close to 25 for Grids 2 and 3 and close to 30-35 for the simulations with Grid 1, regardless of the turbulence model. For the polygonal cases, with both orientations, Grids 2 and 3 performed at about 25 iterations per time-step and for Grid 1 it was close to 70 iterations per time-step. It is clear that for none of the

cases the value is close to the Maximum Iteration Value of 200, so all the simulations converge properly. For the two sparcest refinement levels, the average number of iterations are always around 25, which is enough to guarantee that the simulation will show the appropriate unsteady behaviour. For the finest grid there is a steep increase in average number of iterations per time step, particularly in the more complex geometries - hexagonal and octagonal cylinder - this was to be expected, given the decrease in grid size. Even so, the values registered for these simulations are still within acceptable levels. This shows that with more complex geometries and very small grid sizes, the simulation will be significantly more computationally expensive. This must be take into consideration when simulating the flow around the final 3D aquaculture structure.

5.1.6 Conclusions From This Study

Several conclusions can be extracted from this study that will help choose how to proceed with the rest of the work.

Firstly it is clear that the behaviour of circular, hexagonal and octagonal cylinders in turbulent flow has relevant differences. As the number of faces increases in a polygonal cylinder, similarities with the circular cylinder (infinite number of faces) start to become apparent, as was noted by Xu et al. [10], but there are still considerable differences between the octagonal cylinder and its circular counterpart. Those differences, both in Strouhal number, average forces and streamline patterns are even more accentuated in the case of the hexagonal cylinder. The orientation of the polygonal cylinders also has consequences regarding the behaviour of the flow around it and with the increase in turbulence, these effects might be accentuated. However, in a real offshore setting, choosing the orientation of a large floating aquaculture structure is close to impossible, which means not much can be done to minimize these effects.

Secondly, from a computational point of view, by comparing the Strouhal numbers obtained with the simulations performed with HEXPRESS^{TM} with the ones in the available literature it is possible to conclude that the results obtained with unstructured grids are accurate. Since the average Courant number is close to one for all the simulations and the number of iterations per time step never exceeds the maximum value and is always in an acceptable range, it is also possible to conclude that using unstructured grids provides stable simulations with an acceptable convergence. This gives confidence for the use of unstructured grids for the study of the flow around the 3D structure.

5.2 Preliminary Study 2

The objective of this study is to compare the results obtained from simulations where wall functions were used to the results of simulations without wall functions for three bluff body geometries to weigh the advantages and disadvantages of using wall functions in a flow around bluff bodies at a very high Reynolds number.

Unlike the previous study, the results will be presented by geometry, meaning that first the results

of the the simulations with a circular cylinder will be presented and analysed, followed by the octagonal cylinder's results and finally the ones from the hexadecagonal cylinder.

For the sake of brevity and simplicity, only the images regarding the results of the simulations performed with the circular cylinder will be presented here. The images of the results from the simulations with the polygonal cylinders can be consulted in Appendix B.

5.2.1 Circular Cylinder

Numerical Uncertainty

The contribution of the discretization error dominates the numerical uncertainty of the quantities of interest. This requires negligible contributions of round-off, statistical and iterative errors, which are achieved in part due to the use of double precision and an iterative convergence criteria of 10^{-6}. Table 5.5 presents the average number of iterations performed at each time-step for the simulations with this geometry. Even though there was no systematic attempt to perform optimization of the iterative convergence for each grid set, the under-relaxation parameters remain fixed with the exception of the two finest grid sets GNO and GWF1. For these, the explicit under-relaxation coefficients had to be slightly smaller than those used in the remaining grids. Compared to the calculation of τ_w from its definition (GNO), the use of wall functions reduces N_{it} and the increase of $((y_n^+)_2)_{max}$ of the near-wall cell also leads to a decrease in N_{it}. Thus the use of wall functions enhances the robustness of the flow solver, as expected. [4]

Table 5.5: Average number of iterations performed at each time step N_{it} for the grid sets GNO, GWF1, GWF2 and GWF3. Calculation of the flow around a circular cylinder at a Reynolds number of 10^8 with and without wall functions.

Grid	r_i					
Set	1.	1.16(6)	1.4	1.75	2.	2.3(3)
GNO	118	120	125	133	120	118
GWF1	63	61	64	70	85	80
GWF2	58	60	55	58	53	51
GWF3	50	43	30	35	31	31

Figures 5.4 to 5.7 illustrate the time histories of the drag coefficient C_D, lift coefficient C_L and Cartesian mean velocity components V_x and V_y at P_1 and P_2 for the last 4 cycles of the simulations performed for the circular cylinder. The mean value of each period [1] is subtracted to the dependent variables and the difference is divided by the maximum value obtained in each period. Time t is divided by the period of the cycles T obtained in each grid.

The results show that, for all simulations performed, all the quantities under analysis become periodic. Grid and time refinement, as well as the selected wall boundary condition is shown to affect differently the selected quantities.

C_D has a period that is half of that determined for C_L, which was expected. The signals of two velocity components of the point located outside the boundary layer (P_2) have the same period of C_L,

[1] The mean value of C_L is assumed zero.

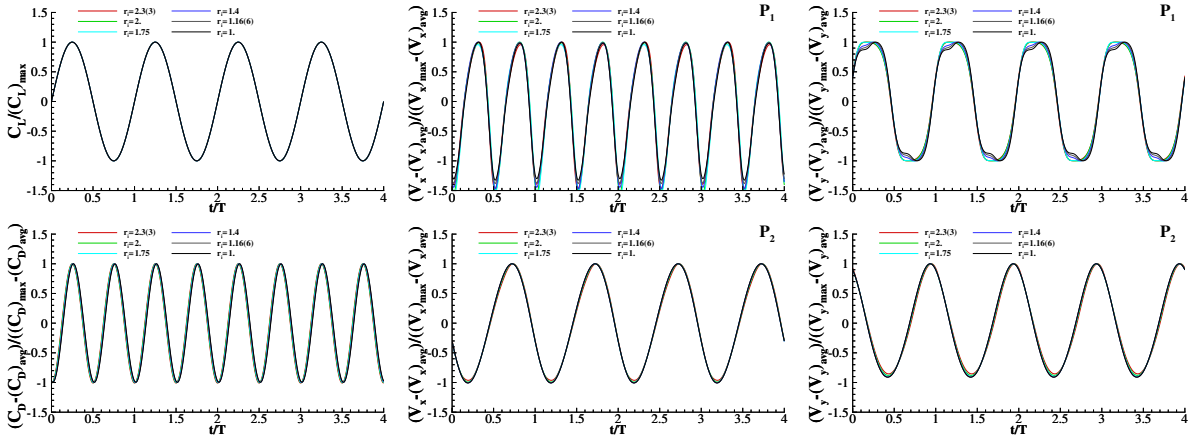

Figure 5.4: Time history of the drag coefficient C_D, lift coefficient C_L and Cartesian mean velocity components V_x and V_y at $x = 1.75D, y = 0$ (P_1) and $x = D, y = 0.75D$ (P_2) for the last 4 cycles of the simulations performed without wall functions, set GNO. Flow around a circular cylinder at a Reynolds number of 10^8.

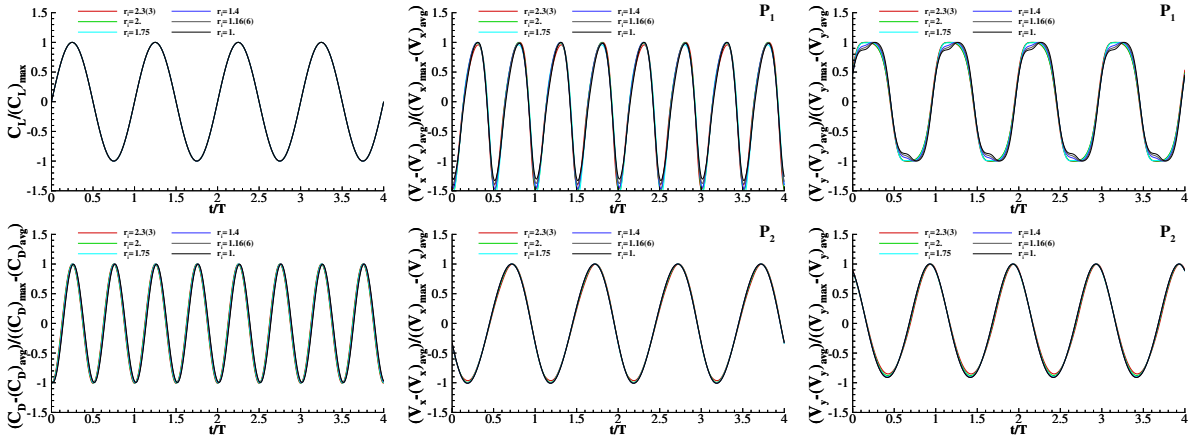

Figure 5.5: Time history of the drag coefficient C_D, lift coefficient C_L and Cartesian mean velocity components V_x and V_y at $x = 1.75D, y = 0$ (P_1) and $x = D, y = 0.75D$ (P_2) for the last 4 cycles of the simulations performed with wall functions, set GWF1. Flow around a circular cylinder at a Reynolds number of 10^8.

while, for the point in the near-wake (P_1) , V_y has the same period of C_L and V_x has half of that period, behaving as C_D.

The results of Figures 5.4 to 5.7 suggest that the solutions produced by the simulations show "RANS-like" behaviour. This is confirmed by the frequency content of the signals of the time histories of the quantities of interest, illustrated in Figures 5.8 to 5.11.

The FFTs of all simulations exhibit sharp peaks only at discrete frequencies, however force coefficients show only one frequency, while the plots of V_x and V_y at P_1 (near-wake) exhibit more than one. Regarding the point outside of the viscous region, P_2, the plots of V_x and V_y present the same frequency as C_L but the second harmonic is also present.

The statistical error depends on the initial condition and on the total simulation time (number of cycles included in the simulation). For this geometry, all simulations show a periodic behaviour, so statistical convergence can be assessed with ease. Table 5.6 presents the values of statistical uncertainty U_S

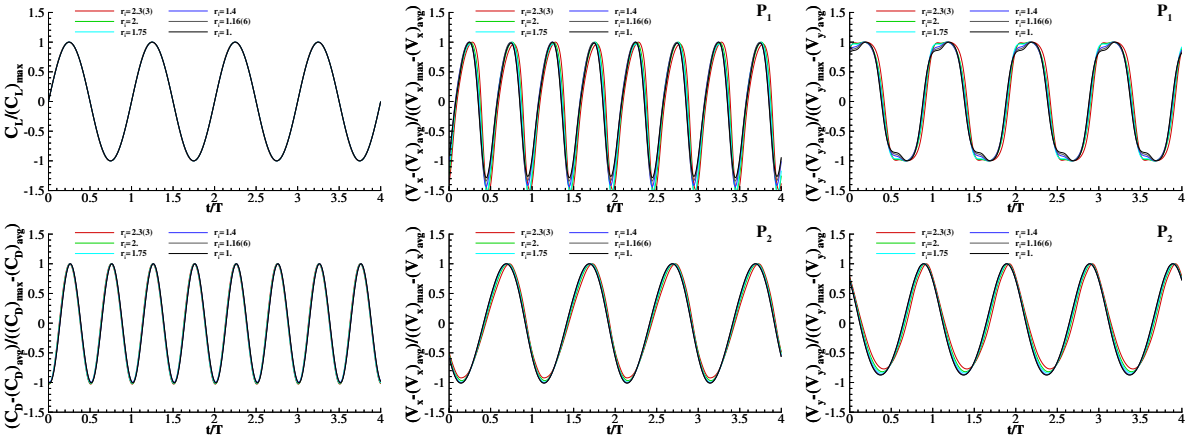

Figure 5.6: Time history of the drag coefficient C_D, lift coefficient C_L and Cartesian mean velocity components V_x and V_y at $x = 1.75D, y = 0$ (P_1) and $x = D, y = 0.75D$ (P_2) for the last 4 cycles of the simulations performed with wall functions, set GWF2. Flow around a circular cylinder at a Reynolds number of 10^8.

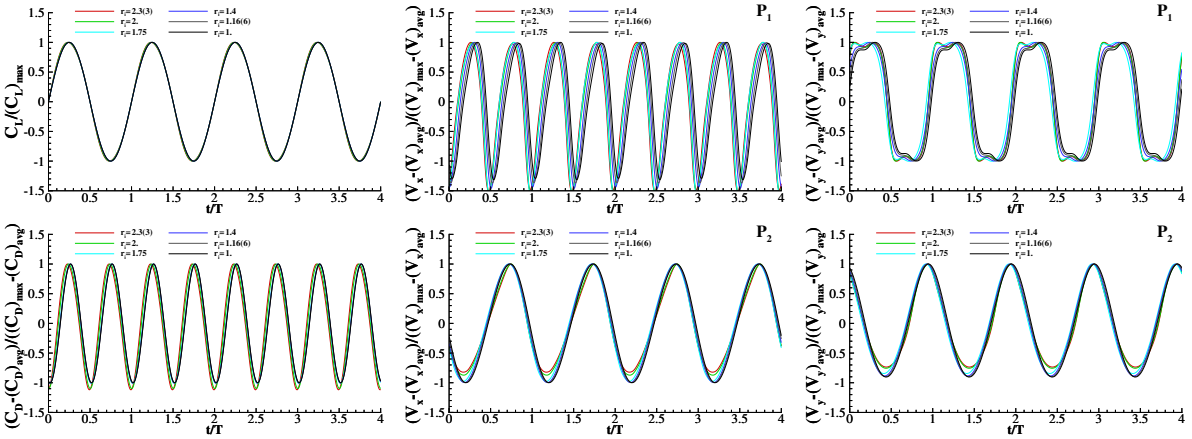

Figure 5.7: Time history of the drag coefficient C_D, lift coefficient C_L and Cartesian mean velocity components V_x and V_y at $x = 1.75D, y = 0$ (P_1) and $x = D, y = 0.75D$ (P_2) for the last 4 cycles of the simulations performed with wall functions, set GWF3. Flow around a circular cylinder at a Reynolds number of 10^8.

of $C_{D_{avg}}$ and TV_∞/D obtained from the last 48 cycles divided in the 12 intervals of 4 cycles. From this it is possible to conclude that the contribution of the statistical error to the numerical uncertainty is negligible when compared with iterative errors that are at least one order of magnitude above the iterative convergence criteria, 10^{-6}.

Simulations with iterative convergence criteria of 10^{-3}, 10^{-4} and 10^{-5} were also performed, however these were not repeated for all grids and time steps tested. Iterative errors were assessed only for the most refined grid and smallest time-step ($r_i = 1$) of set GNO. The estimated iterative errors obtained were sufficiently small to assume that numerical uncertainty is dominated by the discretization error.

The convergence of $C_{D_{avg}}$, $C_{D_{max}}$, $C_{L_{rms}}$ and St with grid/time refinement is illustrated in figure 5.12.

There is a remarkable consistency between the results obtained without wall functions (GNO) and those obtained with wall functions for the minimum and maximum values of near-wall cell size (GWF1 and GWF3), however the same is not true for the data obtained with the set GWF2. There is a significant

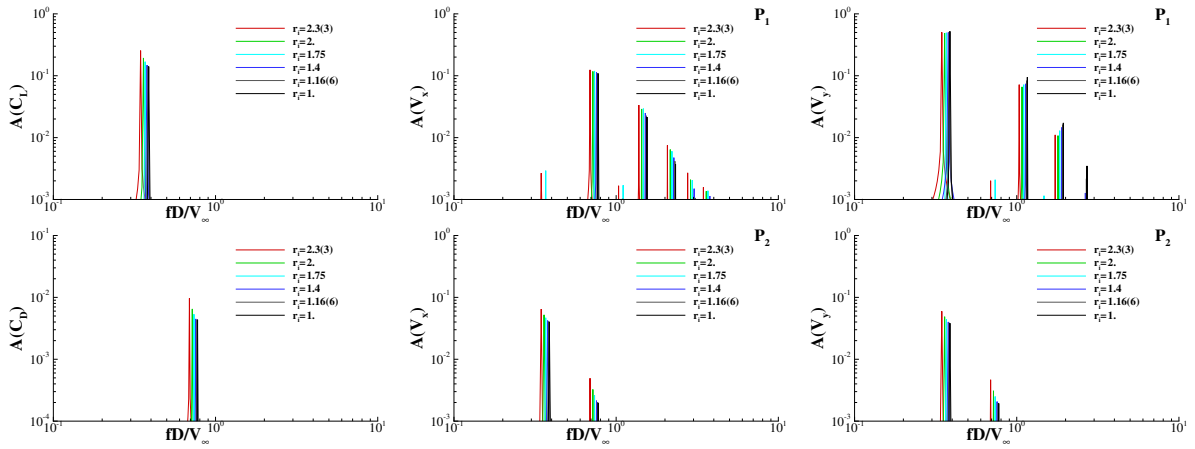

Figure 5.8: Frequency content of the time history of the drag coefficient C_D, lift coefficient C_L and Cartesian mean velocity components V_x and V_y at $x = 1.75D, y = 0$ (P_1) and $x = D, y = 0.75D$ (P_2) for the last 48 cycles of the simulations performed without wall functions, set GNO. Flow around a circular cylinder at a Reynolds number of 10^8.

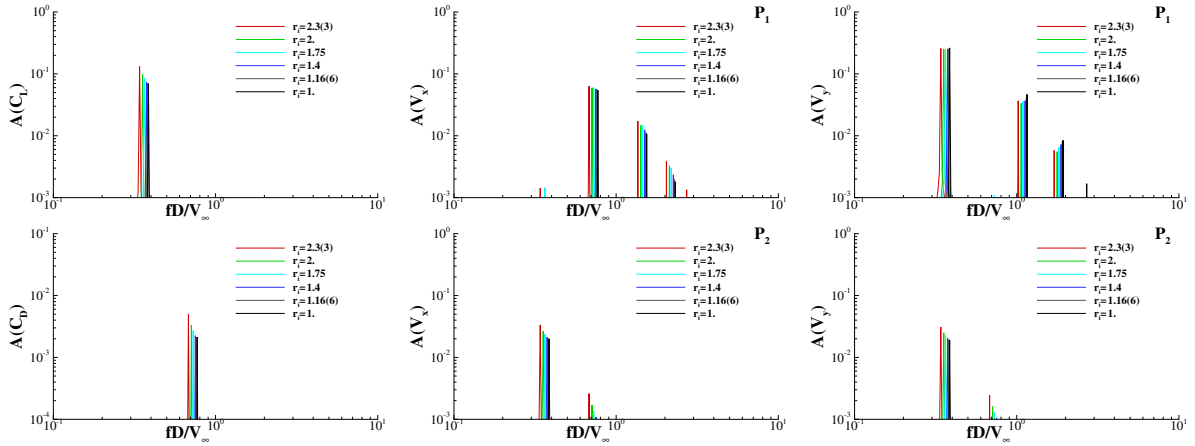

Figure 5.9: Frequency content of the time history of the drag coefficient C_D, lift coefficient C_L and Cartesian mean velocity components V_x and V_y at $x = 1.75D, y = 0$ (P_1) and $x = D, y = 0.75D$ (P_2) for the last 48 cycles of the simulations performed with wall functions, set GWF1. Flow around a circular cylinder at a Reynolds number of 10^8.

discrepancy between the data obtained with this grid set and the remaining simulations that cannot be explained by numerical uncertainty. This is an awkward result, given that it suggest that wall functions could be acceptable for bluff bodies at very high Reynolds numbers, but it also shows that there is a strong influence of the size of the near wall cell on the force coefficients determined with wall functions [4].

The convergence properties observed for C_L, C_D and St are not identical for the four conditions tested. For the level of grid/time refinement shown, the convergence of $C_{D_{avg}}$ and $C_{D_{max}}$ is not monotonic for the GNO set, while all other fits are performed with orders of grid/time convergence between 1.8 and 2. The error constant is significantly larger for the results of the GWF3 set compared with the results of the other three sets. For this set, GWF3, the two coarsest grids had to be discarded for the fits, whereas only the coarsest grid was ignored for all remaining fits.

Figure 5.13 shows the grid/time refinement of the mean velocity components at P_1 and P_2. Even

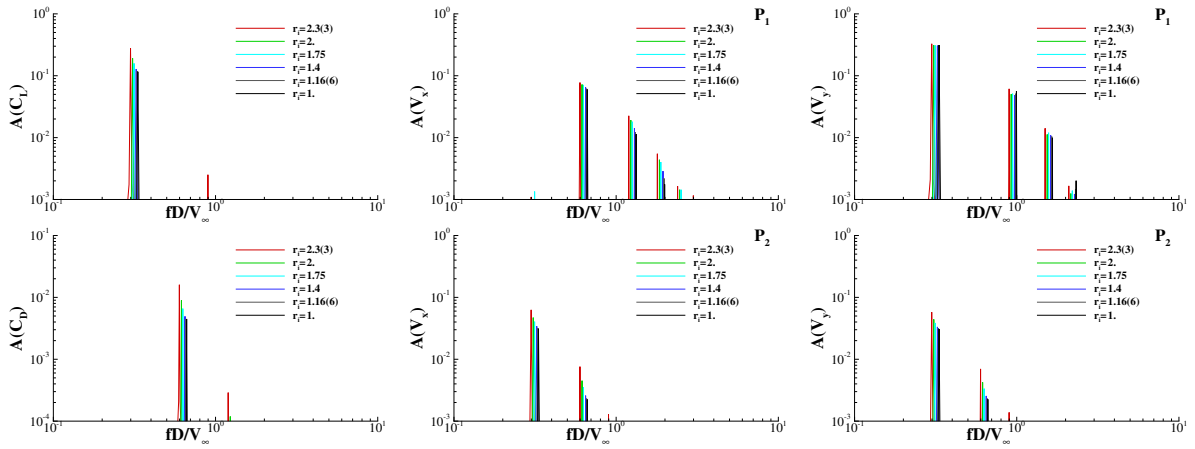

Figure 5.10: Frequency content of the time history of the drag coefficient C_D, lift coefficient C_L and Cartesian mean velocity components V_x and V_y at $x = 1.75D, y = 0$ (P_1) and $x = D, y = 0.75D$ (P_2) for the last 48 cycles of the simulations performed with wall functions, set GWF2. Flow around a circular cylinder at a Reynolds number of 10^8.

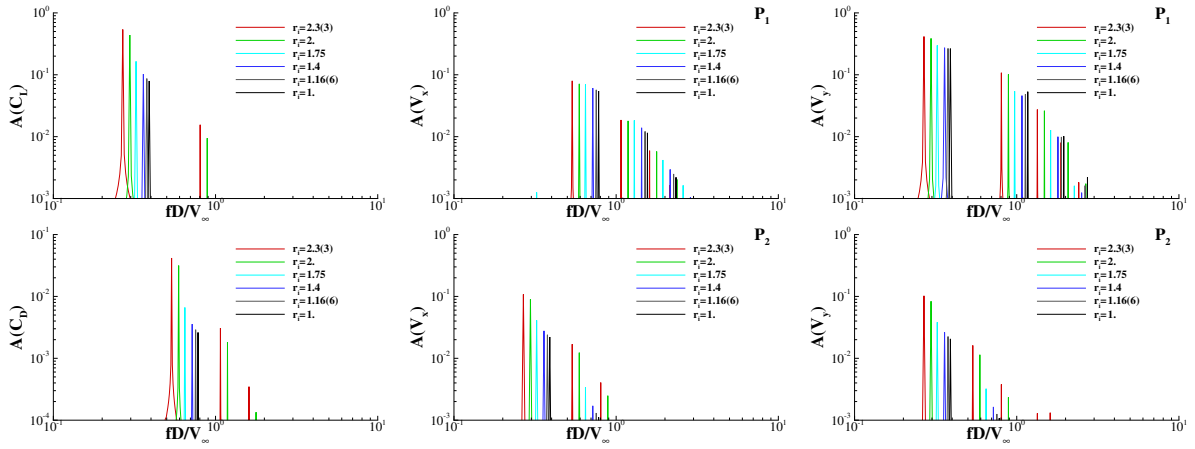

Figure 5.11: Frequency content of the time history of the drag coefficient C_D, lift coefficient C_L and Cartesian mean velocity components V_x and V_y at $x = 1.75D, y = 0$ (P_1) and $x = D, y = 0.75D$ (P_2) for the last 48 cycles of the simulations performed with wall functions, set GWF3. Flow around a circular cylinder at a Reynolds number of 10^8.

though there are significantly more non-monotonic cases than for the force coefficients, the main trends observed here are similar to those found in the data obtained from the force coefficients. Furthermore, these results indicate that the wake obtained in grid set GWF2 is wider than the one determined for the other grid sets.

Comparison of Solutions Obtained With and Without Wall Functions

The results obtained for this geometry seem to indicate that at very high Reynolds numbers, wall functions significantly enhance the robustness of the simulations compared to the calculation of τ_w from the definition. Figure 5.14 shows the average and maximum drag coefficient, root mean squared lift coefficient and Strouhal number obtained for the grids with $r_i = 1$, with the respective error bars due to numerical uncertainty.

The results show that only the GNO, GWF1 and GWF3 are consistent for all four quantities of interest

Table 5.6: Statistical uncertainty U_s of the average drag coefficient $(C_D)_{avg}$ and cycles period TV_∞/D obtained from the variance of the last 48 cycles divided in 12 intervals of 4 cycles. Flow around a circular cylinder at a Reynolds number of 10^8.

	$U_s\left[(C_D)_{avg}\right] \times 10^7$				$U_s\left[TV_\infty/D\right] \times 10^7$			
r_i	GNO	GWF1	GWF2	GWF3	GNO	GWF1	GWF2	GWF3
2.3(3)	1.3	0.1	1.2	17.8	9.9	2.7	3.0	59.7
2.	0.3	0.3	0.2	1.3	2.6	3.3	2.3	7.9
1.75	0,5	0.5	4.5	2.2	6.5	4.1	39.6	8.8
1.4	0.8	1.9	4.9	0.04	11.7	7.6	40.3	2.5
1.16(6)	0,9	0,2	0.5	0.04	13.7	1.8	5.0	1.6
1.	0.8	0.8	1.3	0.04	7.4	8.0	9,8	1.6

(there is overlap of the error bars of the four grid sets). The results from the GWF2 grid set present discrepancies relative to the remaining simulations not explained by the numerical uncertainty. This means that the results do not change monotonically with the increase in near-wall cell height. But the grids with the largest near-wall cell size show the largest numerical uncertainties.

Figure 5.15 illustrates the streamlines and V_x field at a time instant close to minumum lift coefficient for the finest grids/smallest time-step of the four grid sets tested. There is a remarkable resemblance between the GNO, GWF1 and GWF3 graphics. The GWF2 graphic shows a larger vortex and wider near-wake, which explain the results obtained for this grid set for the force coefficients and Strouhal number.

In figure 5.16 the regions of the flow with $\nu_t < 5\nu$ are left white to visualize only the "viscous region". GWF2 shows once again a wider wake than the other grid sets. The field of ν_t is also different than those obtained in the simulations performed with the remaining grid sets. Although it cannot be considered surprising to obtain an influence of the near-wall cell size on the flow field obtained with wall functions, it was not expected to obtain a good match between the lowest (GWF1) and highest (GWF3) cell sizes.

5.2.2 Octagonal Cylinder

Numerical Uncertainty

For this geometry, for the simulations performed without wall functions, iterative convergence was extremely difficult to achieve. The ratio between the maximum and average Courant number is significantly larger than what was obtained for the circular cylinder. Two alternatives are available to achieve iterative convergence for the present grids: reduce the time-step until iterative convergence is acceptable; increase under-relaxation (implicit and/or explicit) at each time step. For the simulations performed with the coarsest grids ($r_i = 2.3(3)$), the first option required time steps more than 100 times smaller that those presented in Table 4.3 for the circular cylinder, which makes the simulations unaffordable. Alternatively, to keep a time-step corresponding to half of what is presented in Table 4.3 more than 2500 iterations are necessary at each time step to achieve L_∞ norms of the normalized residuals below 5×10^{-4}. Reducing that value to 10^{-6} would mean that 10^4 iterations per time step were necessary and so no attempt was made to simulate the flow in the remaining grids.

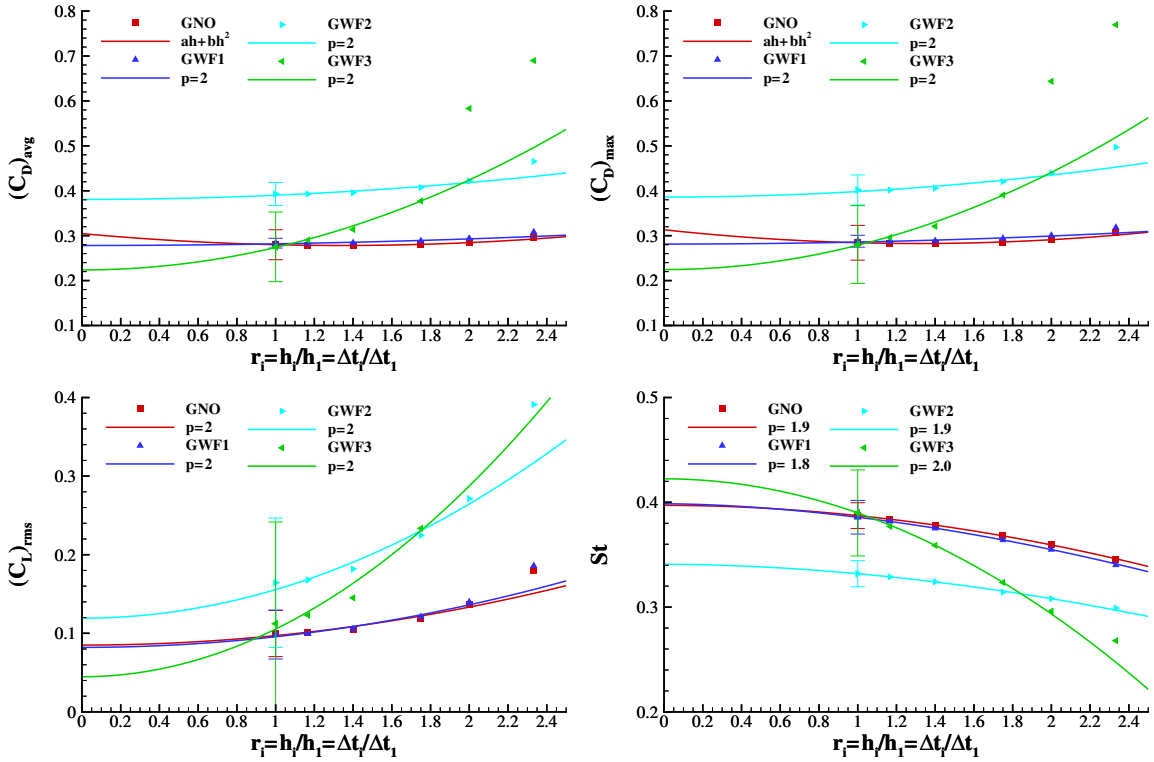

Figure 5.12: Convergence with grid/time refinement of average $(C_D)_{avg}$ and maximum $(C_D)_{max}$ drag coefficient, root mean squared $(C_L)_{rms}$ lift coefficient and Strouhal number St. Flow around a circular cylinder at a Reynolds number of 10^8 calculated with and without wall functions.

For the set GWF1, which presents wall functions with near-wall cell heights of $y^+ \simeq 300$ the problems of robustness remained, thus simulations were only performed with the coarsest grid. Figure B.1 shows the time histories of the lift and drag coefficients and their respective frequency content for the results obtained with the coarsest grid of sets GNO and GWF1. These results show a "RANS-like" behaviour. The statistical convergence appears to be better for the grid set with wall functions (GWF1) compared to the one without wall functions (GNO). On the other hand, grid/time refinement leads to an increase of the iterative convergence problems at each time step for the GWF1 set, so only the other two wall function sets (GWF2 and GWF3) will be further analysed.

Figure B.2 illustrates the time histories of the lift and drag coefficients obtained in the GWF2 set [2]. The coarsest grids are the only ones that exhibit a periodic behaviour with discrete frequencies in the force coefficient time histories. Grid/time refinement lead to an increase in the range of frequencies present in the time histories under study. This suggests that the turbulence model (as well as numerical diffusion) are not enough to obtain a RANS solution. This makes it difficult to assess statistical convergence or even to define a cycle.

The force coefficient time histories obtained in the grids of the last wall function set (GWF3) are shown in Figure B.3. This set shows similar trends to the ones obtained in the GWF2 set. However, in this set, not even the coarsest grid shows a periodic behaviour or a solution that resembles a RANS solution.

[2]The simulation of the finest grid of this set was not performed.

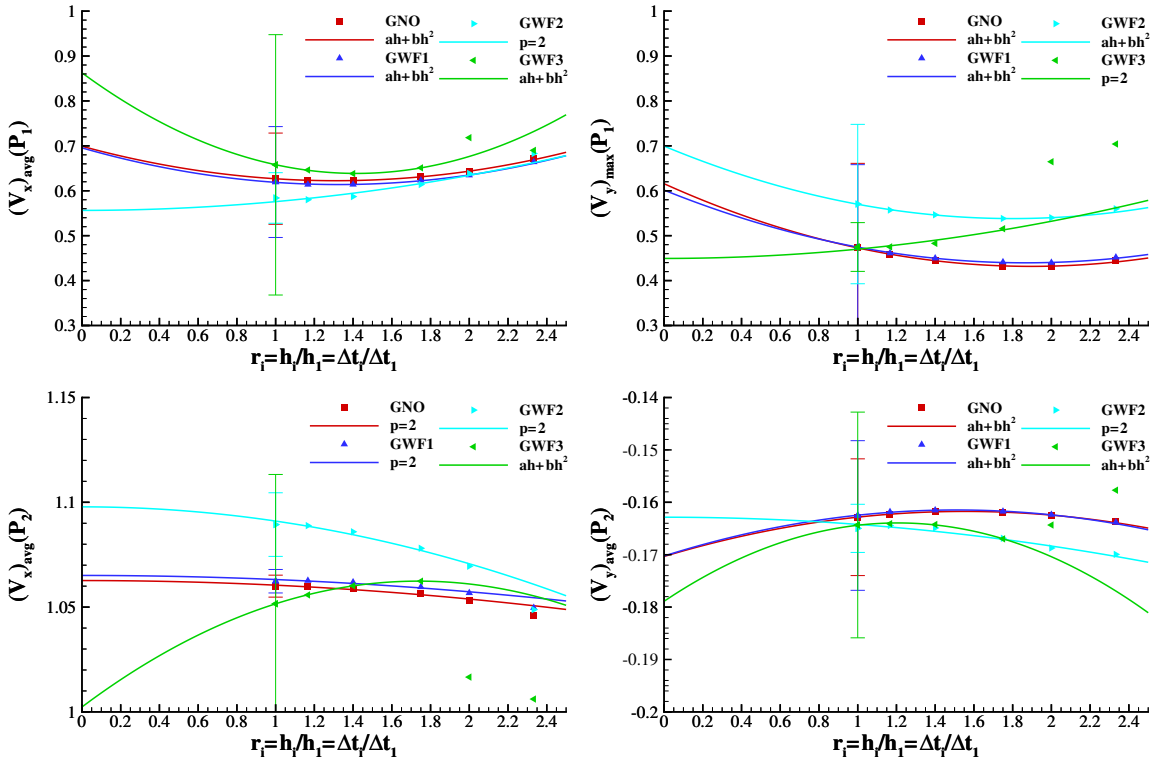

Figure 5.13: Convergence with grid/time refinement of average $(V_x)_{avg}$ and maximum $(V_y)_{max}$ mean velocity components at $x = 1.75D, y = 0$ (P_1) and average $(V_x)_{avg}$ and maximum $(V_y)_{avg}$ at $x = D, y = 0.75D$ (P_2). Flow around a circular cylinder at a Reynolds number of 10^8 calculated with and without wall functions.

Taking into consideration the properties of the time signals obtained for the force coefficients, statistical convergence data will not be presented for the local quantities that show time histories that do not resemble ”RANS-like” solutions.

Figure B.4 illustrates the convergence with grid/time refinement of the average and maximum drag coefficient, $C_{D_{avg}}$ and $C_{D_{max}}$, the root mean squared lift coefficient, $C_{L_{rms}}$ and the Strouhal number St, the latter obtained from the frequency presenting the highest magnitude in the time history of the lift coefficient. Even though the estimated error bars are unavoidably large, there is a remarkable consistency between the results obtained from the two grid sets.

Flow Properties

The values obtained for the force coefficients with this geometry are significantly larger than the ones obtained for the flow around the circular cylinder. More, the Strouhal number is close to half of that obtained for the circular cylinder, which seems to indicate that the wake is wider for the octagonal geometry.

Figure B.5 shows the streamlines of mean velocity component V_x and eddy viscosity ν_t/ν for a time instant for the finest grid used in each set (the time instants are not the same for the two grid sets). The figure shows that the wake is indeed larger than the one from the circular cylinder. It is also evident that the increase in size of the ”viscous region” is due to the kinks on the surface of the cylinder that

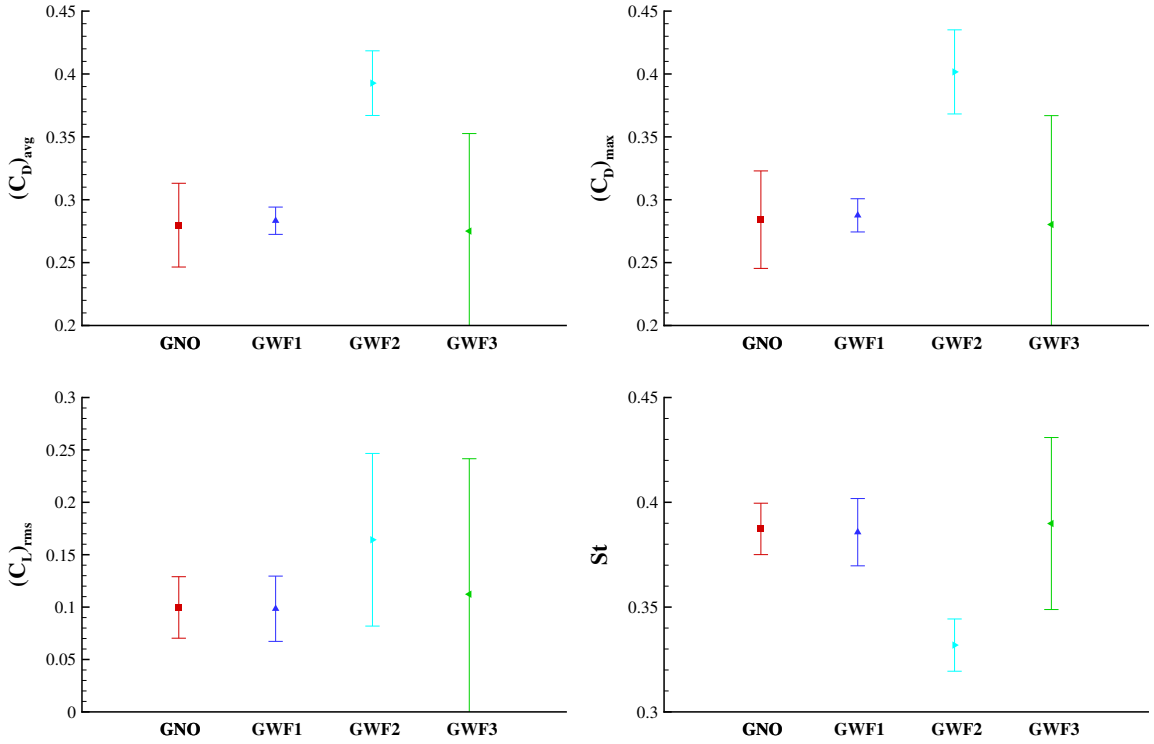

Figure 5.14: Average $(C_D)_{avg}$ and maximum $(C_D)_{max}$ drag coefficient, root mean squared $(C_L)_{rms}$ lift coefficient and Strouhal number St obtained in the finest grids with the smallest time step. Flow around a circular cylinder at a Reynolds number of 10^8 calculated with and without wall functions.

provoke flow separation. Although the time histories suggest that this solution does not correspond to the "RANS-like" solution that was expected, the width of the wake is similar in the two simulations, unlike what was obtained with the circular cylinder for these two grid sets.

5.2.3 Hexadecagonal Cylinder

Numerical Uncertainty

With this geometry, the objective is to assess the robustness of the flow solver and to compare the flow properties with the ones from the other geometries in order to determine whether the geometry with 16 sides more closely resembles the octagonal or circular cylinder.

The Courant number was maintained close to 0.3 for all grid sets to achieve iterative convergence in a reasonable number of iterations per time-step. Regardless, simulations with the coarsest grid of the GWF1 set required approximately 2000 iterations to reduce the L_∞ norm of the normalized residuals to 10^{-4}, so the simulations for this set were not completed. For the coarsest grid of the GNO set, about 500 iterations were required to lower the residuals to 5×10^{-5}. Hence, as was done for the octagonal case, Figure B.6 presents only the time histories of the force coefficients and their respective frequency content obtained with the coarsest grid.

The results suggest that more simulation time is required to achieve statistical convergence, Nevertheless, the results obtained for the force coefficients are much closer to the octagonal cylinder than the

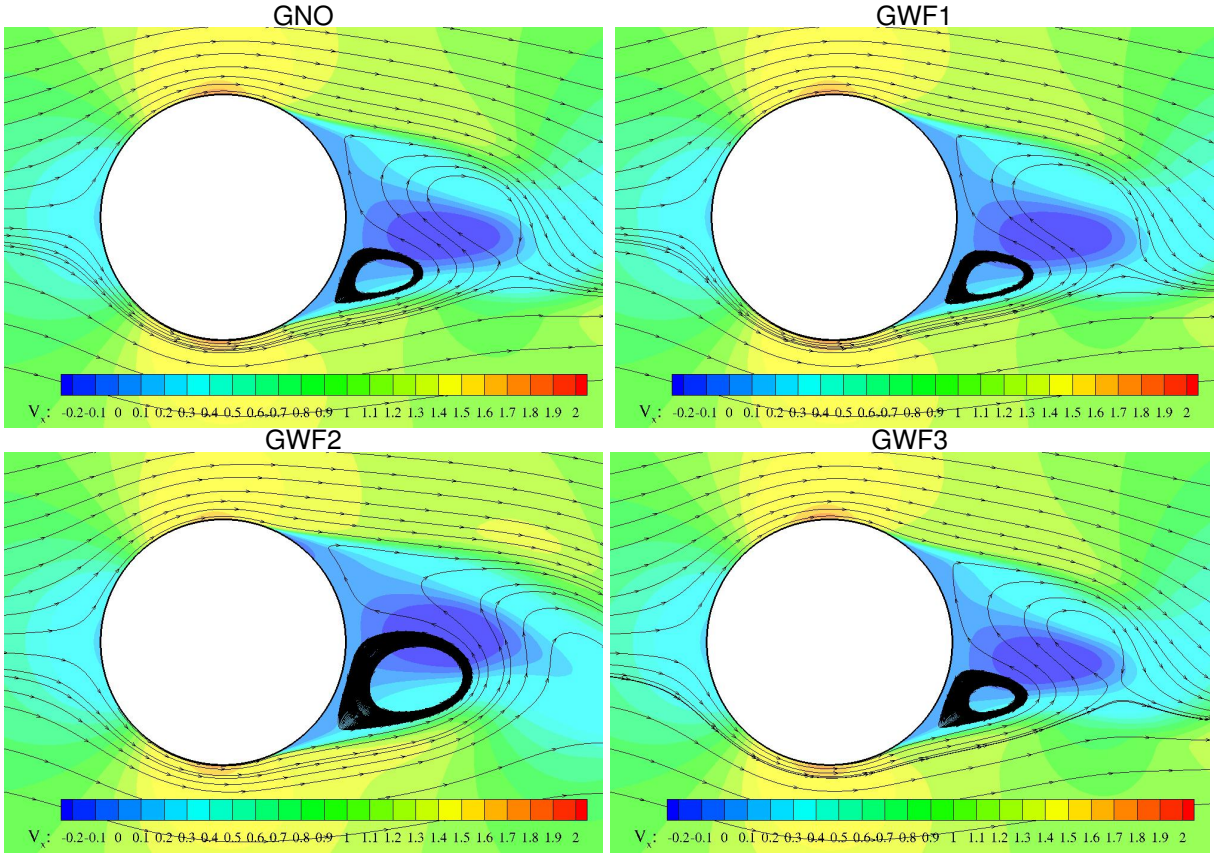

Figure 5.15: Visualization of the flow field and isolines of V_x at a time close to minimum lift coefficient $(C_L)_{min}$ obtained in the finest grids with the smallest time step. Flow around a circular cylinder at a Reynolds number of 10^8 calculated with and without wall functions.

circular one.

Grid sets GWF2 and GWF3 show significantly better iterative convergence, with an average of 30 iterations per time-step with a convergence criteria of 10^{-5}. Figures B.7 and B.8 show the time histories of the force coefficients in the six grids of the GWF2 and GWF3 sets, respectively. All the solutions present a "RANS-like" behaviour, but the frequency content of the force coefficients differs between the two sets.

In GWF2 the two coarsest grids show a periodic behaviour of C_L and C_D, with the lift coefficient presenting only one frequency. However, with grid/time refinement this behaviour is lost and for the finest grid several other frequencies appear in the time history of the force coefficients.

The results of GWF3 present a consistent behaviour of the time signals of the lift and drag coefficients for all the grids/time-steps tested. Statistical convergence resembles that which was obtained in the circular cylinder, thus in this case numerical uncertainty is dominated by the discretization error.

Figure B.9 illustrates the convergence with grid/time refinement of $C_{D_{avg}}$, $C_{D_{max}}$, $C_{L_{rms}}$ and St for the simulations performed using GWF2 and GWF3. The most striking feature observed is that none of the quantities of interest present monotonic convergence. The largest uncertainties are, once again, obtained for the GWF3 set. However, in this case the results of the GWF2 set must be carefully interpreted because grid/time refinement leads to a change in the frequency content of the time histories.

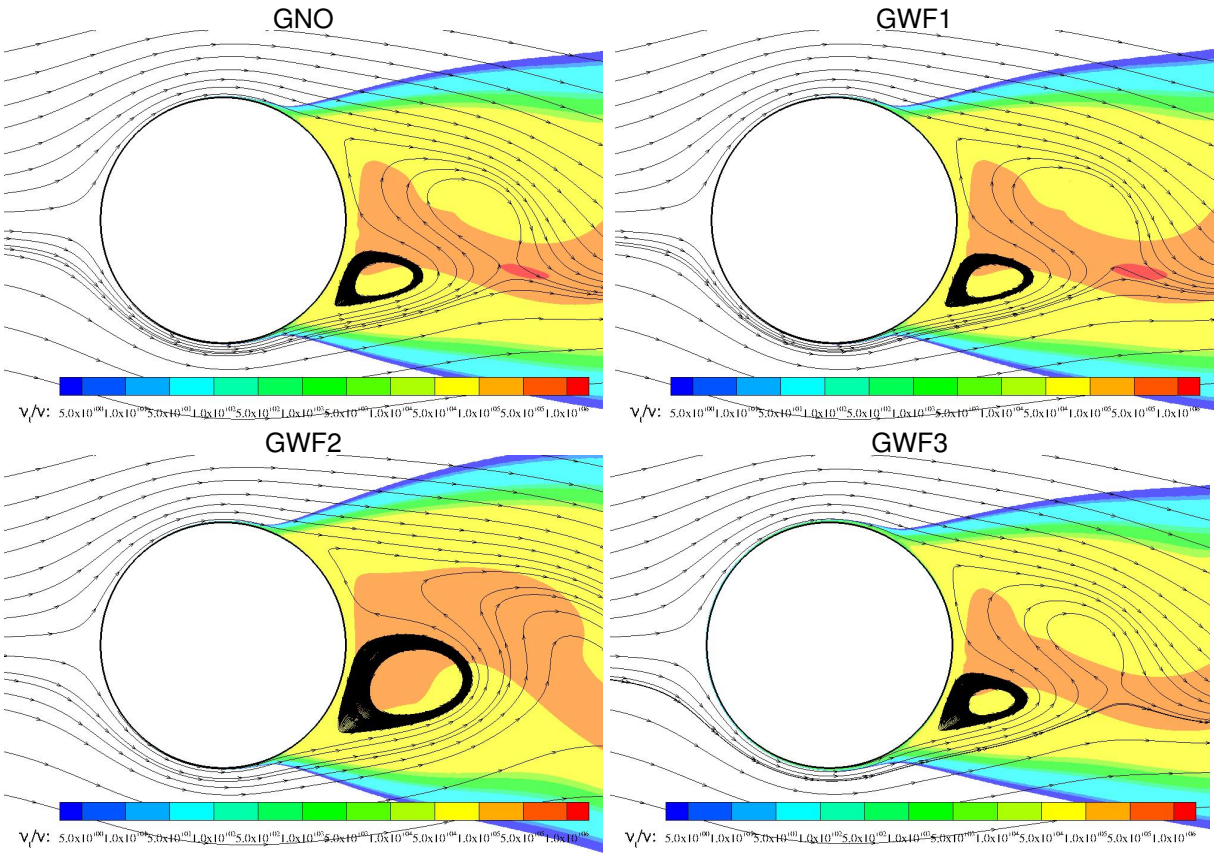

Figure 5.16: Visualization of the flow field and isolines of ν_t/ν at a time close to minimum lift coefficient $(C_L)_{min}$ obtained in the finest grids with the smallest time step. Flow around a circular cylinder at a Reynolds number of 10^8 calculated with and without wall functions.

Flow Properties

The force coefficients obtained for this cylinder are closer to the ones from the octagonal cylinder than those from the circular cylinder. However, there is a reduction of the average drag coefficient which suggests a reduction, however small, of the width of the wake in comparison to the octagonal cylinder.

Figure B.10 shows the isolines of mean velocity V_x and eddy viscosity ν_t/ν at a time instant close to minimum lift coefficient. The expected reduction in wake width compared to the octagonal cylinder is visible, but is still significantly wider than the circular cylinder.

5.2.4 Conclusions From This Study

From this study it is possible to conclude that:

- the use of wall functions significantly improves the robustness of the flow solver, since for the polygonal cylinders the time steps required to obtain statistical convergence without the use of wall functions is unacceptably small. Additionally, the under-relaxation required to converge at each time-step with maximum Courant numbers close to 2 lead to thousands of iterations to lower the residuals to acceptable levels of convergence criteria;

- there is no clear trend in the results obtained with wall functions using different sizes of the near-

wall cell size. The results of the largest and smallest values of near-wall cell size for the circular cylinder case with wall functions were consistent, whereas the intermediate size showed a larger wake width; For the polygonal cylinders, only the two largest sizes of near-wall cell resulted in good iterative convergence and the consistency of those two grid sets is better than for the circular cylinder; the only noticeable systematic trend in the three test cases seems to be that there is a significantly increase in numerical uncertainty of the quantities under investigation for the largest near-wall cell size;

- The results from the simulations of flow around the octagonal cylinder did not present a "RANS-like" behaviour, while only discrete frequencies in the time histories were present in the flow around the circular cylinder for all grid/time steps tested. For the hexadecagonal cylinder "RANS-like" solutions were obtained but the frequency content is strongly dependent on the refinement level for one of the grid sets. Thus it is impossible to know whether or not the turbulence model is capable of providing the necessary diffusion to damp the turbulent fluctuations.

- The results show that, in spite of the difficulties to guarantee iterative convergence, even at such high Reynolds numbers it is the kinks on the surface of the polygonal cylinders that produce a significant increase of the force coefficients when compared to the circular cylinder.

This seems to suggest that wall functions can be an efficient option to simulate very high Reynolds numbers flows around bluff bodies, but also that the size of the near-wall cells have a strong influence on the solution. [4].

5.3 3D Study

For the 3D case it is still relevant to understand the average values of forces at which the structure will be subject to, as well as the frequency content of the simulation, since this is important information for a future structural analysis. For the same reason a study of the average moments is also relevant. The point on which the moments are being calculated is on the surface of the water in the center of the octagon, $(x, y, z) = (5452, 6951.3, 6815)[m]$.

5.3.1 Time History of the Forces and Moments

As was done in the previous cases, using ReFRESCO's Force monitor, the evolution of the forces acting on the structure throughout the duration of the simulation was plotted. Additionally, by means of the Moments monitor, a similar analysis was made for the moments acting on the structure.

In the previous studies, the initial part of the simulation, under the effect of the initial condition was discarded and the most relevant part of the information was extracted to be analysed, since it was possible to see in the results obtained, the diffusion of said effect and the onset of periodicity in the solution, which in turn allows to make an assessment about the iterative convergence of the simulation. However, in the simulations performed in this part of the investigation, the results obtained do not show a

periodic behaviour of the simulations, as can be seen in Figures 5.17 and 5.18, which means that, while average values can be extracted and a frequency analysis performed, it is hard to judge the statistical convergence of the simulations.

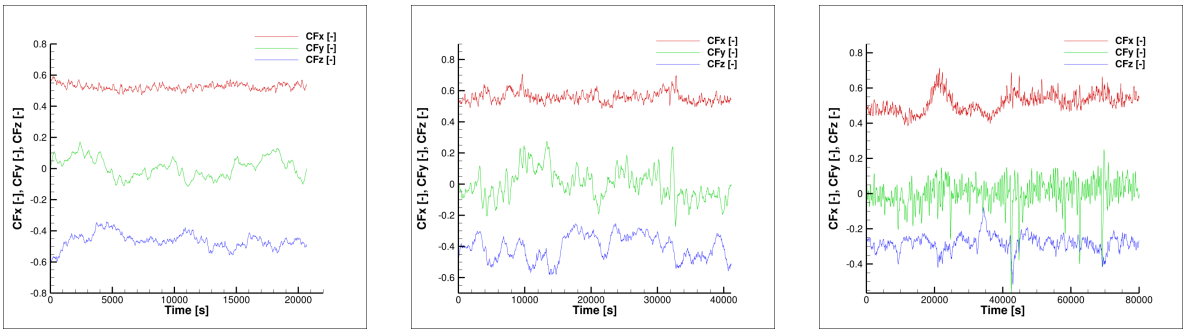

(a) Grid 1 (b) Grid 2 (c) Grid 3

Figure 5.17: Evolution of the force coefficients, C_{F_x}, C_{F_y} and C_{F_z} for each of the three grids

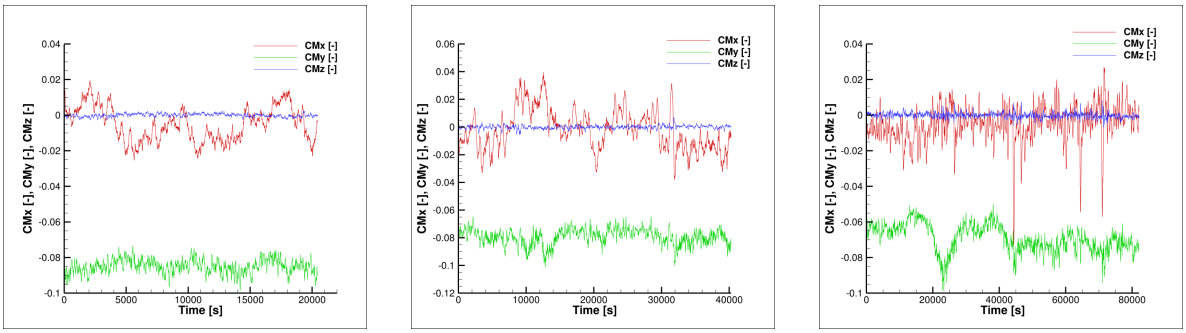

(a) Grid 1 (b) Grid 2 (c) Grid 3

Figure 5.18: Evolution of the moments coefficients, C_{M_x}, C_{M_y} and C_{M_z} for each of the three grids

Figures 5.17 and 5.18 show an aperiodic behaviour of both the forces and moments acting on the structure, which is not a "RANS-like" behaviour similar to what was obtained in the second preliminary study. To better understand this behaviour, a frequency analysis was performed.

5.3.2 Frequency Analysis

Given the behaviour of the forces and moments shown in Figures 5.17 and 5.18, a frequency analysis is helpful to understand this behaviour and possibly show the reasons behind it. The signals of the forces and the moments in the three directions were subject to a Fast Fourier Transform, Figure 5.19 shows the plots of the FFTs.

Figure 5.19 shows that it is not possible to identify one dominant frequency. This means that it is not possible to extract a Strouhal number. This type of frequency behaviour seems to be closer to what was to be expected from a fully turbulent regime as opposed to a RANS simulation. It is even possible to find a frequency region where the log-log plot seems to have a linear slope, which would be consistent with Kolmogorov's $-5/3$ rule [37, 38]. The slope of the forces FFT plots here presented is approximately -1.9 for Grid 1, -1.5 for Grid 2 and -2.0 for Grid 3. The slope of the moments FFT plots is approximately

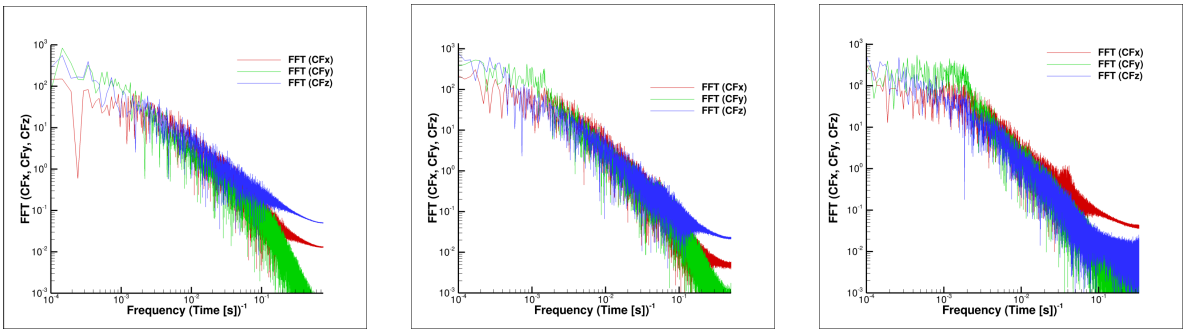

(a) Grid 1: Forces FFT (b) Grid 2: Forces FFT (c) Grid 3: Forces FFT

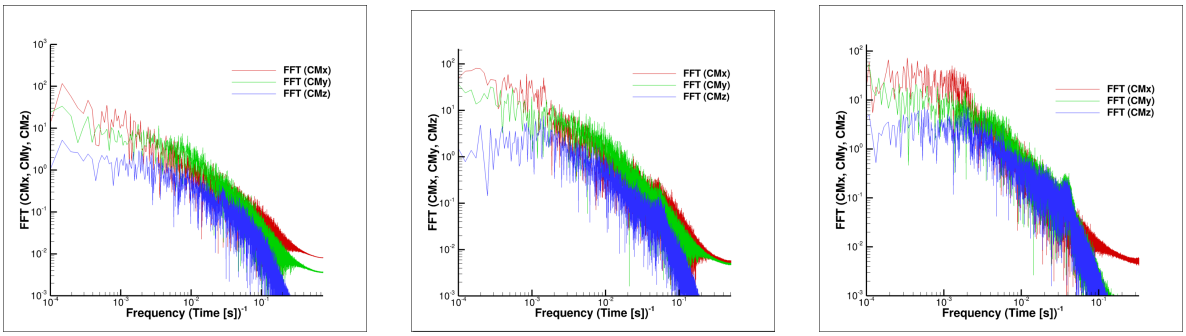

(d) Grid 1: Moments FFT (e) Grid 2: Moments FFT (f) Grid 3: Moments FFT

Figure 5.19: Fast Fourrier Transform of the signal of the Forces for the finest Grid (Grid 1).

-1.2 for Grid 1, -1.3 for Grid 2 and -1.9 for Grid 3.

This behaviour suggests that the diffusion offered by the turbulence model was not able to dampen some of the turbulent frequencies at such a high Reynolds number, as was the case of the octagonal cylinder analysed in the second preliminary study.

Nonetheless some information can still be taken from these results, namely regarding the average values of the forces and moments.

5.3.3 Average Forces and Moments

From the plots of Figures 5.17 and 5.18, the average values of the forces and moments were calculated for each case, as can be seen in Tables 5.7 and 5.8, respectively.

Table 5.7: Average value of forces and force coefficients for the simulations performed with a 3D Aquaculture Structure, $Re = 10^8$

	$\overline{C_{F_x}}$	$\overline{C_{F_y}}$	$\overline{C_{F_z}}$	$\overline{F_x}\ [N]$	$\overline{F_y}\ [N]$	$\overline{F_z}\ [N]$
Grid 1	0.52338537	-0.03985061	-0.46235996	2279.998	-173.5992	-2014.156
Grid 2	0.55837157	-0.00753203	-0.37579110	2432.406	-32.81141	-1637.040
Grid 3	0.51759876	-0.04186968	-0.27691708	2254.789	-182.3948	-1206.320

It is evident that the force in the y-direction (F_y) is several orders of magnitude smaller than the forces in the streamwise direction of the flow F_x and, more notably, than the force in the vertical direction F_z.

The reason for the latter is most likely related to the tapered geometry of the net, which creates a zone of high flow velocity and therefore low pressure in the bottom of the net, due to the formation of large vortexes in the bottom of the structure, pushing the structure downwards. It is reasonable to assume that similar simulations where the net is computed as a permeable, deformable surface will result in a lower absolute values of F_z and F_x, since the net will no longer display the same behaviour as it does in this study.

Table 5.8: Average value of moments and moment coefficients for the simulations performed with a 3D Aquaculture Structure, $Re = 10^8$

	$\overline{C_{M_x}}$	$\overline{C_{M_y}}$	$\overline{C_{M_z}}$	$\overline{M_x}\ [N/m]$	$\overline{M_y}\ [N/m]$	$\overline{M_z}\ [N/m]$
Grid 1	-0.00549140	-0.06785840	0.00270050	-3186.399	-39375.01	1556.972
Grid 2	-0.00121969	-0.07856030	-0.00007109	-707.7282	-45584.81	-41.25015
Grid 3	-0.00466444	-0.07153042	0.00250077	-2706.553	-41505.71	1451.078

Table 5.8 shows that the absolute values of the moments in the vertical direction are smaller than the ones in the other directions, which was to be expected given the symmetry of the structure.

Regarding the average moments in y-direction, which are several orders of magnitude larger than the moments in the other two directions, this is consistent with the fact that the forces in the streamwise direction, F_x, and the force in the vertical direction, F_z, have the most magnitude of the forces acting on the structure, since this is the pair of forces that will generate M_y. Again, the magnitude of this moment is expected to be smaller in a simulation where the net is deformable and permeable.

5.3.4 Flow Analysis

In this subsection, the flow will be analysed by means of instantaneous velocity plots, streamline patterns and also recurring to show the eddy viscosity influence on the flow, by means of ν_t/ν plots, since this will show the influence of turbulence in the flow, which may explain the frequency behaviour seen above.

Some instantaneous velocity plots of Grid 1 are illustrated in Figure 5.20.

From Figures 5.20 (a) and (b) it is possible to see that, away from the structure, in the hanging nodes from the largest cell size to the second largest cell size there exists some numerical error affecting the flow, however, since this behaviour is far away from the structure (more than $30d$ away from the structure, the influence of this numerical artifact on the results obtained should be minimal.

Figure 5.20 (c) shows that the wake created by the structure is more than $17d$ long and Figures 5.20 (d) and (e) show the increase in flow velocity under the structure due to the tapered geometry of the structure and the angle formed by the sides and the bottom of the net, which leads to the formation of a vortex underneath the structure in addition to the ones formed in the wake of the bluff body.

In Figure 5.21 all regions of the flow with $\nu_t < 2\nu$ are left white, so that the only the "viscous region" of the flow is visible. It is evident that the influence of turbulence in the flow is very low, since only the region close to the wall and the near wake have values of eddy viscosity over 2ν. This explains the frequency

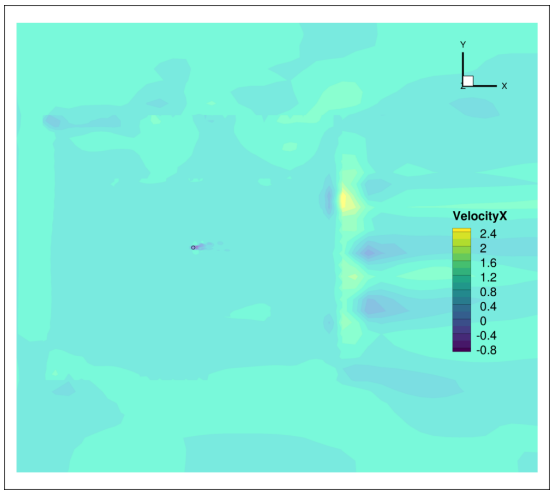

(a) Top-down View ($x - y$ plane)

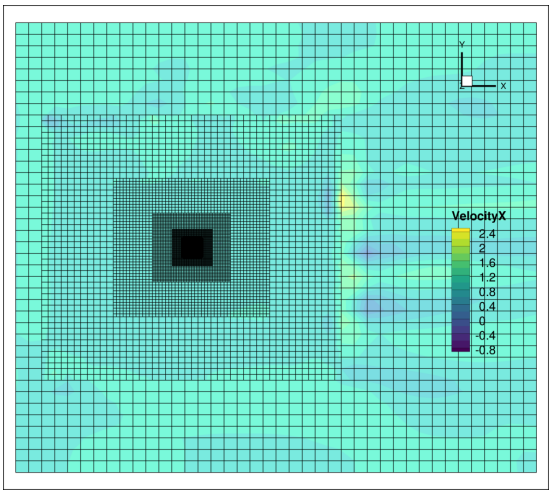

(b) Top-down View ($x - y$ plane): Overlayed grid

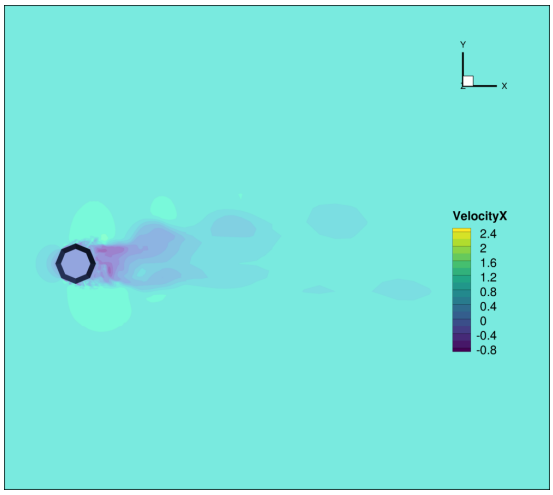

(c) Top-down View ($x - y$ plane): Close-up of the structure

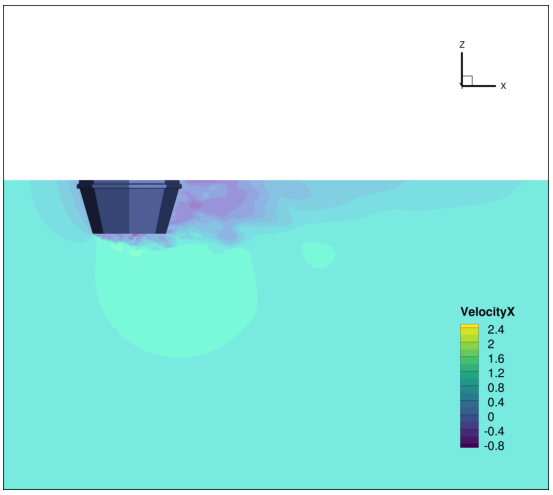

(d) Side View ($x - z$ plane): Close-up of the structure

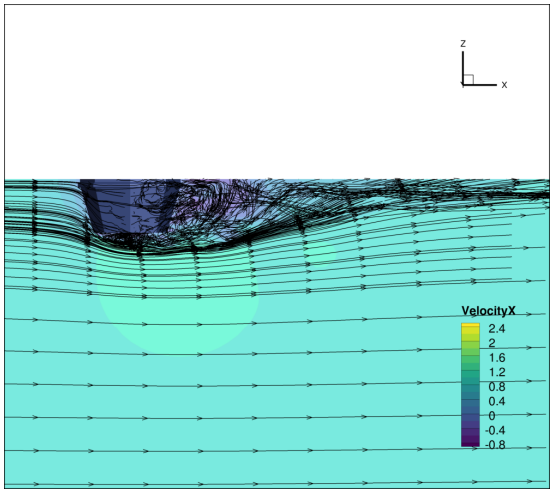

(e) Side View ($x - z$ plane): Close-up of the structure with streamtraces

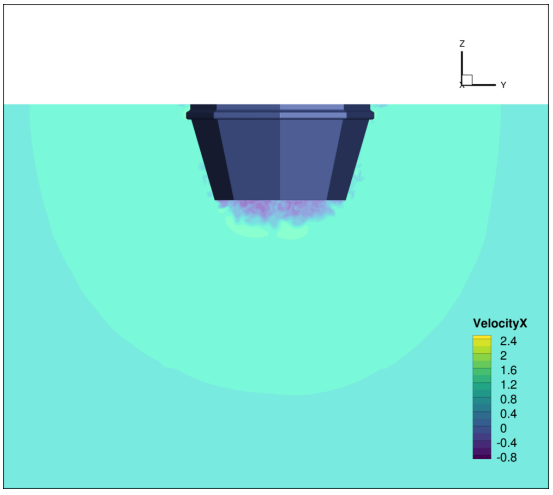

(f) Side View ($y - z$ plane): Close-up of the structure

Figure 5.20: Instantaneous velocity plots, at the last time-step using Grid 1.

behaviour seen previously, since there does not seem to be enough diffusion from the turbulence model to dampen the turbulent fluctuations at the Reynolds number of the simulation.

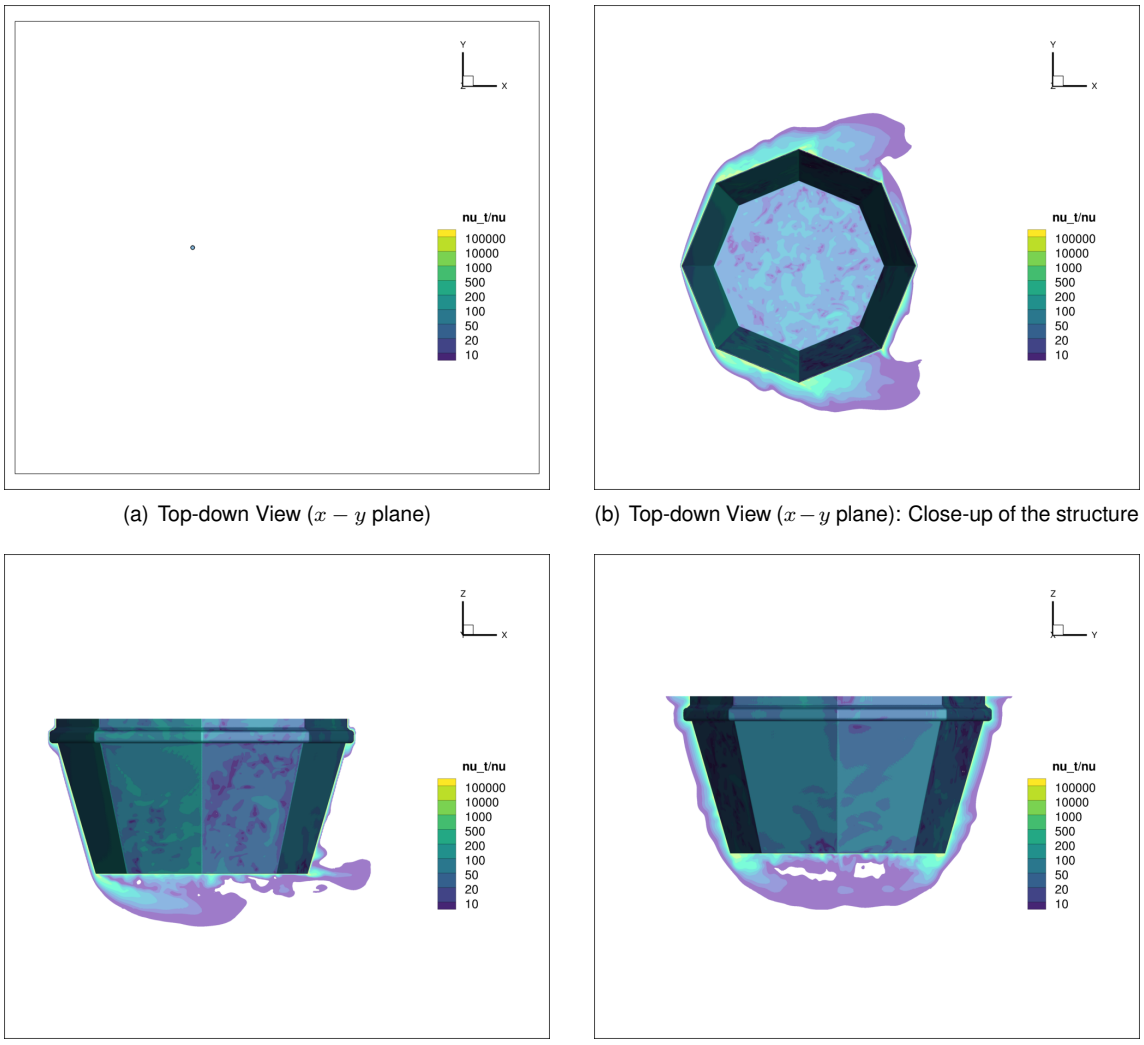

(a) Top-down View ($x - y$ plane)

(b) Top-down View ($x - y$ plane): Close-up of the structure

(c) Side View ($x - z$ plane): Close-up of the structure

(d) Side View ($y - z$ plane): Close-up of the structure

Figure 5.21: ν_t/ν plots, at the last time-step using Grid 1.

5.3.5 Conclusions From This Study

This study allows to make some estimations regarding the average value of the forces acting on the structure: the force in the x-direction is in the vicinity of $2300\ N$, the force in the y-direction should be a little under $200\ N$, while the force in the z-direction is near $2000\ N$. An estimation of the average value of the moments is also possible, with the moments around x close to $-3000\ N/m$, the moments around y are clearly the strongest moments acting on the structure, about $40000\ N/m$ and the moments in the z-direction approximately $1500\ N/m$.

Not much can be said about the frequency behaviour since the results obtained did not show a "RANS-like" behaviour, but given that the available literature on flow around bluff bodies at such a high Reynolds number is not extensive enough, comparisons are not possible.

The size of the near-wall cells is most likely too large which contributed to values of eddy viscosity which are too low. It was not possible to generate a new grid and perform new simulations due to time and computational constraints.

From a computational point of view, given the size of the domain and complexity of the structure it is

clear that the choices regarding the use of unstructured grids and the use of wall functions, made with the knowledge taken from the two preliminary studies, were appropriate choices, since the computational time used allowed for the extraction of useful information from the simulations without rendering the simulations prohibitively expensive. Even so, with as much computational resources as were used in this case, the results obtained are still not ideal. A lot more investigation can be made in this field, both in terms of the use of unstructured grids, perhaps with smaller grid sizes or with smaller cell size jumps in the far field, and in terms of the use of wall functions at this Reynolds numbers. These investigations, motivated by projects such as off-shore aquaculture structures or off-shore wind turbine installations, will be able to better predict the behaviour of bluff bodies in very high Reynolds number flows.

Chapter 6

Conclusions

This chapter will serve to synthesise the conclusions of this investigation, including the main conclusions from each of the two preliminary studies performed. Additionally, possible avenues for future work to be done in the study of flow around bluff bodies will be laid out.

6.1 Achievements

The first preliminary study made clear the differences in the behaviour of the flow around cylinders with three different cross section geometries. An increase in the number of faces of a polygonal cylinder leads to an increased similarity with the behaviour of the flow around the circular cylinder, corroborating the results of the literature. The orientation of the cylinder has also a significant impact on the behaviour of the flow and it is not the geometry of the stagnation point (corner or face) that influences the flow, but whether the width of the projected cylinder is determined by faces parallel to the flow or sharp corners.

From a computational standpoint, the first preliminary study also showed that the simulations performed with unstructured grids showed the necessary robustness, allowing for stable simulations with acceptable convergence.

The second preliminary study showed that the use of wall functions improved the robustness of the simulations. For the circular cylinder, the results of the largest and smallest values of near-wall cell size for the circular cylinder case with wall functions were consistent, whereas the intermediate size showed a larger wake width, while for the polygonal cylinders, only the two largest sizes of near-wall cell resulted in good iterative convergence and the consistency of those two grid sets was better than for the circular cylinder. A significant increase in numerical uncertainty for the largest near-wall cell size for all grid sets was reported.

In this study, the circular cylinder was the only where ”RANS-like” solutions resulted from all the simulations. The hexadecagonal cylinder resulted in some ”RANS-like” solutions but the frequency content of the time histories depended heavily on grid/time refinement. Consequently it is not possible to understand if this is caused by lack of diffusion from the turbulence model.

The results also show that even at such high Reynolds numbers and with significant difficulties to

guarantee iterative convergence, it is the sharp corners on the surface of the polygonal cylinders that produce a significant increase of the force coefficients when compared to the circular cylinder.

This study suggested that wall functions can be an efficient option to simulate very high Reynolds numbers flows around bluff bodies, but that the size of the near-wall cells have a strong influence on the solution.

Concerning the final 3D study, estimations were made regarding the average values of forces and moments acting on the surface of the structure. However, given the simplifications made (lack of a deformable, permeable net) it is necessary to carefully analyse the results in order to make predictions regrading the structural analysis of the floating structure.

The frequency content showed behaviour similar to the one found in the simulations of flow around the octagonal cylinder in the second preliminary study, in that it did not show a ”RANS-like” behaviour.

The near wall cell size used in the 3D study was most likely too large and as such the levels of eddy-viscosity are too low. Generation of a new grid was not possible in the available time.

Given the complexity of the structure and computational time expended on the simulations there is confidence in the computational choices made in the final study i.e. use of unstructured grids and use of ”automatic” wall functions.

6.2 Future Work

With the increase in interest in larger structures in open sea areas (aquaculture structures, wind farms, etc.) the need for the study of flows at very high Reynolds numbers increases as well. Given that this is a quasi-unexplored area of fluid dynamics, further investigations on this topic are recommended.

The use of wall functions seems to be acceptable at very high Reynolds numbers but the high influence of the size of the near-wall cell on the force coefficients needs to be analysed by means of a sensitivity study for the near-wall cell size.

Simulations of flow around the aquaculture structure without the simplifications made in this work can be performed to achieve better approximations for the quantities under study, however in order for those simulations to have a good degree of realism, fluid-structure interactions and deformation of the net need to be taken into account.

Bibliography

[1] FAO - Food and Agriculture Organization of the United Nations. The State of World Fisheries and Aquaculture 2018 - Meeting the sustainable development goals. Rome, 2018. Licence: CC BY-NC-SA 3.0 IGO.

[2] H. A. Khaledi and H. I. Anderson. On vortex shedding from a hexagonal cylinder. *Physics Letters A*, 2011.

[3] L. Eça, G. Saraiva, G. Vaz, and H. Abreu. The pros and cons of wall functions. In *OMAE2015-41518 Paper, Proceedings of the ASME 2015 34th International Conference on Ocean, Offshore and Arctic Engineering*, volume 1-6, St John's, NL, Canada, 2015. OMAE.

[4] L. Eça and G. F. Neves. On the Simulation of Very High Reynolds Number Flows Around Bluff Bodies Using the RANS Equations. Technical report, Instituto Superior Técnico/MARIN Partnership, 2020.

[5] L. Eça. Grid generation tools for structured grids. Technical report, MARIN/IST Cooperative Research Project, May 2003.

[6] MARIN. ReFRESCO Controls Documentation, version 2.5.0.

[7] C. H. K. Williamson. Vortex Dynamic in the Cylinder Wake. *Annual Review of Fluid Mechanics*, 28: 477–539, 1996.

[8] A. Sohankar, C. Norberg, and L. Davidson. Numerical simulation of unsteady low-reynolds number flow around rectangular cylinders at incidence. *Journal of Wind Engineering and Industrial Aerodynamics*, 1997.

[9] H. R. Bosch and R. M. Guterres. Wind tunnel experimental investigation on tapered cylinders for highway support structures. *Journal of Wind Engineering and Industrial Aerodynamics*, 89: 1311–1323, 2001.

[10] S. J. Xu, W. Zhang, L. Gan, and Y. Zhou. Experimental study of flow around polygonal cylinders. *Journal of Fluid Mechanics*, 812:251–278, 2017.

[11] J. H. Ferziger and M. Peric. *Computational Methods for Fluid Dynamics*. Springer-Verlag Berlin Heidelberg, 3rd edition edition, 2002.

[12] F. Menter. Two-equation eddy-viscosity turbulence models for engineering applications. *AIAA Journal*, 32(8), 1994.

[13] F. Menter, M. Kuntz, and R. Langtry. Ten Years of Industrial Experience with the SST Turbulence Model. *Turbulence, Heat and Mass Transfer*, 4, 2003.

[14] F. Menter, Y. Egorov, and D. Rusch. Steady and Unsteady Flow Modelling Using the $k\sqrt{k}l$ Model. In *Proceedings of the International Symposium on Turbulence, Heat and Mass Transfer, vol 5, p.403-406*. Ichmt Digital Library Online. Begel House Inc., 2006.

[15] F. Menter and Y. Egorov. The scale-adaptive simulation method for unsteady turbulent flow predictions. part 1: Theory and model description. *Flow, Turbulence and Combustion*, 85:113–138, 2010.

[16] B. Launder and D. Spalding. The Numerical Computation of Turbulent Flows. *Computer Methods in Applied Mechanics And Engineering*, 3, 1974.

[17] D. Wilcox. *Turbulence Modeling for CFD*. DCW Industries, 2006.

[18] D. A. Johnson and L. S. King. Mathematically simple turbulence closure model for attached and separated boundary layers. *AIAA Journal*, 23(11):1684–1692, 1985.

[19] J. Rotta. Über eine methode zur Berechnung turbulenter Scherströmungen. *Aerodinamische Versuchsanstalt Göttingen*, Rep.69 A14, 1968.

[20] J. Rotta. Turbulente strömungen. *BG Teubner Stuttgart*, 1972.

[21] R. M. Costa and L. Eça. Assessing rans numerical and modelling properties in the simulation of the flow around fixed and moving cylinders. Master's thesis, Universidade de Lisboa - Instituto Superior Técnico, 2019.

[22] L. Eça, F. Pereira, and G. Vaz. Viscous flow simulations at high reynolds numbers without wall functions: Is $y+ \simeq 1$ enough for the near-wall cells? *Computers & Fluids*, 170:157–175, 2018.

[23] F. Menter and T. Esch. Elements of industrial heat transfer predictions. In *16th Brasilian Congress of Mechanical Engineering*, 2001.

[24] Dassault Systèmes. `https://www.3ds.com/products-services/solidworks/`, 2020. [online: viewed on the 27th of May 2020].

[25] NUMECA. `https://www.numeca.com/en_eu/product/hexpress`, 2019. [online: viewed on the 26th of November 2019].

[26] P. Crepier. Ship resistance prediction: Verification and validation exercise on unstructured grids. In *MARINE 2017 Computational Methods in Marine Engineering VII*. International Center for Numerical Methods in Engineering (CIMNE), 2017. ISBN: 978-84-946909-8-3.

[27] MARIN. https://www.refresco.org/resources/overview-2/, 2019. [online: viewed on the 26th of November 2019].

[28] L. Eça, M. Hoekstra, and J. Windt. Practical Grid Generation Tools with Applications to Ship Hydrodynamics. In *8th international Conference on Numerical Grid Generation in Computational Field Simulations*, Honolulu, Hawaii, U.S.A., June 2002.

[29] L. Eça and M. Hoekstra. Near-Wall Profiles of Mean Flow and Turbulence Quantities Predicted by Eddy-Viscosity Turbulence Models. *International Journal for Numerical Methods in Fluids*, 63(8): 953–988, 2010.

[30] TecPlot. www.tecplot.com, 2020.

[31] R. M. Costa, L. Eça, and A. Koop. Assessing RANS Numerical and Modeling Properties in the Simulation of the Flow Around Captive and Moving Cylinders. In *OMAE2020-8385, Proceedings of the ASME 2015 39th International (Virtual) Conference on Ocean, Offshore and Arctic Engineering*. OMAE, August 2020.

[32] J. Brouwer, J. Tukker, and M. Rijsbergen. Uncertainty Analysis of Finite Length Measurements Signals. In *3rd International Conference on Advanced Model Measurement Technology for the EU Maritime Industry*, Gdansk, Poland, 2013. AMT'13.

[33] L. Eça and M. Hoekstra. Procedure for the Estimation of the Numerical Uncertainty of CFD Calculations Based on Grid Refinement Studies. *Journal of Computational Physics*, 262:104–130, 2014.

[34] L. Eça, G. Vaz, S. Toxopeus, and M. Hoekstra. Numerical Errors in Unsteady Flow Simulations. *ASME Journal of Verification, Validation and Uncertainty Quantification*, 4, June 2019.

[35] C. Norberg. An experimental investigation of the flow around a circular cylinder: influence of aspect ratio. *Journal of Fluid Mechanics*, 258, 1994.

[36] M. Kyia, H. Tamura, and M. Arie. Vortex shedding from a circular cylinder in moderate-Reynolds number shear flow. *Journal of Fluid Mechanics*, 141, 1980.

[37] A. N. Kolmogorov. Dissipation of Energy in the Locally Isotropic Turbulence. In *Proceedings of the Royal Society A: Mathematical, Physical and Engineering Sciences*, August 1991.

[38] A. N. Kolmogorov. The Local Structure of Turbulence in Incompressible Viscous Fluid for Very Large Reynolds Numbers. In *Proceedings of the Royal Society A: Mathematical, Physical and Engineering Sciences*, August 1991.

Appendix A

1st Preliminary Study - Additional Images

A.1 Preliminary Study 1

A.1.1 Time History Of The Forces

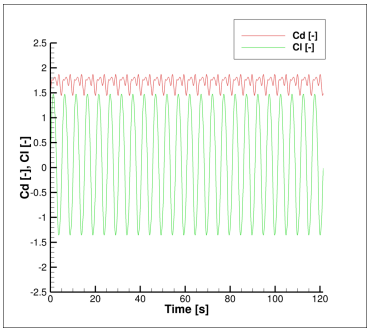

(a) Hexagonal cylinder with corner orientation

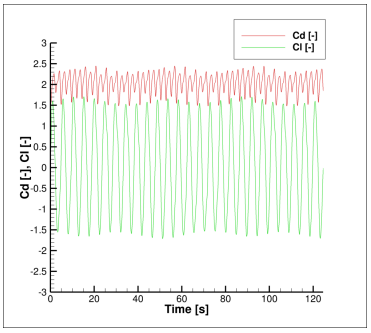

(b) Hexagonal cylinder with face orientation

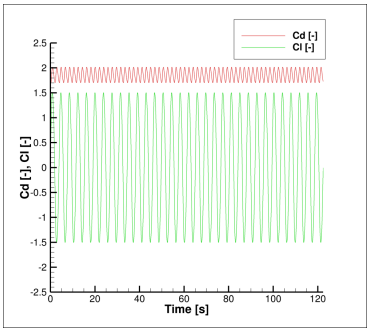

(c) Octagonal cylinder with corner orientation

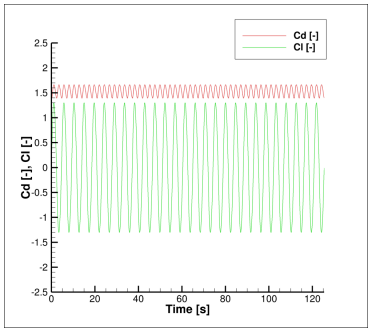

(d) Octagonal cylinder with face orientation

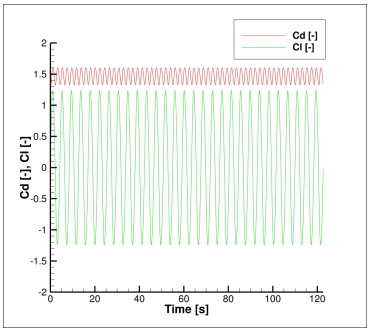

(e) Circular cylinder

Figure A.1: Evolution of C_d and C_L for the simulations with Grid 1 using the $KSKL$ model

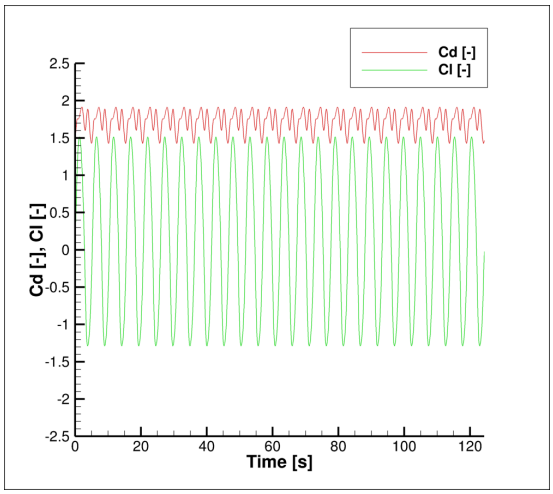

(a) Hexagonal cylinder with corner orientation

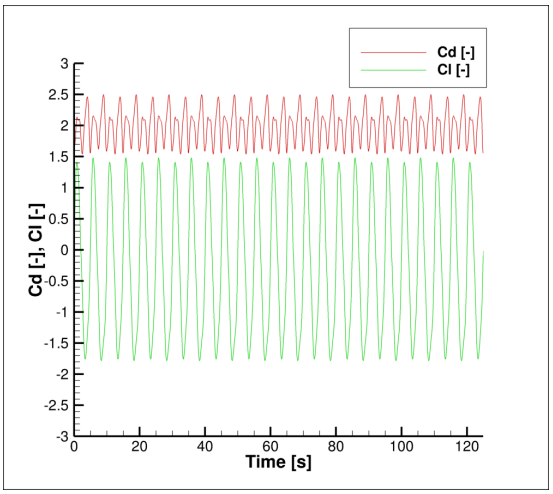

(b) Hexagonal cylinder with face orientation

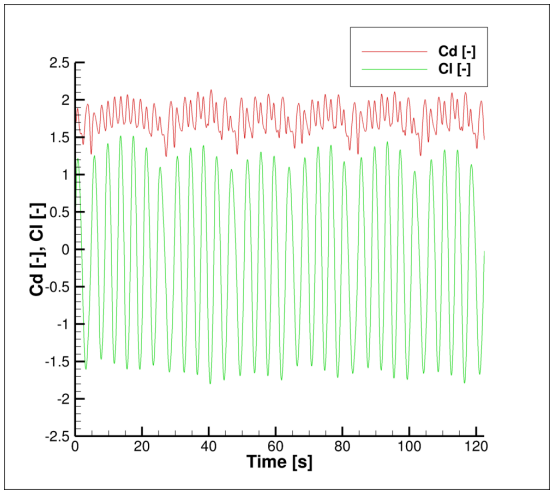

(c) Octagonal cylinder with corner orientation

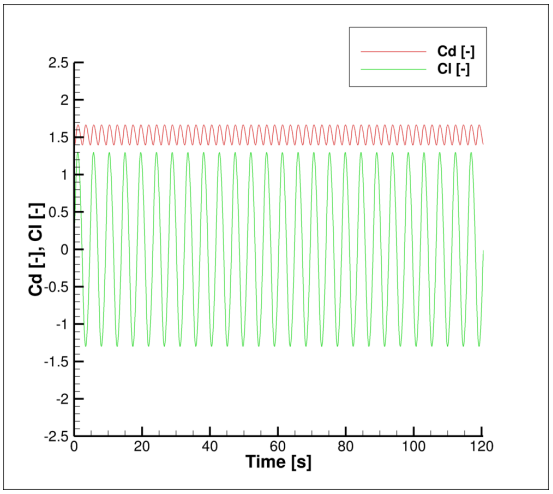

(d) Octagonal cylinder with face orientation

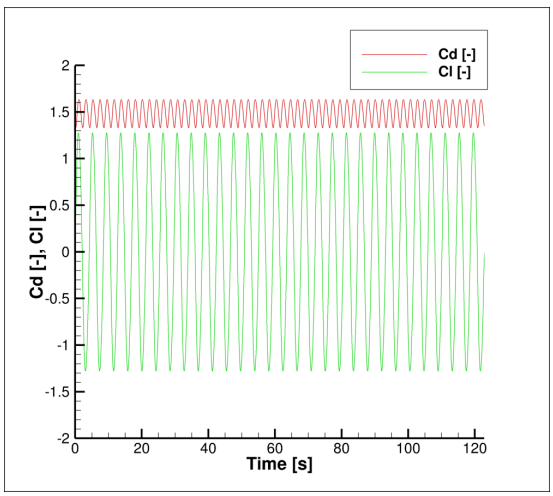

(e) Circular cylinder

Figure A.2: Evolution of C_d and C_L for the simulations with Grid 2 using the $k-\omega SST$ model

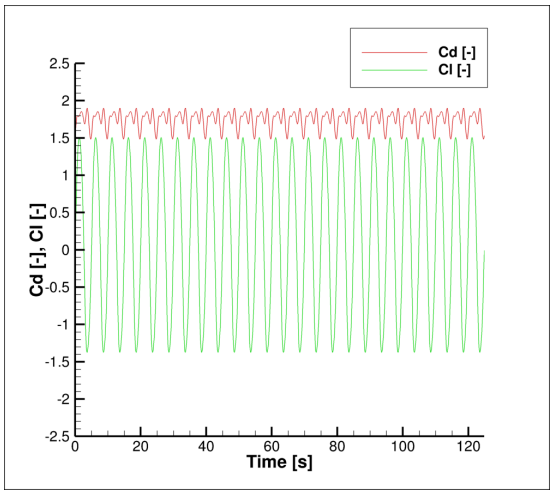

(a) Hexagonal cylinder with corner orientation

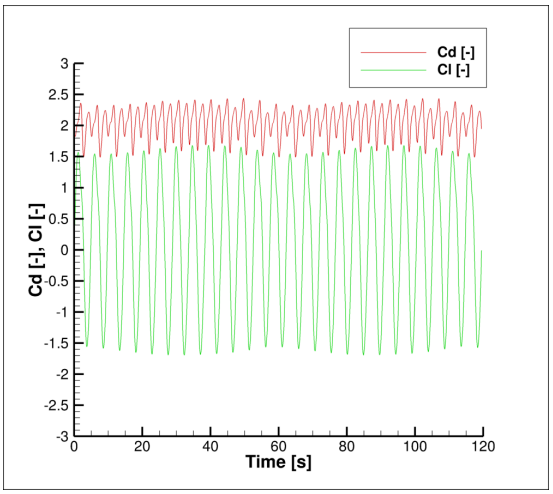

(b) Hexagonal cylinder with face orientation

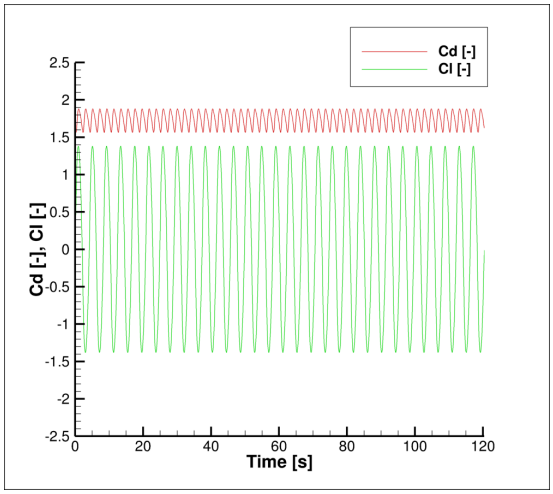

(c) Octagonal cylinder with corner orientation

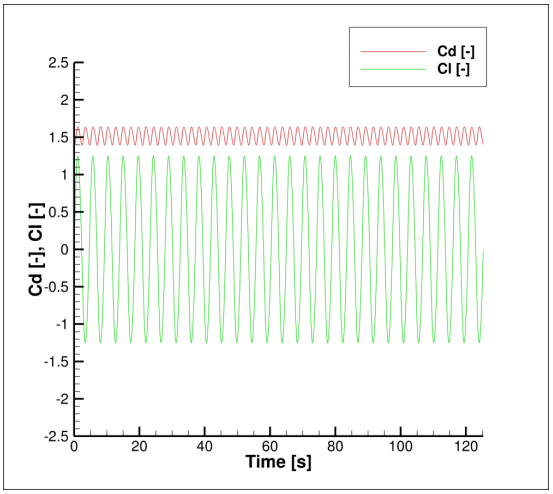

(d) Octagonal cylinder with face orientation

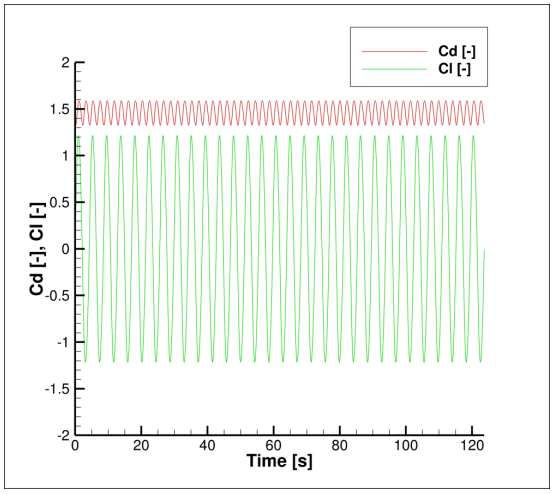

(e) Circular cylinder

Figure A.3: Evolution of C_d and C_L for the simulations with Grid 2 using the $KSKL$ model

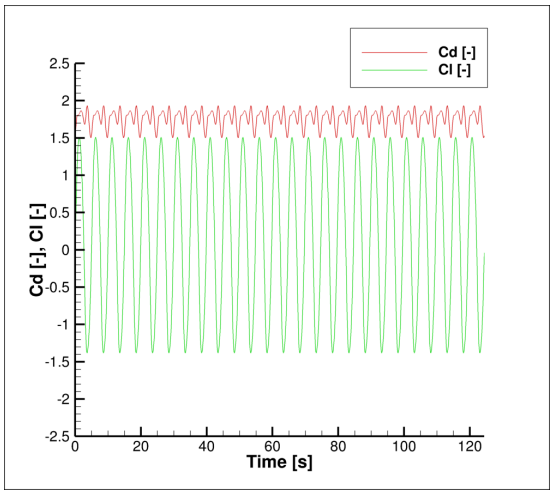

(a) Hexagonal cylinder with corner orientation

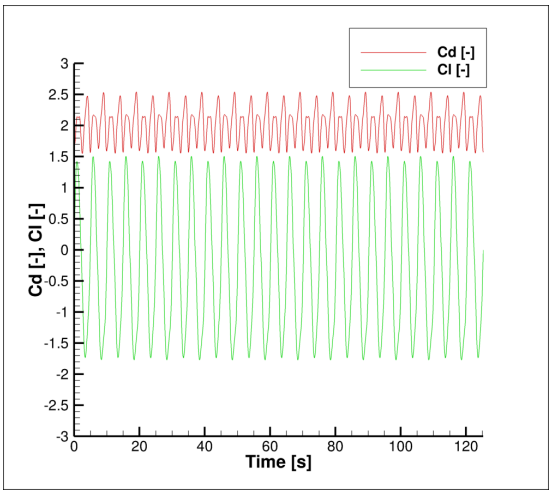

(b) Hexagonal cylinder with face orientation

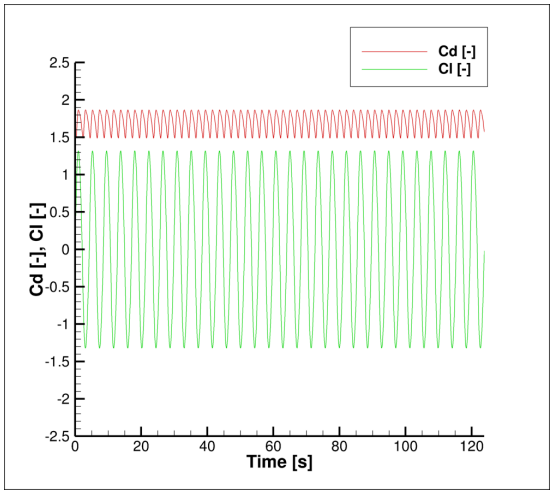

(c) Octagonal cylinder with corner orientation

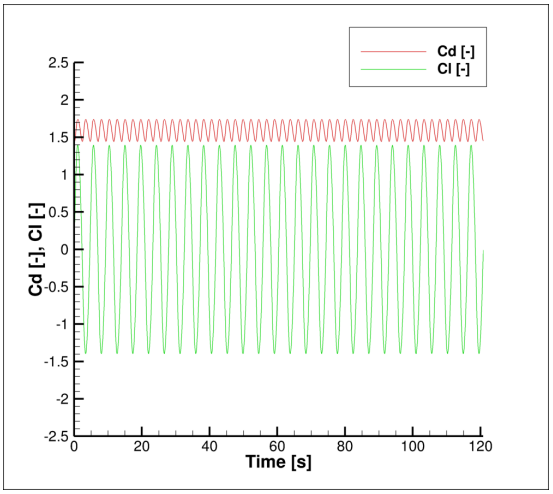

(d) Octagonal cylinder with face orientation

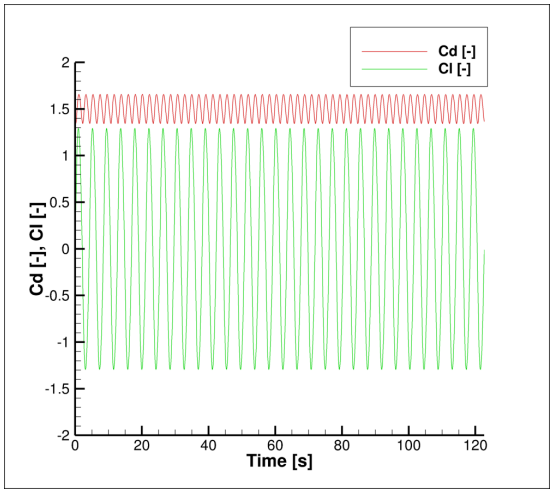

(e) Circular cylinder

Figure A.4: Evolution of C_d and C_L for the simulations with Grid 3 using the $k-\omega SST$ model

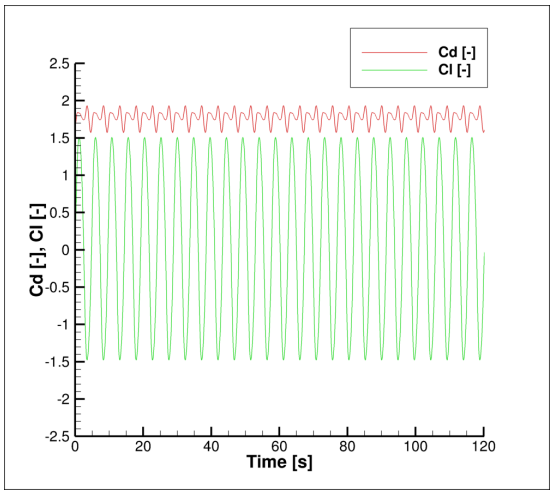

(a) Hexagonal cylinder with corner orientation

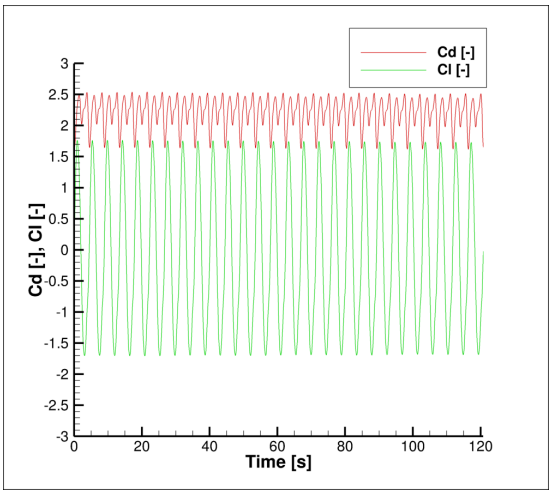

(b) Hexagonal cylinder with face orientation

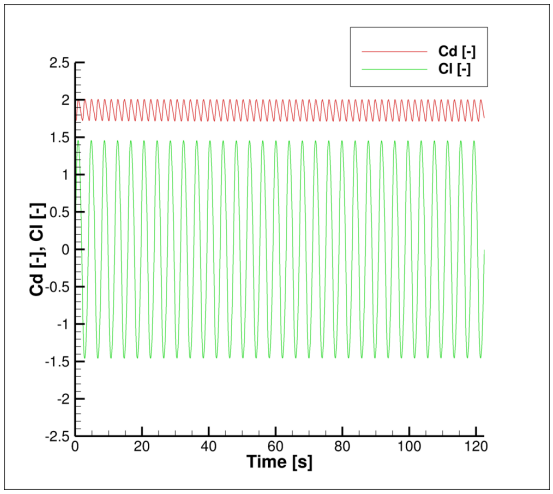

(c) Octagonal cylinder with corner orientation

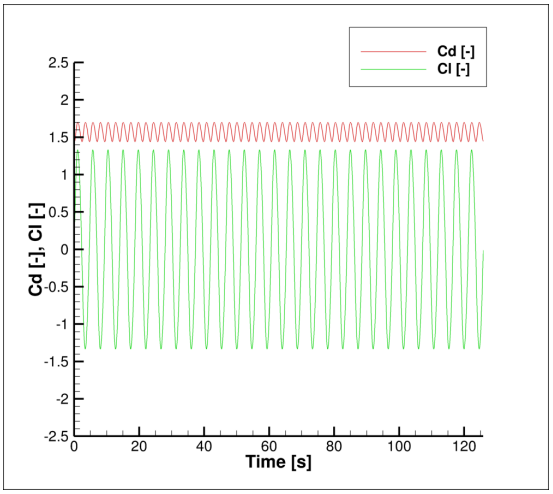

(d) Octagonal cylinder with face orientation

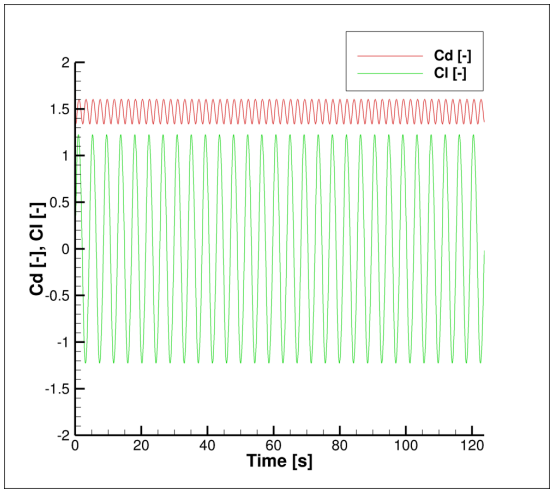

(e) Circular cylinder

Figure A.5: Evolution of C_d and C_L for the simulations with Grid 3 using the $KSKL$ model

A.1.2 Fast Fourier Transforms

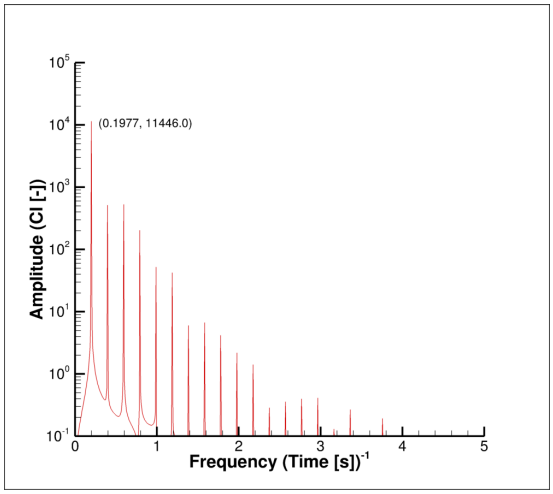

(a) Hexagonal cylinder with corner orientation

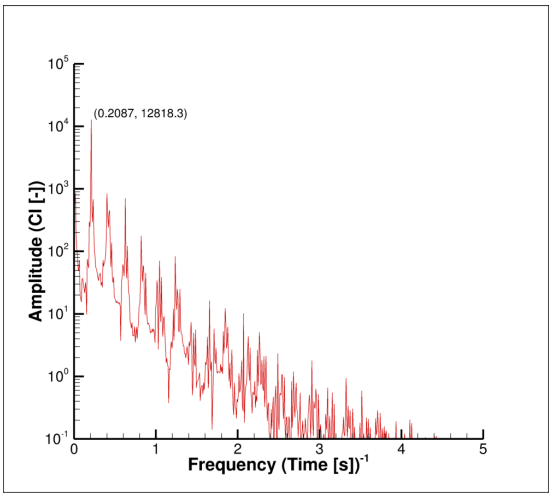

(b) Hexagonal cylinder with face orientation

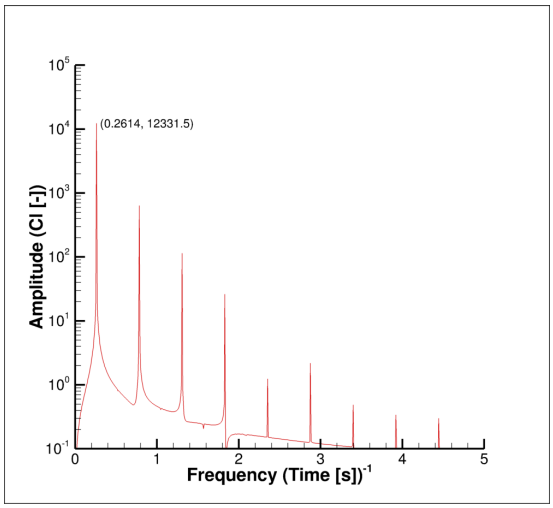

(c) Octagonal cylinder with corner orientation

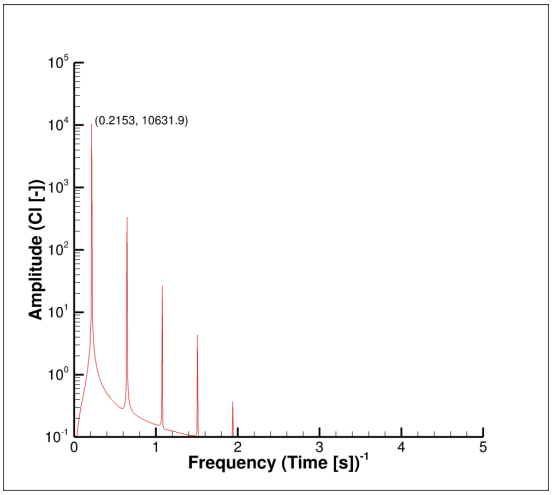

(d) Octagonal cylinder with face orientation

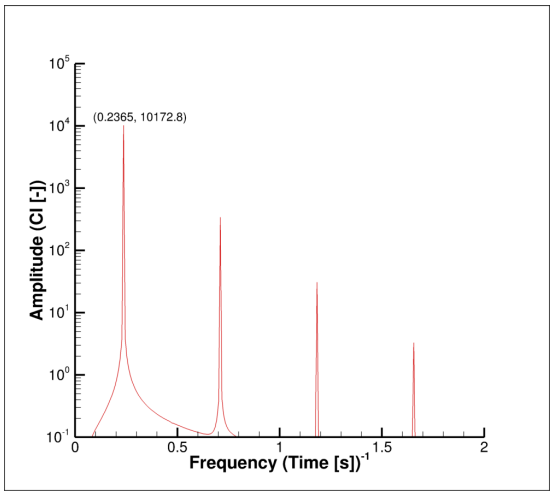

(e) Circular cylinder

Figure A.6: Fast Fourier Transfom plots obtained from the simulations with Grid 1 using the $KSKL$ model.

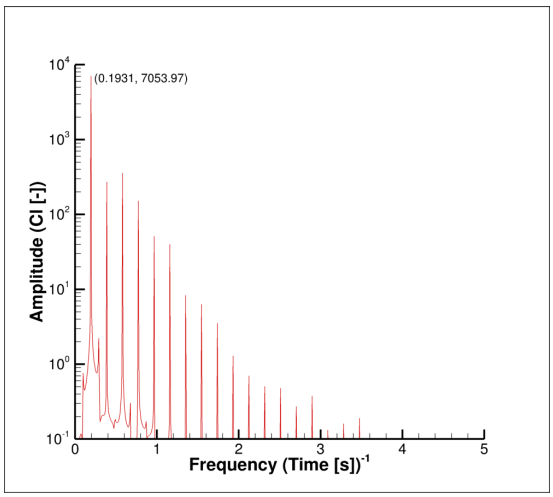

(a) Hexagonal cylinder with corner orientation

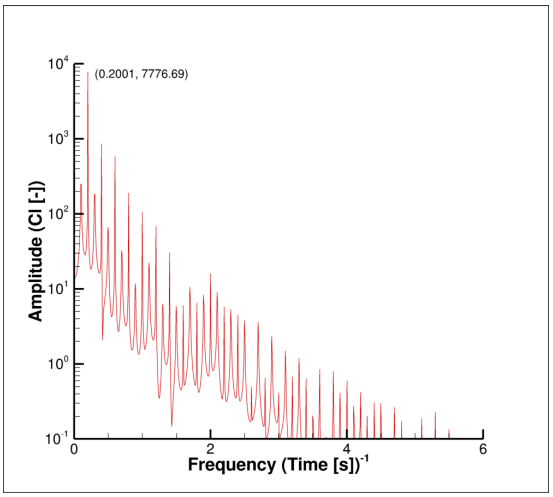

(b) Hexagonal cylinder with face orientation

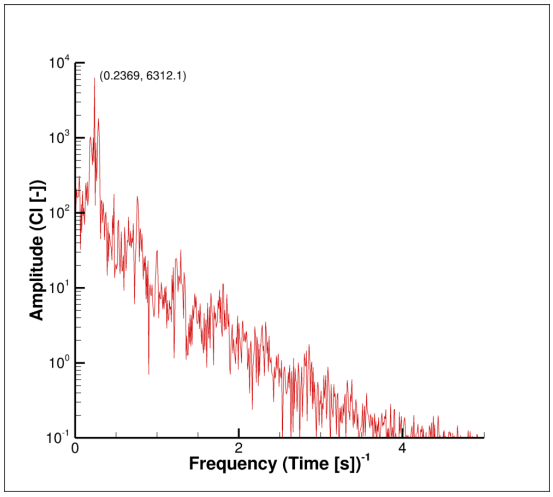

(c) Octagonal cylinder with corner orientation

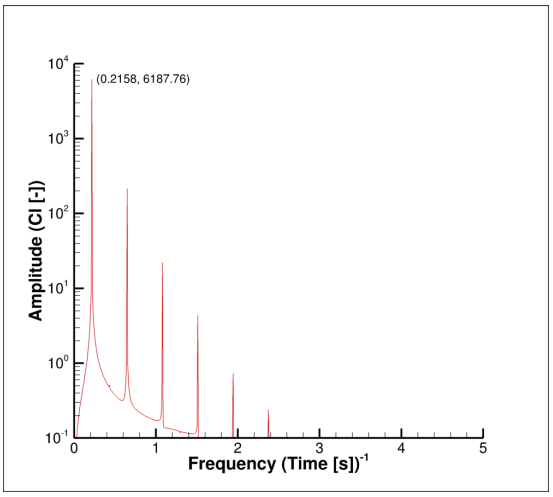

(d) Octagonal cylinder with face orientation

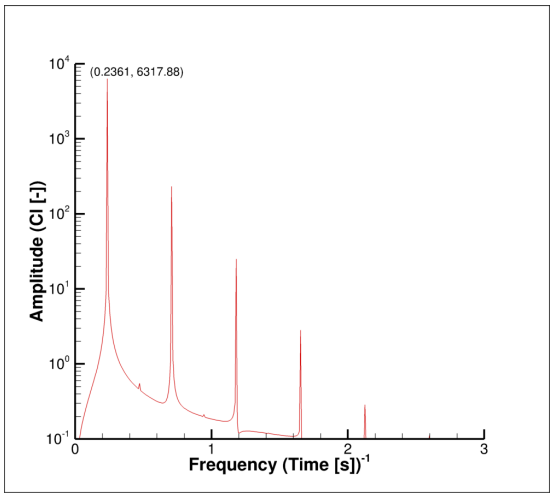

(e) Circular cylinder

Figure A.7: Fast Fourier Transfom plots obtained from the simulations with Grid 2 using the $k-\omega SST$ model.

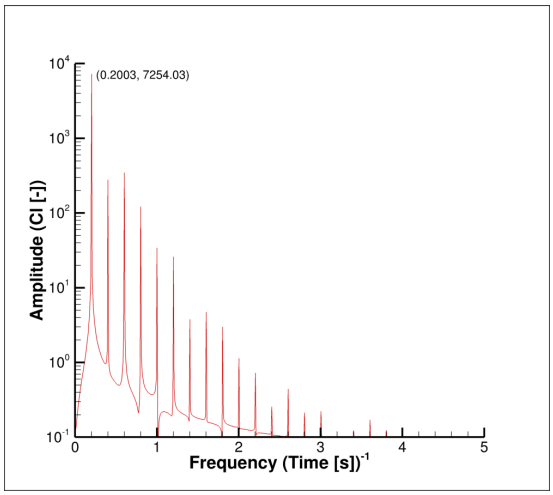

(a) Hexagonal cylinder with corner orientation

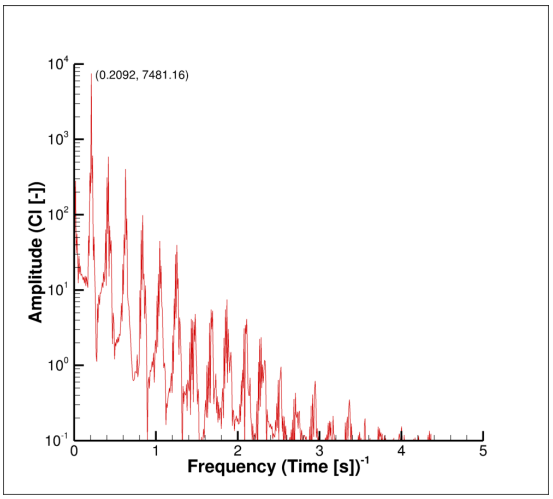

(b) Hexagonal cylinder with face orientation

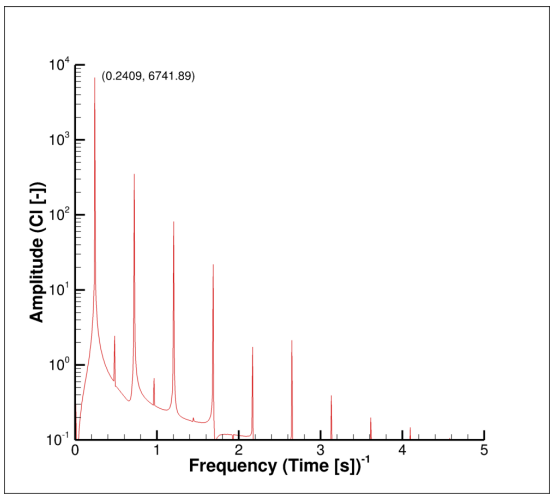

(c) Octagonal cylinder with corner orientation

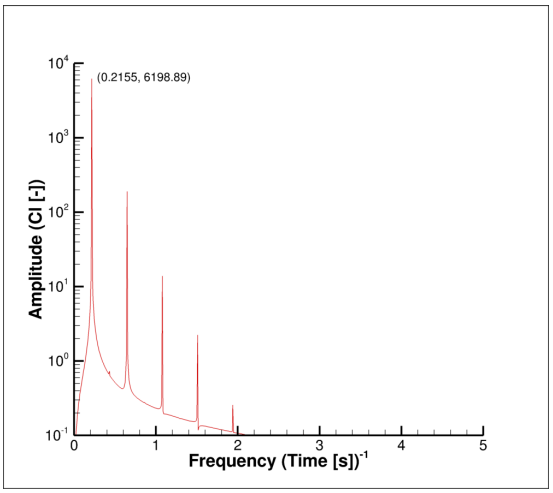

(d) Octagonal cylinder with face orientation

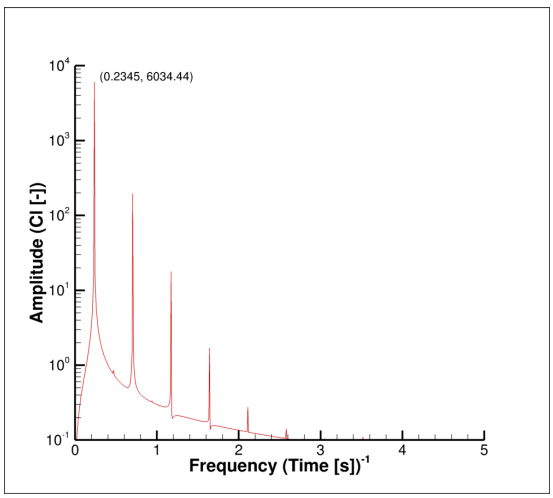

(e) Circular cylinder

Figure A.8: Fast Fourier Transfom plots obtained from the simulations with Grid 2 using the $KSKL$ model.

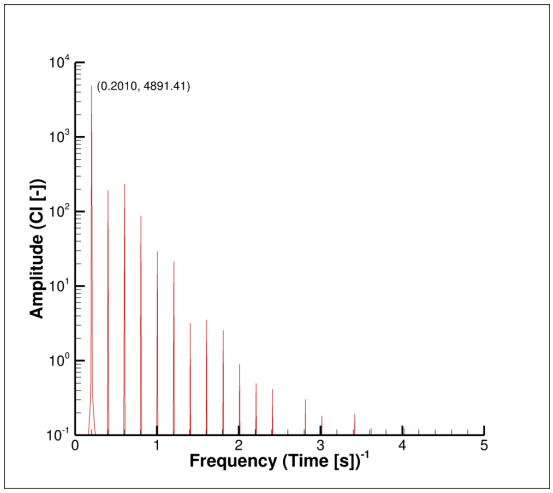

(a) Hexagonal cylinder with corner orientation

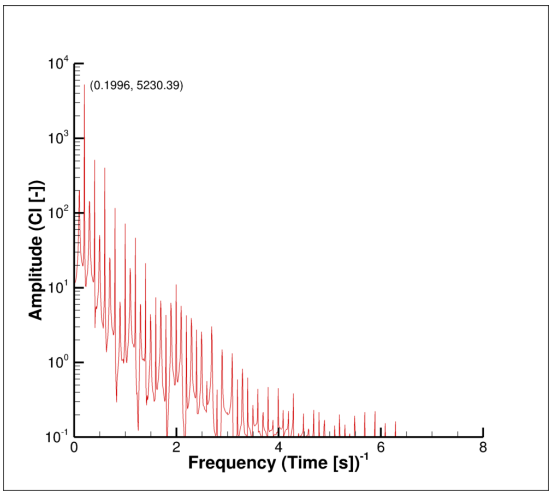

(b) Hexagonal cylinder with face orientation

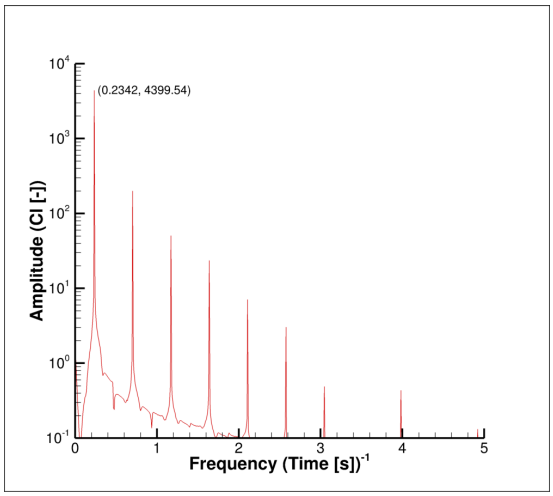

(c) Octagonal cylinder with corner orientation

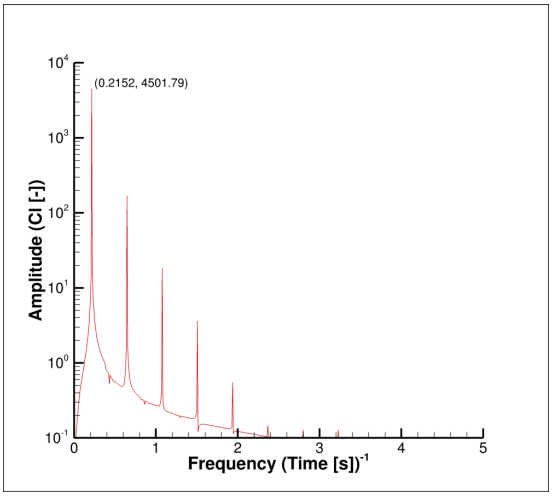

(d) Octagonal cylinder with face orientation

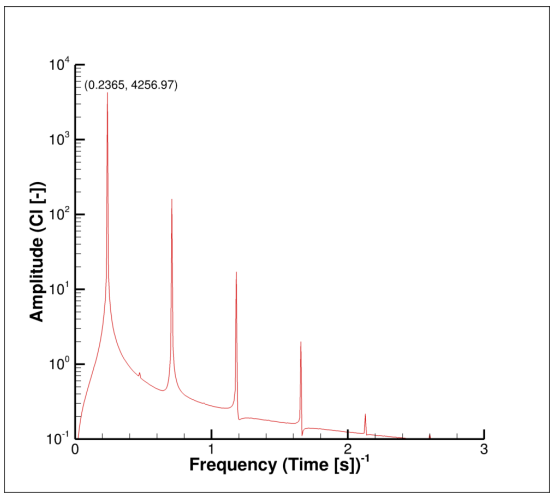

(e) Circular cylinder

Figure A.9: Fast Fourier Transfom plots obtained from the simulations with Grid 3 using the $k-\omega SST$ model.

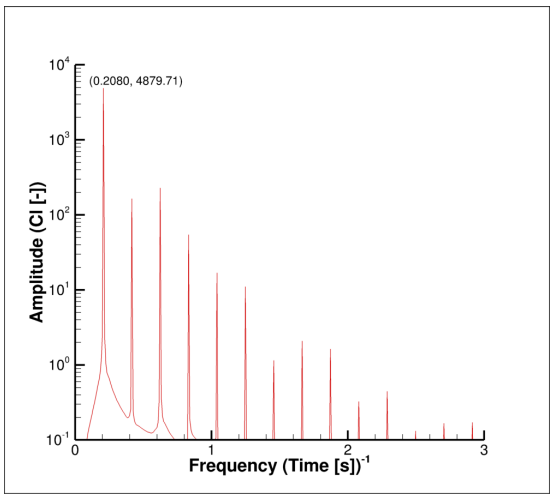

(a) Hexagonal cylinder with corner orientation

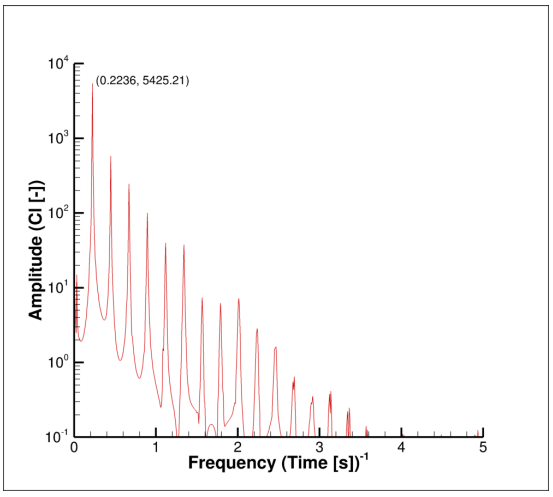

(b) Hexagonal cylinder with face orientation

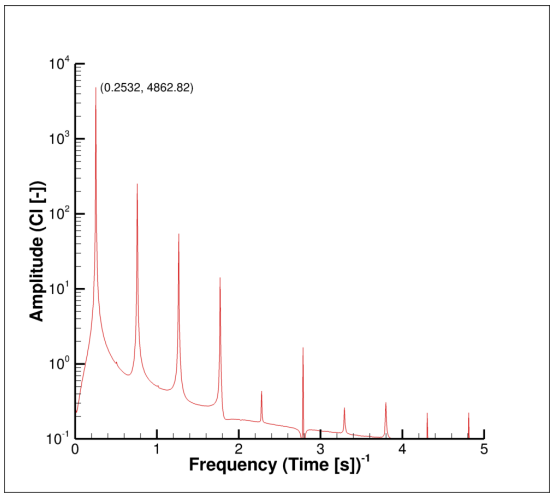

(c) Octagonal cylinder with corner orientation

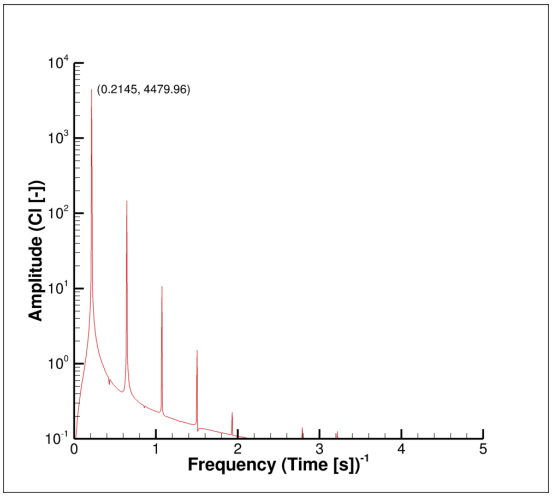

(d) Octagonal cylinder with face orientation

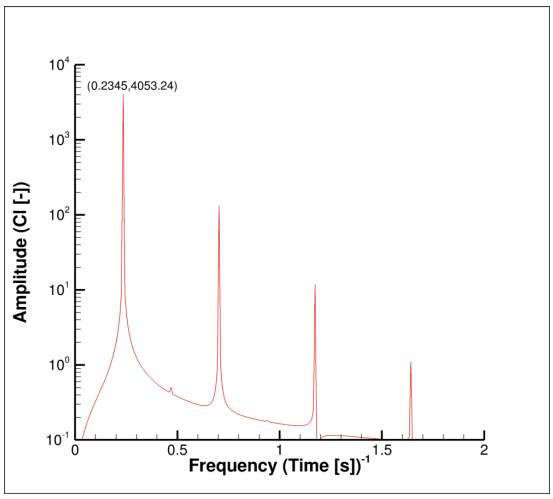

(e) Circular cylinder

Figure A.10: Fast Fourier Transfom plots obtained from the simulations with Grid 3 using the $KSKL$ model.

Appendix B

2nd Preliminary Study - Images from the Octagonal and Hexadecagonal Cylinders

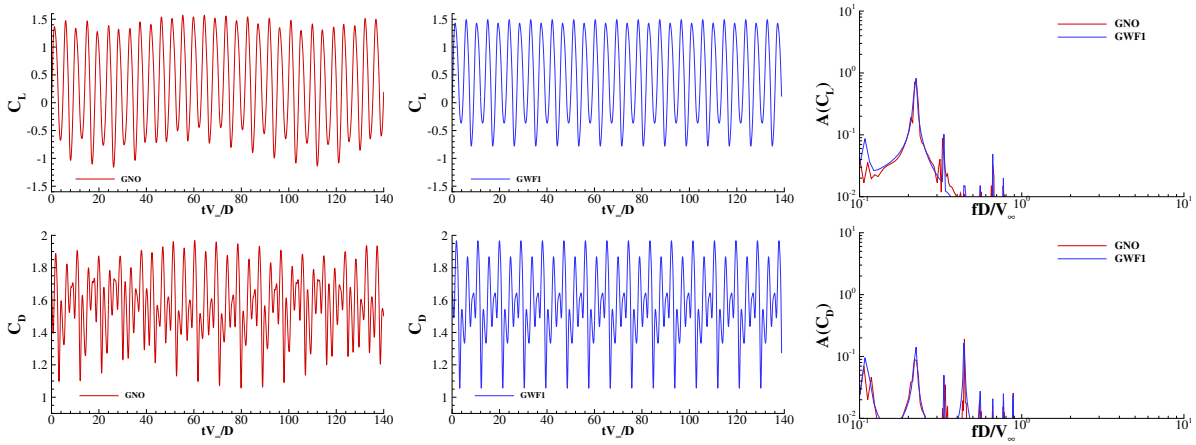

Figure B.1: Time history of the lift C_L and drag C_D coefficients and their frequency content. Simulations performed in the coarsest grids of sets GNO (without wall functions) and GWF1 (with wall functions). Flow around an octagonal cylinder at a Reynolds number of 10^8.

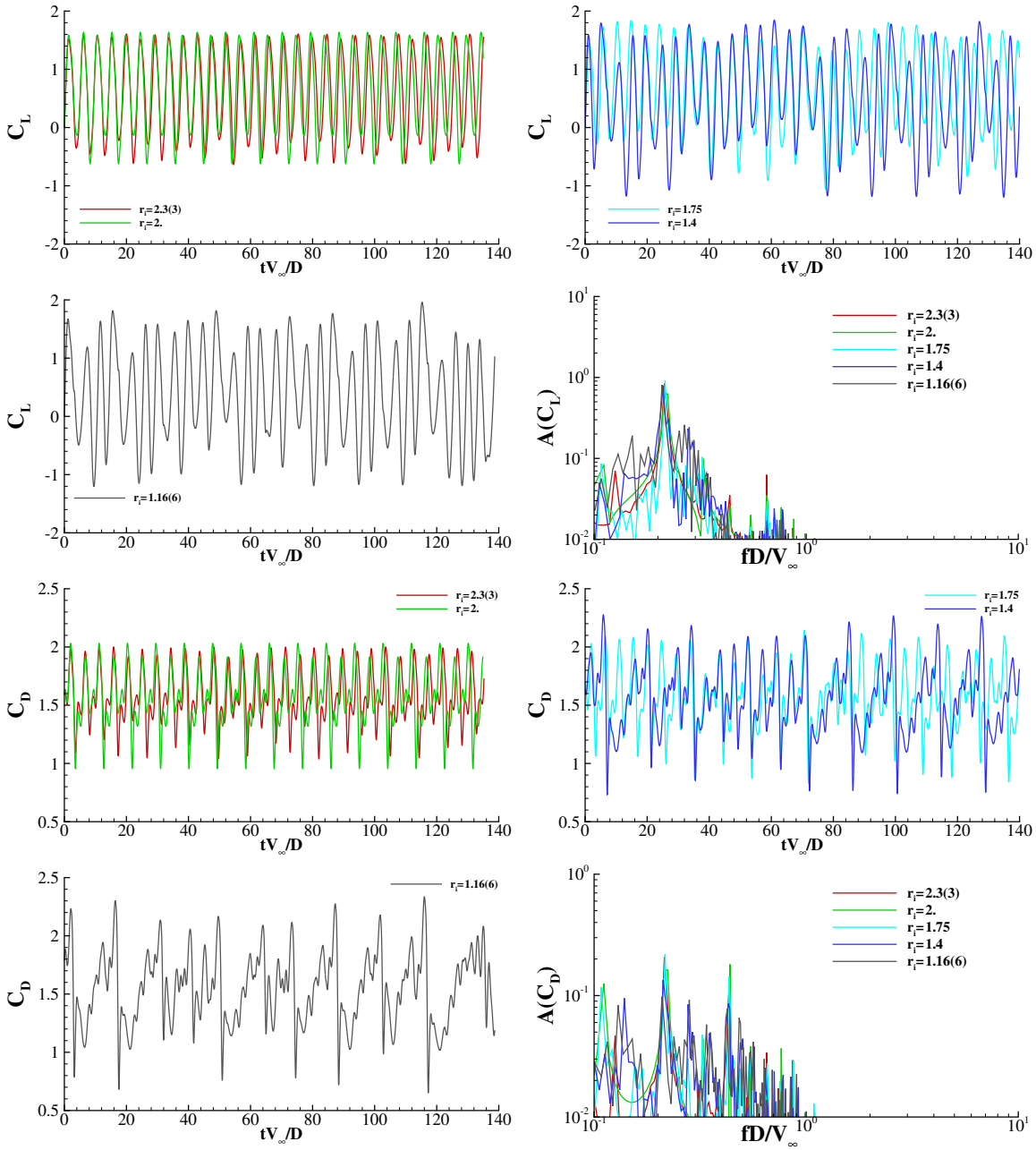

Figure B.2: Time histories of the lift C_L and drag C_D coefficients and their frequency content. Simulations performed in the grids of sets GWF2 (with wall functions). Flow around an octagonal cylinder at a Reynolds number of 10^8.

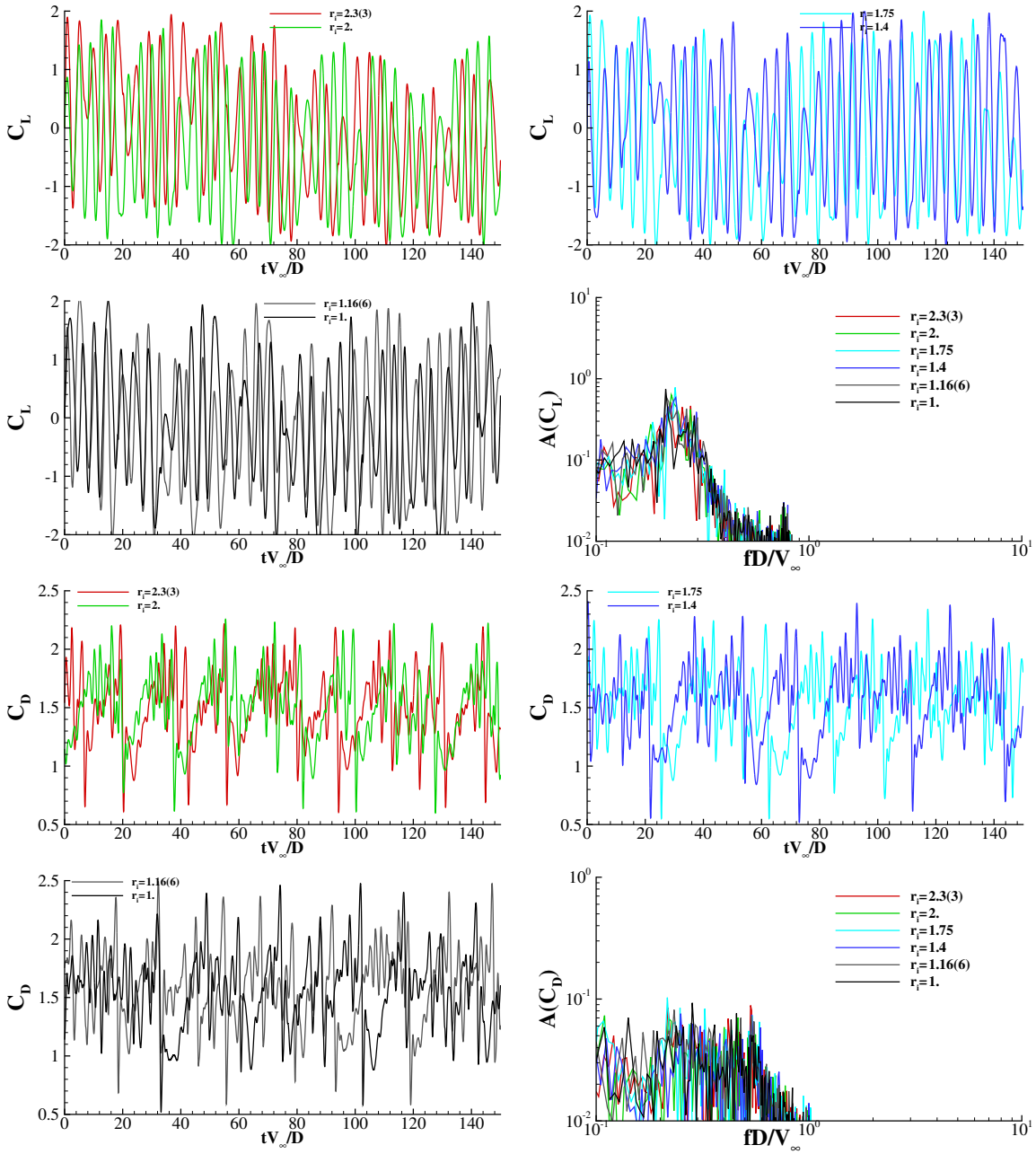

Figure B.3: Time histories of the lift C_L and drag C_D coefficients and their frequency content. Simulations performed in the grids of sets GWF3 (with wall functions). Flow around an octagonal cylinder at a Reynolds number of 10^8.

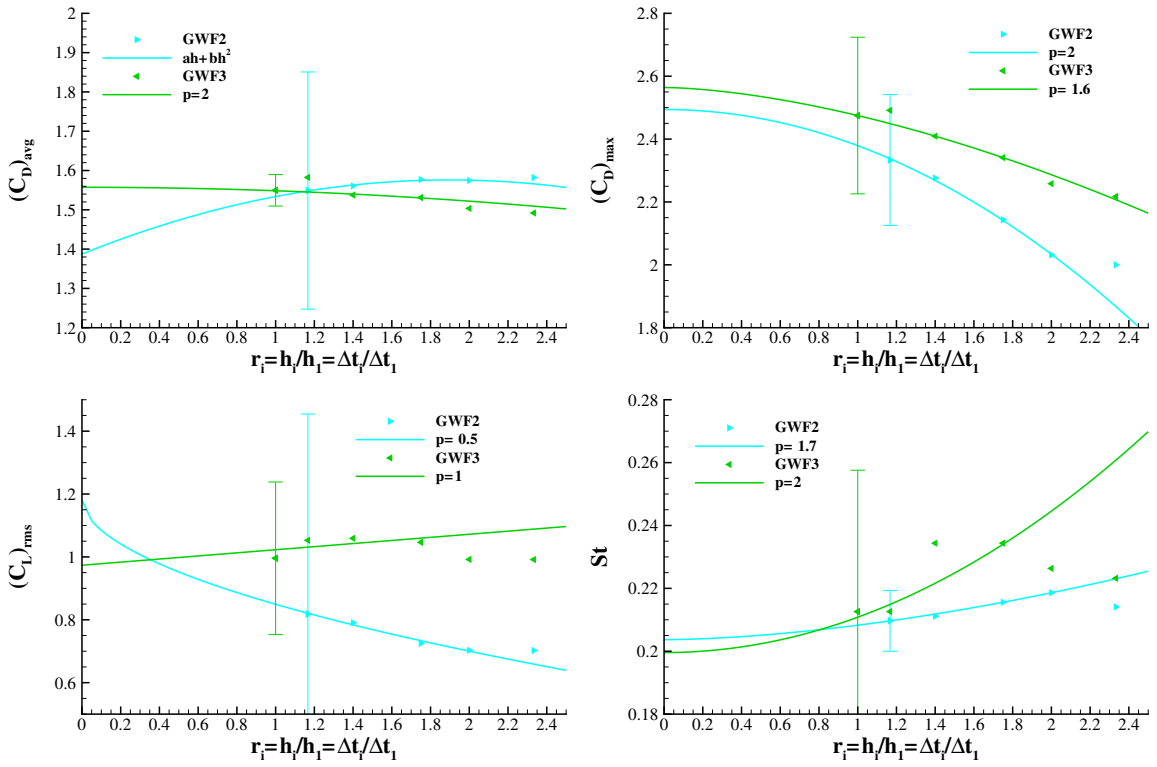

Figure B.4: Convergence with grid/time refinement of average $(C_D)_{avg}$ and maximum $(C_D)_{max}$ drag coefficient, root mean squared $(C_L)_{rms}$ lift coefficient and Strouhal number St. Flow around an octagonal cylinder at a Reynolds number of 10^8 calculated with wall functions.

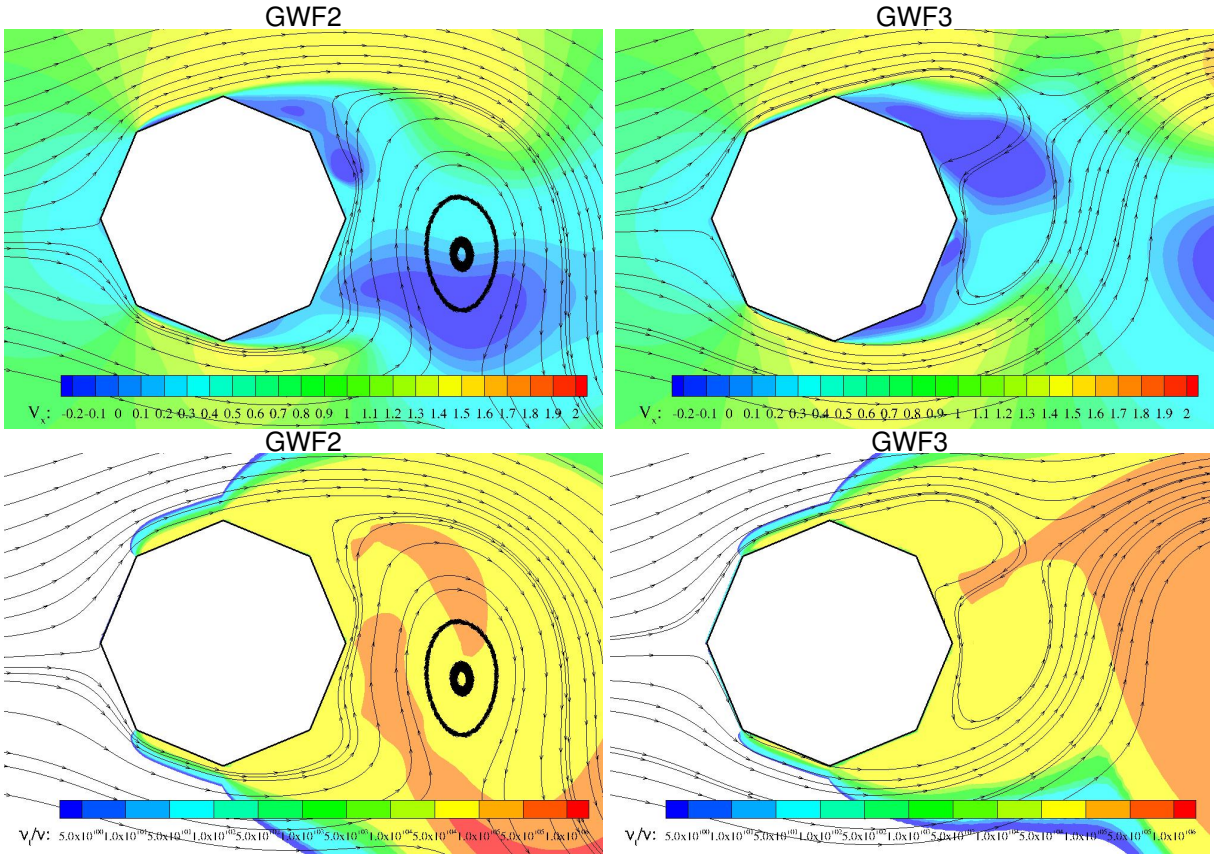

Figure B.5: Visualization of the flow field and isolines of V_x and ν_t/ν at a time instant (different for each grid). Flow around an octagonal cylinder at a Reynolds number of 10^8 calculated with wall functions.

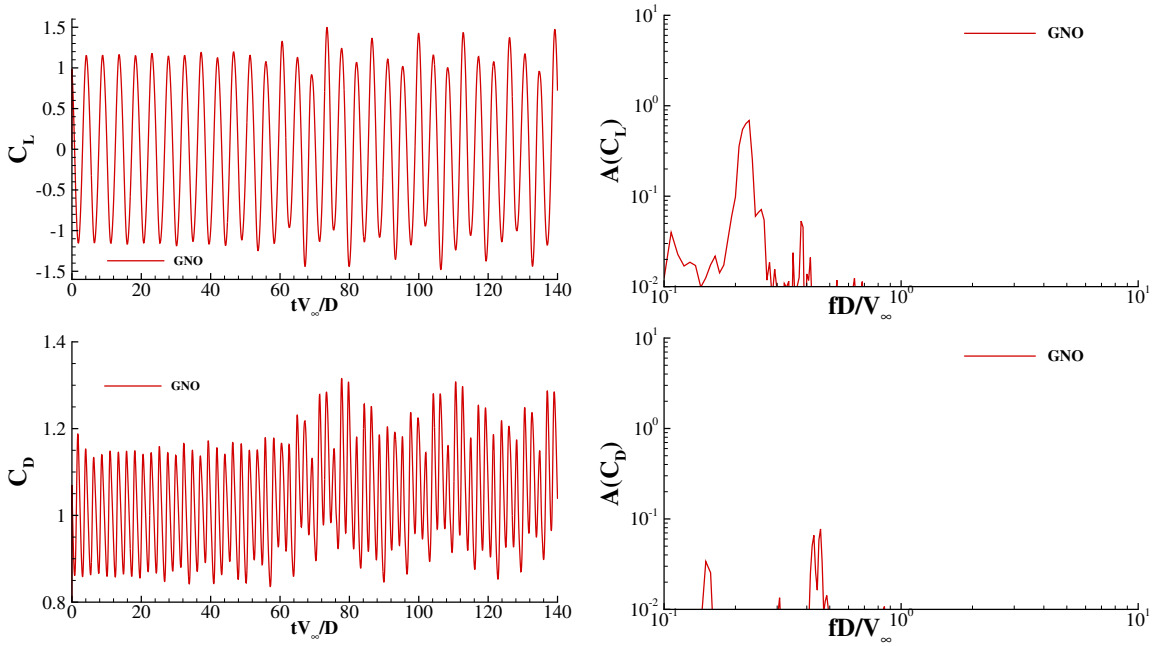

Figure B.6: Time history of the lift C_L and drag C_D coefficients and their frequency content. Simulations performed in the coarsest grids of set GNO (without wall functions). Flow around an hexadecagonal cylinder at a Reynolds number of 10^8.

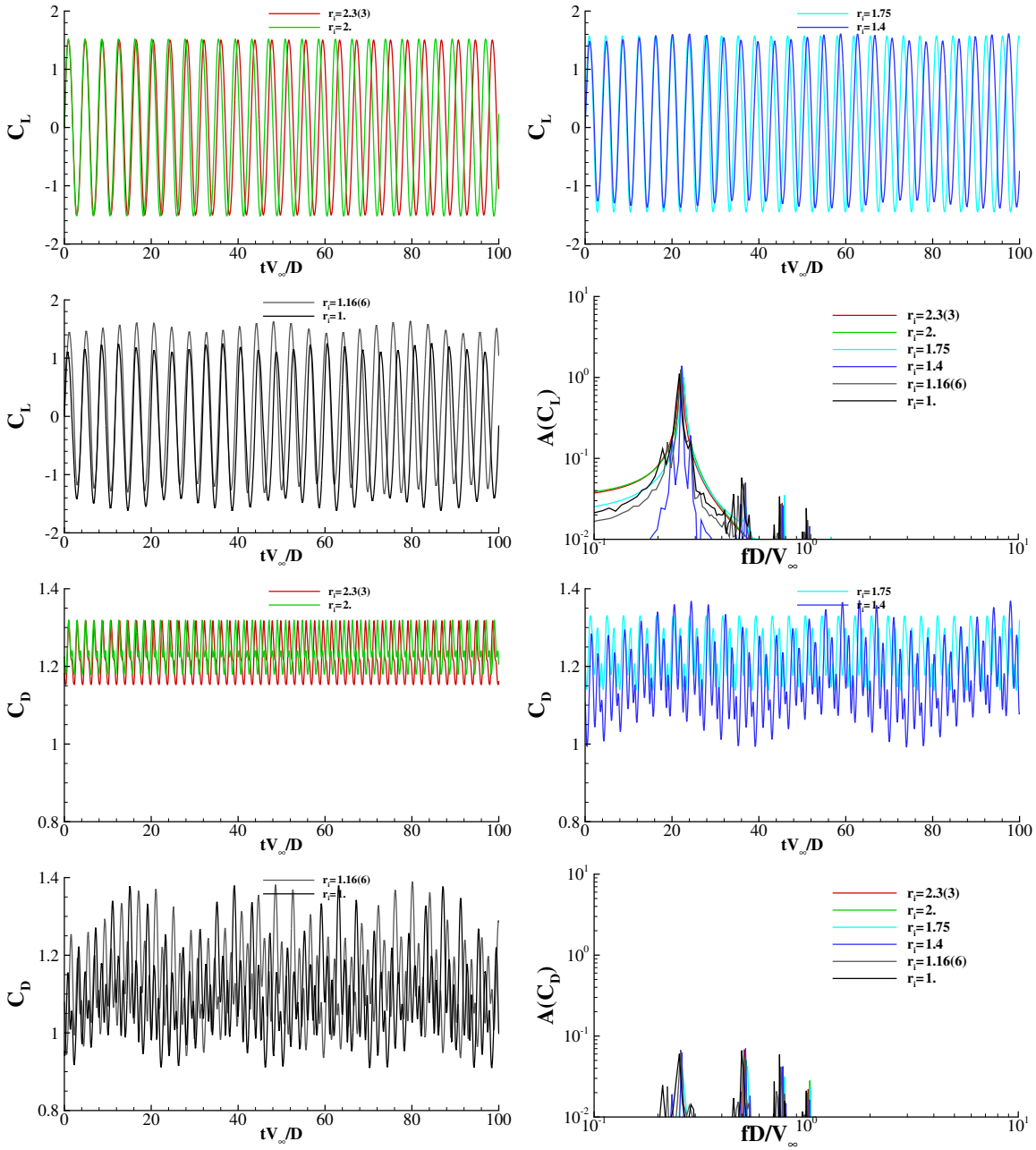

Figure B.7: Time histories of the lift C_L and drag C_D coefficients and their frequency content. Simulations performed in the grids of sets GWF1 (with wall functions). Flow around an hexadecagonal cylinder at a Reynolds number of 10^8.

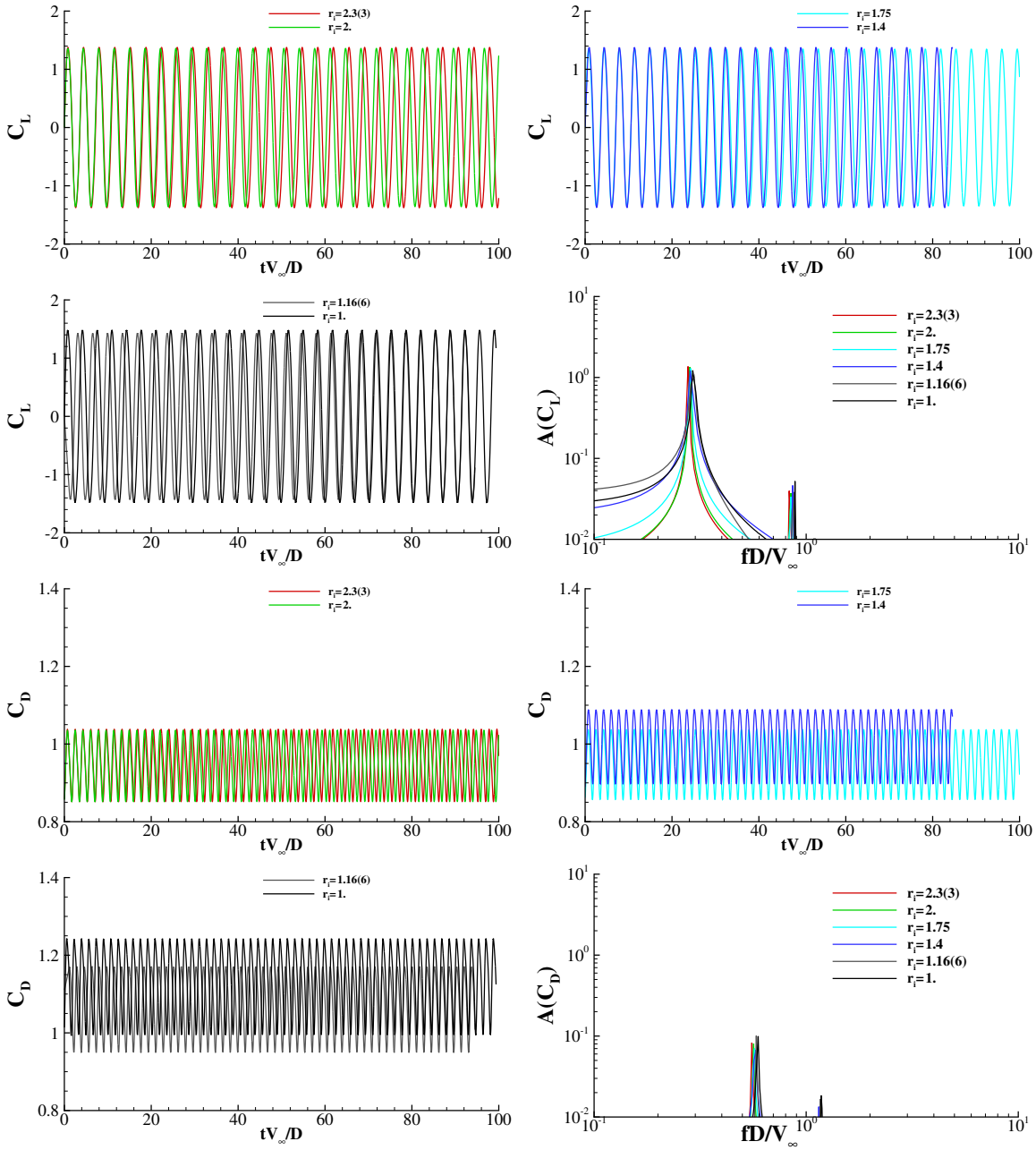

Figure B.8: Time histories of the lift C_L and drag C_D coefficients and their frequency content. Simulations performed in the grids of sets GWF2 (with wall functions). Flow around an hexadecagonal cylinder at a Reynolds number of 10^8.

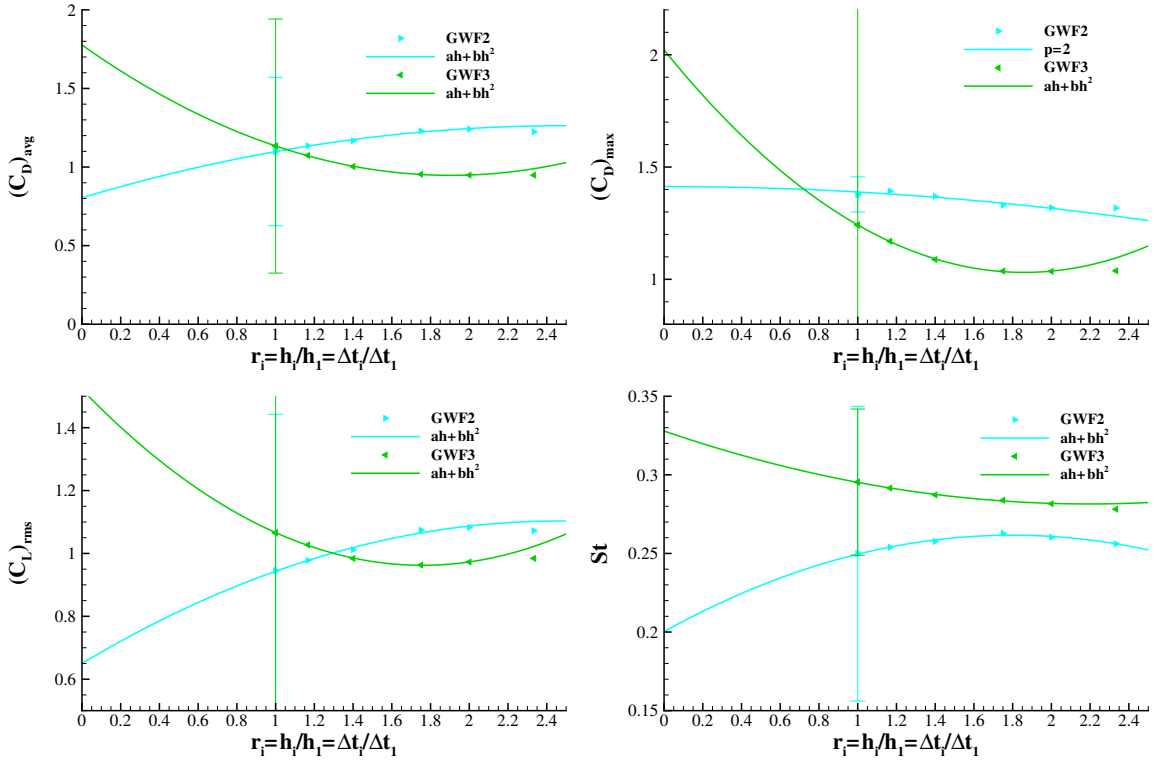

Figure B.9: Convergence with grid/time refinement of average $(C_D)_{avg}$ and maximum $(C_D)_{max}$ drag coefficient, root mean squared $(C_L)_{rms}$ lift coefficient and Strouhal number St. Flow around an hexadecagonal cylinder at a Reynolds number of 10^8 calculated with wall functions.

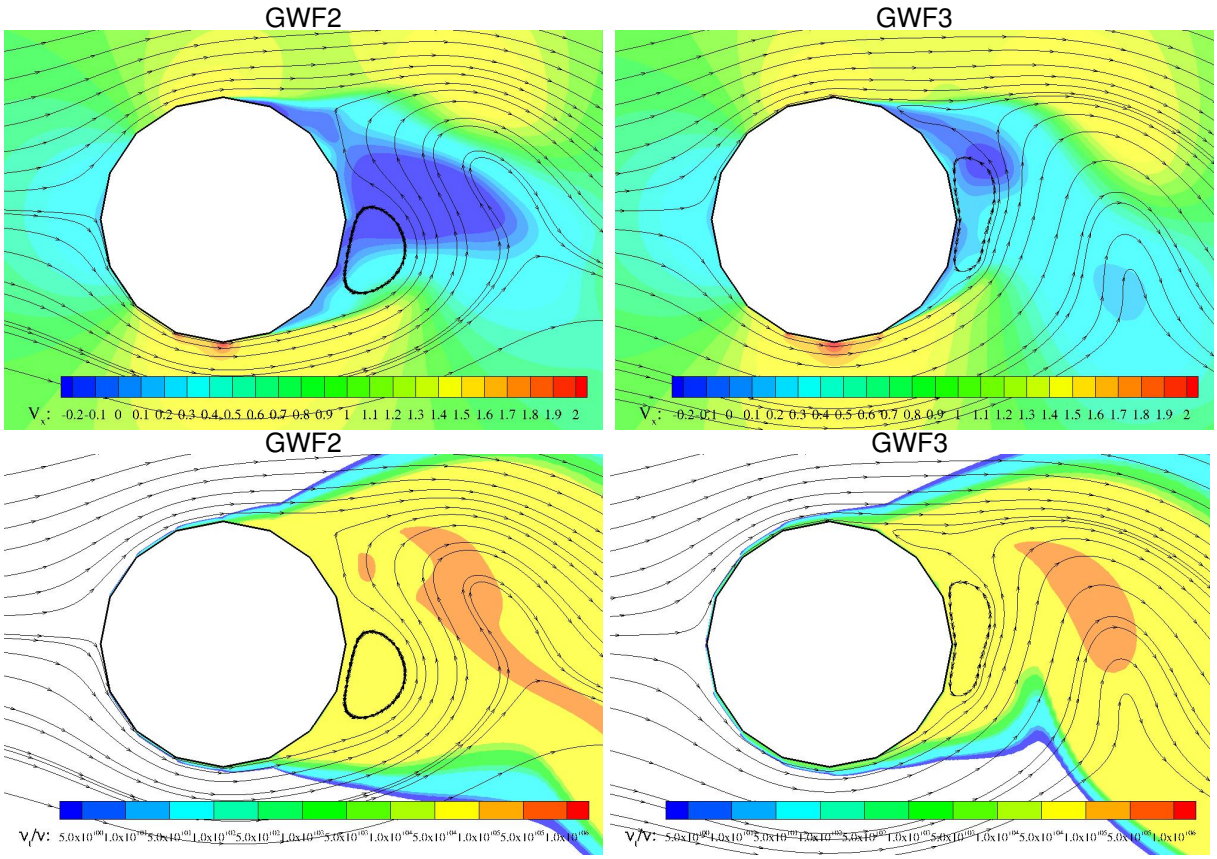

Figure B.10: Visualization of the flow field and isolines of V_x and ν_t/ν at a time instant close to the minimum lift coefficient. Flow around a hexadecagonal cylinder at a Reynolds number of 10^8 calculated with wall functions.